SANDIA REPORT

An Uncertainty Analysis of the Hydrogen Source Term for a Station Blackout Accident in Sequoyah Using MELCOR 1.8.5

DRAFT Report For Review

Prepared by:

R.O. Gauntt,

Nathan Bixler, and

K.C. Wagner (ITSC)

Sandia National Laboratories
P.O. Box 5800
Albuquerque, NM 87185-0739

Abstract

A methodology for using the MELCOR code together with the Latin Hypercube Sampling method was developed to estimate uncertainty in various predicted quantities such as hydrogen generation or release of fission products under severe accident conditions. In this case, the emphasis was on estimating the range of hydrogen sources in Station Blackout conditions in the Sequoyah Ice Condenser plant, taking into account uncertainties in the modeled physics known to affect hydrogen generation. The method uses user-specified likelihood distributions for uncertain model parameters, which may include uncertainties of a stochastic nature, to produce a collection of code calculations, or realizations, characterizing the range of possible outcomes. Presently, we refer to this methodology as the *MELCOR Probabilistic Uncertainty Analysis Methodology (MPUAM).* Forty MELCOR code realizations of Station Blackout in Sequoyah were conducted that included 10 uncertain parameters, producing a range of in-vessel hydrogen quantities. The range of total hydrogen produced was approximately 583kg ± 131kg. Sensitivity analyses revealed expected trends with respected to the parameters of greatest importance, however, considerable scatter in results when plotted against any of the uncertain parameters was observed, with no parameter manifesting dominant effects on hydrogen generation. It is concluded that, with respect to the physics parameters investigated, in order to further reduce predicted hydrogen uncertainty, it would be necessary to reduce all physics parameter uncertainties similarly, bearing in mind that some parameters are inherently uncertain within a range. It is suspected that some residual uncertainty associated with modeling complex, coupled and synergistic phenomena, is an inherent aspect of complex systems and cannot be reduced to point value estimates. We conclude that probabilistic analyses such as the one demonstrated in this work are necessary in order to properly characterize response of complex systems such as severe accident progression in nuclear power plants.

Table of Contents

List of Figures

List of Tables

1 Background and Objectives

In support of an NRC initiative that has as its objective the "Risk Informing" of nuclear power plant regulations, a number of studies have been performed recently to evaluate hydrogen production and behavior in Ice Condenser plants for the purpose of re-evaluating present regulations concerning hydrogen controls. A previous report, titled "Hydrogen Source Terms for Station Blackout Accidents in Sequoyah and Grand Gulf Estimated Using MELCOR 1.8.5," [1] provided point estimates for a number of variations on station blackout accidents for two plants. These studies represented an important advance in the performance of detailed integrated plant analyses. The present study builds on this earlier work by incorporating an uncertainty analysis methodology into the integrated plant accident analysis.

In this study, the analyses are carried out using the MELCOR code, version 1.8.5 [2] that provides for a detailed, best estimate integral and self consistent analysis of severe accident progression in a nuclear power plant. This includes coupled analysis of initiating RCS thermal hydraulics, coolant loss, heating of core fuel and cladding, initiation of cladding oxidation and hydrogen production, core melting and relocation, RCS heatup and failure, and thermal hydraulic response of the containment.

The objective of this study is to characterize the uncertainty in the predicted in-vessel and ex-vessel hydrogen production in an un-recovered station blackout accident in the Sequoyah Ice Condenser plant. This methodology for performing this uncertainty characterization is described in body of this report. In that the methodology makes use of the MELCOR code to produce the uncertainty quantification based on the likelihood characterization of uncertainty parameters, we refer to it here as the *MELCOR Probabilistic Uncertainty Analysis Methodology (MPUAM)*, and while this study has emphasized hydrogen production, the methodology can be used to characterize uncertainty in the prediction of other issues, such as fission product source terms. In this case, the uncertainty characterization of hydrogen source terms determined in this study will be used to perform assessments of igniter and recirculation fan efficacy for station blackout conditions in ice condenser plants.

2 Scope of Present Study

The objective of this study is to characterize the uncertainty in the predicted in-vessel and ex-vessel hydrogen production in an un-recovered station blackout accident in the Sequoyah Ice Condenser plant using the MELCOR code itself to characterize that uncertainty. Uncertainty in the predicted hydrogen generation arises from a host of uncertainties concerning the state of knowledge in the physical processes that influence hydrogen production, as modeled in MELCOR. Many factors can influence hydrogen generation in an integral analysis, including the modeling of the oxidation reaction itself, core melt progression, heat transfer, thermal hydraulic conditions, as well as others. Uncertainty can also arise from random variations in the presumed accident progression, such as the timing and degree to which pump seals deteriorate, or whether or not a relief valve sticks open after being challenged for some period of time. Insofar as MELCOR input description prescribes the otherwise deterministic description of the accident progression, both types of uncertainty can be accommodated by the methodology described in this report.

The basic approach of this methodology is to identify the MELCOR input parameters, sensitivity coefficients, and modeling options that describe or influence the uncertainty of interest, prescribe likelihood descriptions of the potential range of these parameters, and evaluate the code predictions using a number of different randon combinations of parameter inputs sampled from the likelihood distributions. In order to limit the number of "realizations" (code calculations) needed to characterize the full range of uncertainty, the Latin Hypercube Sampling method [3] (LHS) is used to sample the input parameter distributions. This methodology is described in this report as the *MELCOR Probabilistic Uncertainty Analysis Methodology (MPUAM)*, and while this study has emphasized hydrogen production, uncertainty in the prediction of other issues, such as fission product source terms.

In this study, we have limited to scope principally to the characterization of knowledge based uncertainties affecting hydrogen generation for a specific accident scenario, Short Term Station Blackout, for the Sequoyah Ice Condenser plant. Knowledge based uncertainty refers to uncertainties in the modeling of the physical processes affecting hydrogen generation. After a description of the MELCOR model for the Sequoyah plant, including details on specific treatments for RCS natural circulation processes, core plate modeling and lower head thermal/mechanical failure modeling, Section 4 provides a discussion of the MELCOR parameters identified as potentially influencing hydrogen generation and the subjective evaluation of the authors concerning the likelihood that the correct or true value for that parameter lies within a given range (i.e. cumulative distributions are constructed to describe the likelihood of a parameter taking a specific value within a range). Section 5 describes the LHS sampling method and the Desktop PA application that was used to perform the LHS sampling and prepare individual MELCOR input files for performing the uncertainty realizations. Results of the 40 MELCOR LHS realizations of the STSBO scenario are described in Section 6, where basic accident signatures are identified and trends are characterized. Section 7 presents statistical analyses of parameter importance relative to the hydrogen uncertainty range, and Section 8 summarizes the principal findings of this study.

3 Sequoyah PWR Ice Condenser Plant

3.1 General Plant Description

The input model for the Sequoyah Ice Condenser plant was based on one that was developed previously [4]. Significant improvements to the Sequoyah model were made in the conduct of the present work, including a revision to the core modeling to treat 5 radial regions and 12 axial ones, and important upgrades to the core support modeling and the lower head thermal/mechanical loading. The Sequoyah-class of plants all make use of 4-loop Westinghouse PWR nuclear steam systems (NSS) housed within Ice Condenser type containments. Details on the principal elements of this plant are provided in the following sections. A description of the two major plant designs, including a description of the MELCOR models for these plants is provided in the following sections. Key reactor characteristics for the Sequoyah plant are summarized in Table 3-1.

Table 3-1. Key Reactor Characteristics.

Characteristic	Sequoyah
Reactor type	PWR
Operating Power	3411 MW
Operating Pressure	15.5 MPa (2250 psia)
In-vessel Fluid Volume	Pressurizer – 51 m^3 Accumulators – 4 x 29.5 m3 Vessel – 137.5 m^3
Containment Volumes	
Total UO_2 Mass	98,250 kg
Active Zr Cladding Mass	20,207 kg
Total Zr Mass	20,207 kg
Total Steel Mass	27,942 kg

3.2 Reactor Core and Vessel Nodalization

The Sequoyah reactor core represented in the MELCOR model is shown in Figure 3-1. This figure shows both the CV (control volume) nodalization and the core cell (COR) nodalization. (Control volumes represent the fluid state throughout the core and COR cells resolve the core solid regions spatially). Within the active core region two COR cells in axial order are housed within a single fluid control volume with a one to one correspondence used between CV and COR regions radially. Each CV volume is connected both radially and axially with adjacent CV's by flow paths thereby allowing prediction of 2-D flow of fluids (liquid or vapor) within the core region. The mass of materials comprising the Sequoyah core region is summarized in Table 3-2. If the entire quantity of zircaloy in the core were to become oxidized by steam, 893 kg of hydrogen would be produced. The total core

operating power prior to shutdown is assumed to be 3411 MWth. The radial and axial power shapes for the Sequoyah model are provided in Table 3-3 and Figure 3-2.

Figure 3-3 shows the balance of the CV nodalization for the reactor vessel. The lower head region is represented by a single large volume; however a finer CV nodalization is used in the regions above the core in order to resolve natural circulation patterns associated with hot leg counter-current flow phenomena. Flow paths are also indicated in the figure.

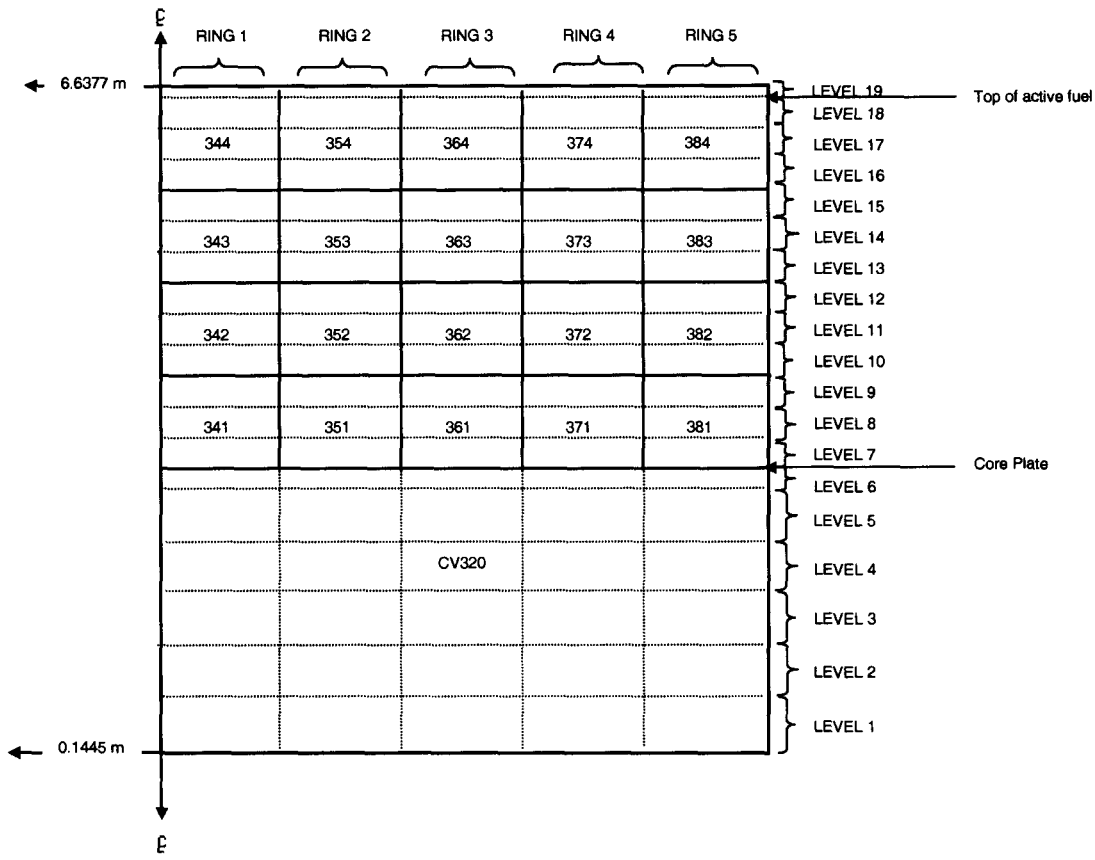

Figure 3-1. Core nodalization used in the Westinghouse Sequoyah MELCOR model.

Table 3-2. Mass of core materials.

Core Material	Total Mass [kg]
UO_2	98250
Zr	20207
SS	27942
Control Poison (Ag-In-Cd)	4602

Table 3-3. Core radial power distribution.

Core Ring	Number or Assemblies	Area or Ring	Fraction of Assemblies	Sequoyah Radial Power Factors
1	13	0.5977	0.067	1.2085
2	44	2.0230	0.228	1.1198
3	48	2.2069	0.249	1.1118
4	44	2.0230	0.228	1.0001
5	44	2.0230	0.228	0.6966
	193	8.9239	1.000	

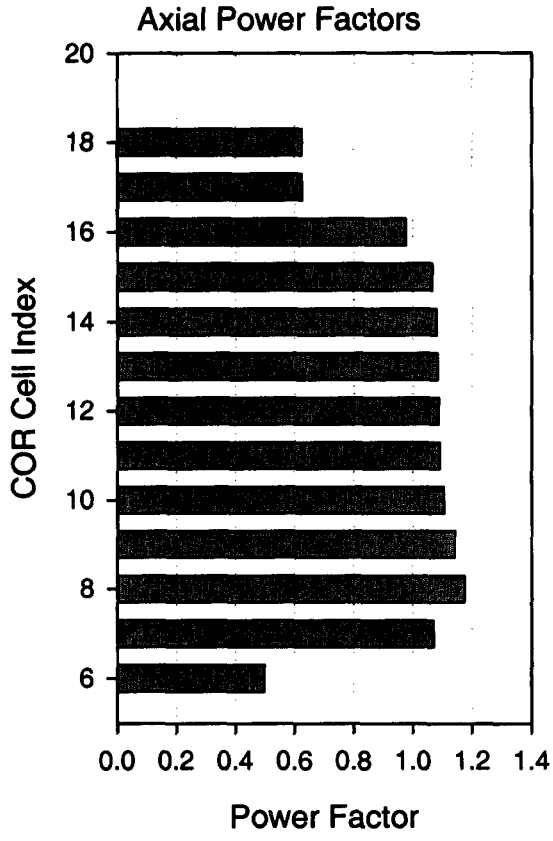

Figure 3-2. Axial power distribution for the Sequoyah core.

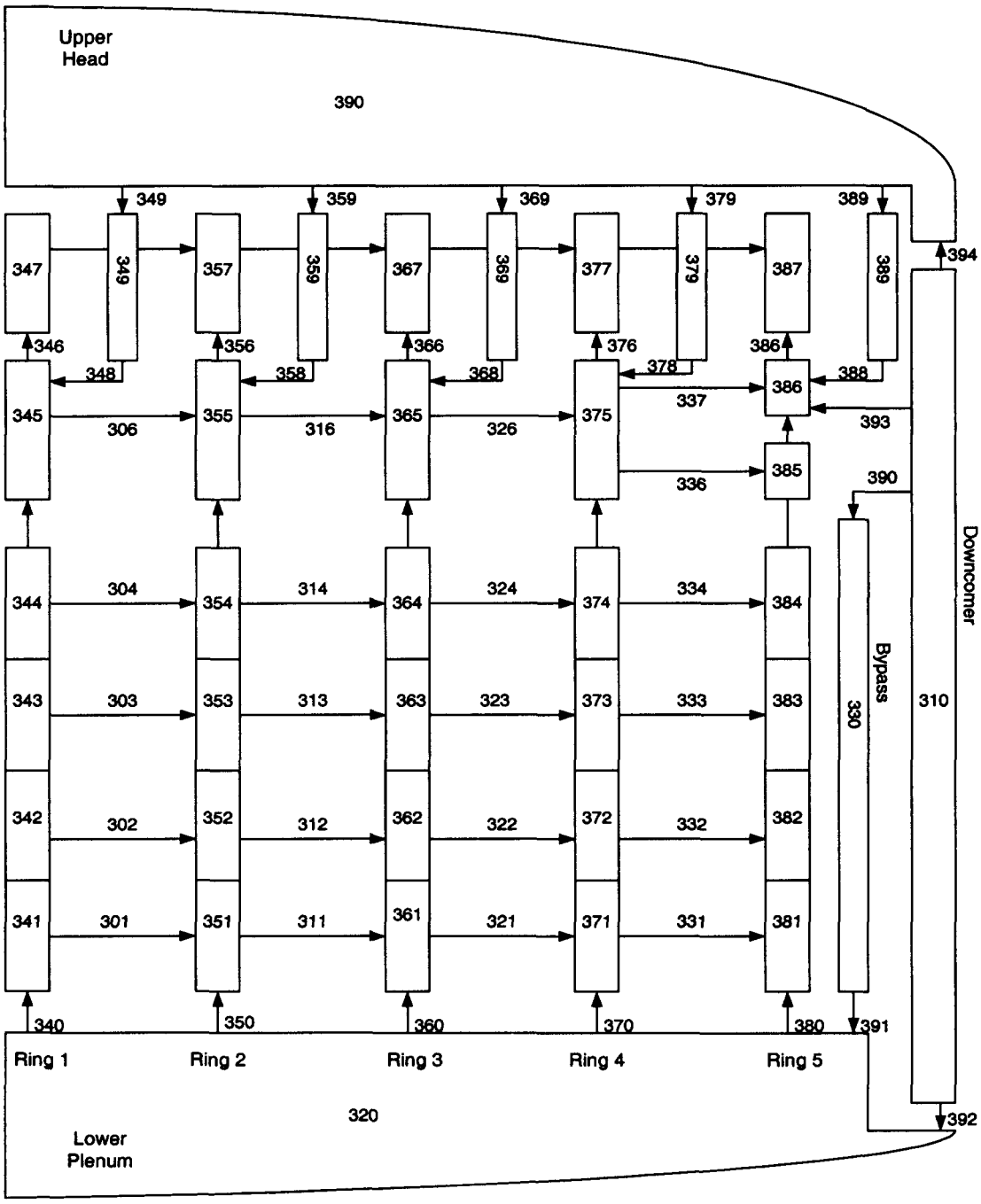

Figure 3-3 Reactor vessel CVH nodalization used in the Westinghouse Sequoyah model

3.3 Core Support Structure Modeling

In MELCOR 1.8.5, several new models were added to calculate the thermal/stress failure of the core supporting structures. The supporting structure component, in any core cell may be treated as representing an edge-supported plate, a grid-supported plate, a BWR core plate, or BWR control rod guide tubes. The models are specified by the keywords "PLATE," "PLATEG," "PLATEB," and "COLUMN," respectively. In the process of upgrading the MELCOR plate models to include natural circulation flow and new version 1.8.5 modeling enhancements, the new lower structure support models were implemented.

To explain the implementation of the new support models, it is useful to review the construction of the Westinghouse PWR reactor. Figure 3-4 shows the internals of a Westinghouse PWR vessel. The core is supported by a core-support structure (see Figure 3-5 and Figure 3-6). The core support structure is hung from near the top of the vessel. The core barrel extends from near the top of the vessel to the lower plenum. Above the lower core support plate are columns that extend to the core plate. The columns transmit the weight of the fuel from the core plate to the lower core plate. Also inside the region between the core plate and the lower core support plate is a flow distribution plate. The flow distribution plate does as it name implies.

Recently, as part of an upgrade to a 5 ring vessel model, several changes were made to improve the modeling of the support structures in the lower plenum. The new 5 ring model developed for this work used the PLATEG model at Level 5 (see Figure 3-7). In this model, debris can be retained at Level 5 once the core plate failes at Level 6. In addition, PLATEB was specified for Level 6. The default stress coefficient for the two PLATEG models were replaced with a coefficient that was consistent with the PWR geometry (i.e., column-supported versus grid-supported). It is important to note that the same stress model is used for the PLATEB and PLATEG models. It is the value of the AKMB coefficient that adjusts the distribution of the stresses for a grid or column geometry. Consequently, the PLATEB model can be adjusted to give a stress loading like a PLATEG model and visa-versa. In the process of calculating the AKMG term for the new PLATEG model, the actual geometry of the PWR columns was considered rather than the code default value. The new specified value of AKMG is expected to increase the stress by approximately a factor of two.[1]

Figure 3-7 shows the nodalization for the 5 ring lower core support structures. Level 6 is the core plate and is modeled as a PLATEG that is supported by an array of columns. The thickness of the core plate is 2 inches. Level 5 models the flow distribution plate. It is 1.5 inches thick and will retain debris once Level 6 fails. Level 4 uses a COLUMN model. The PLATEG and PLATEB models do not transmit loads through the COLUMN model; however, the COLUMN model allows the mass of the columns to be represented and permits heat conduction between support structures above and below that core level. Without a supporting structure at Level 4, heat conduction from the hot debris to lower levels would not be modeled. The COLUMN is specified to fail once the core

1 The default value of AKMG was consistent with larger BWR control rod drive tubes.

plate and flow distribution plate fail (i.e., the PLATEG models at Levels 5 and 6).2 Finally, the lower core support plate is modeled with a PLATE model. It is radially supported by core barrel. The PLATE model will retain debris. However, when a section of the plate fails, the failed section of the plate and everything resting on it will be converted to PD and allowed to fall, taking with it any as-yet-unfailed inner rings of the plate together with everything resting on them. The outermost ring of the plate is treated as self-supporting until it fails. Conversely, the PLATEB and PLATEG models allow independent failure of any ring section without affecting other core rings.

2 Also, the COLUMN model allows any debris to fall through prior to its failure.

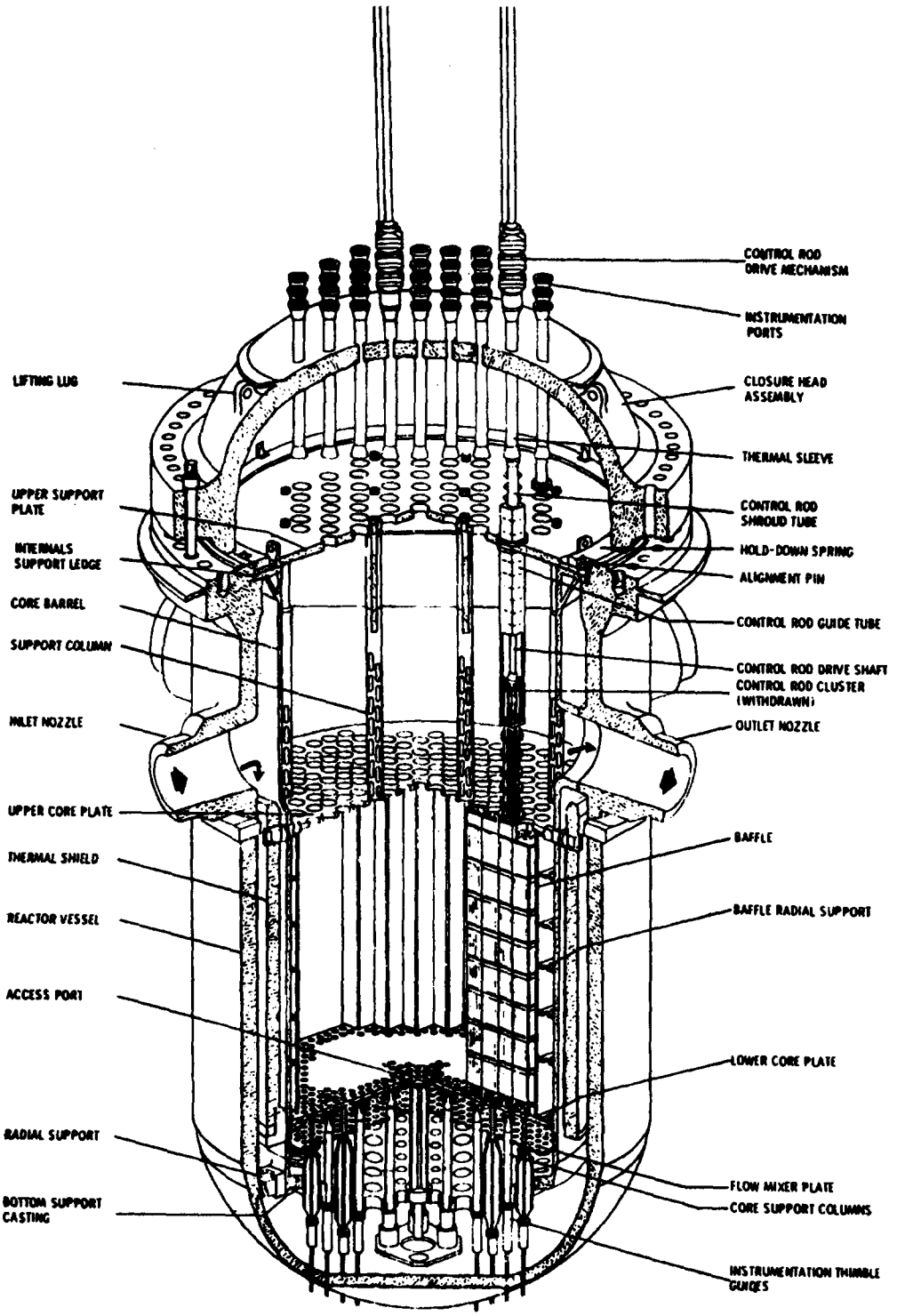

Figure 3-4 Westinghouse PWR Reactor Vessel Internals.

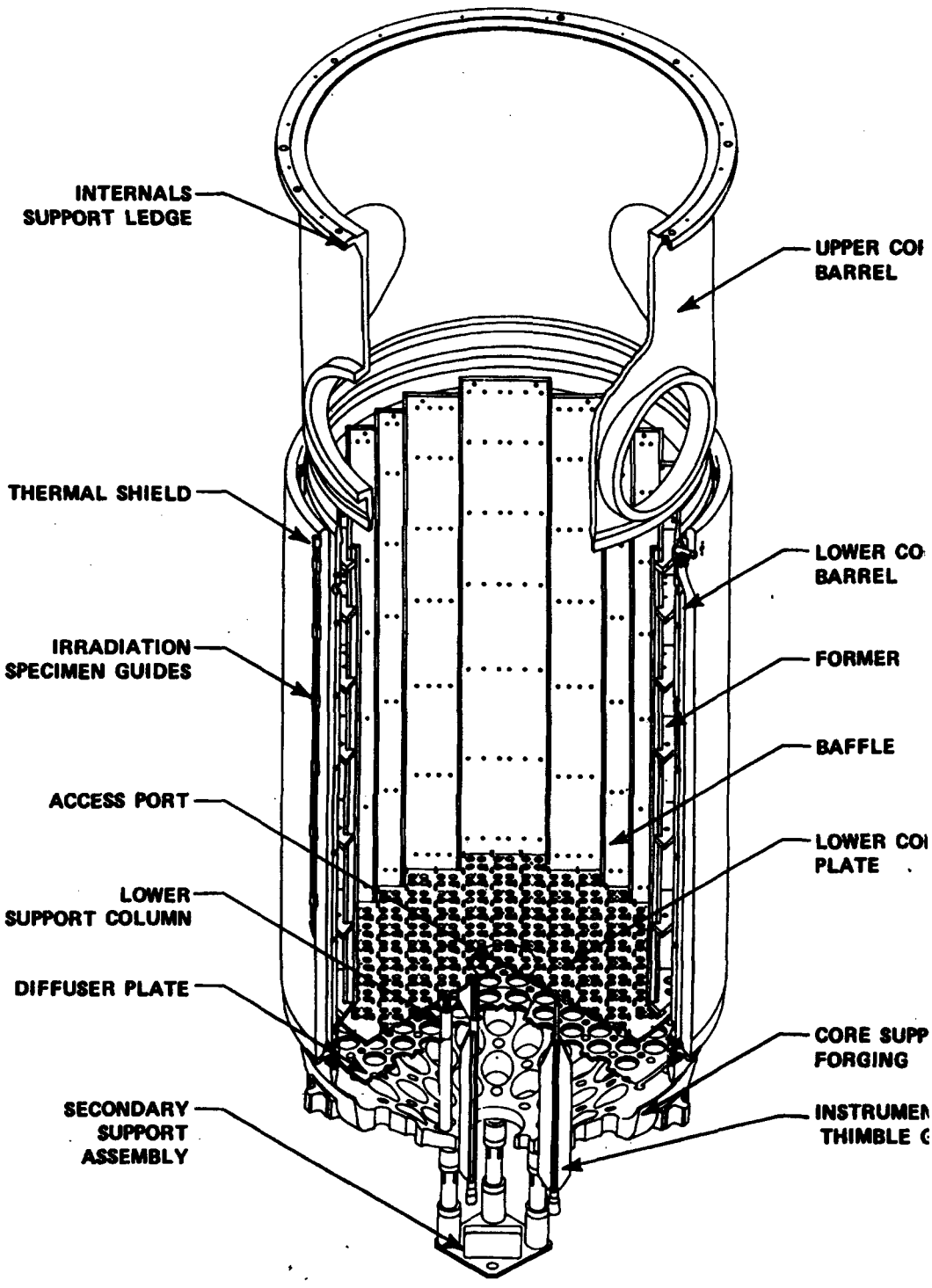

Figure 3-5 Westinghouse PWR Lower Support Structure.

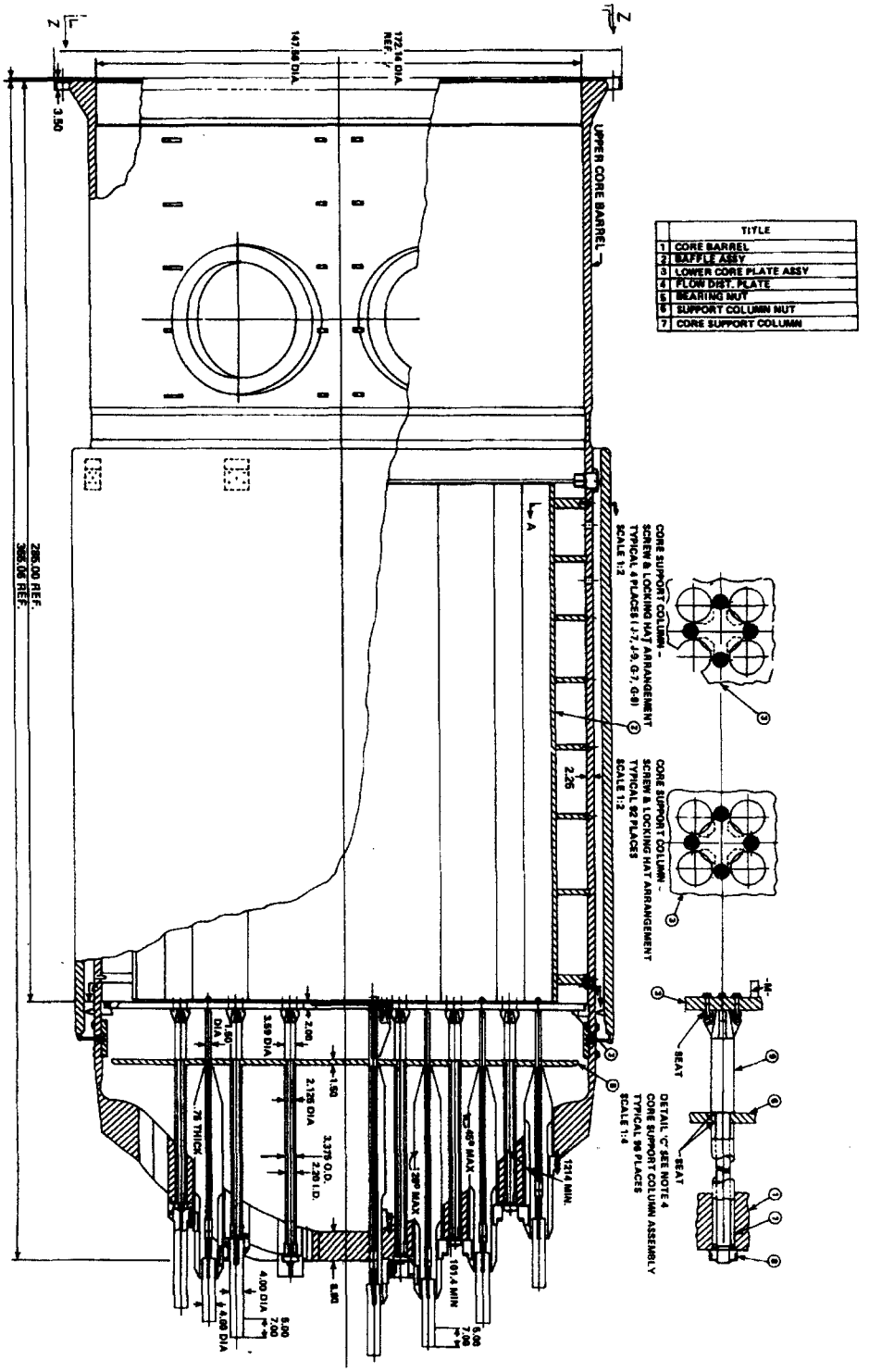

Figure 3-6 Westinghouse PWR Core Barrel Assembly.

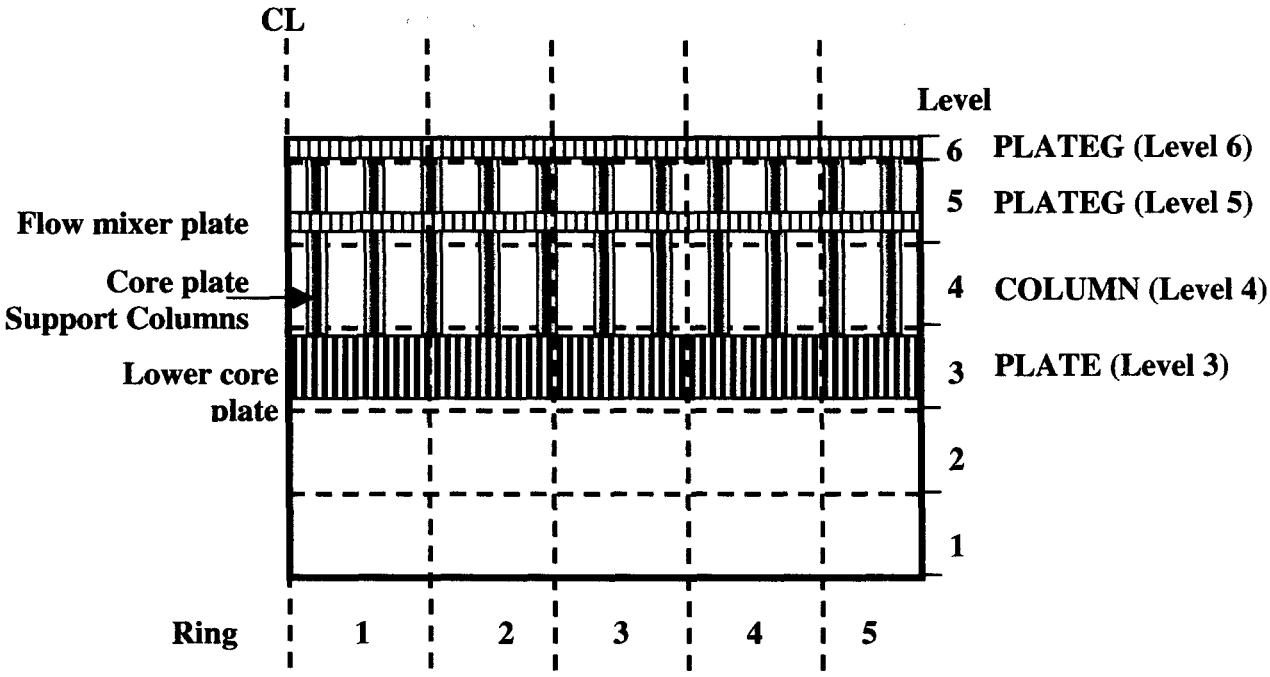

Figure 3-7 Core Support Nodalization for the New 5 Ring Model.

3.4 Modeling of Lower Head Thermal/Mechanical Loading and Failure

Several changes were made to improve the modeling of the lower head thermal/mechanical response. In particular, most previous MELCOR PWR calculations had shown failure of lower head penetrations (i.e., via the penetration thermal-failure model), leading to a blowdown and ejection path for the debris. Based on research from TMI-2 and the SNL lower head experiments, it is believed that the thermal lumped-capacitance penetration mode in MELCOR over-estimated the vulnerability of these locations. It was expected that a gross thermal-mechanical weakening on the lower head itself (i.e., perhaps near penetration locations) would be better calculated using MELCOR's 1-dimensional lower head conduction model with integrated Larson-Miller thermal-stress correlations. To implement this approach, the following changes were made,

Lower head failure by means of the default penetration model was disabled by specifying that the penetrations have a failure temperature of 2000 K (i.e., an arbitrarily high temperature that was well above the melting temperature of the lower head). Furthermore, the surface area, contact area to the lower head, and penetration mass characteristics were specified to force close thermal coupling between the penetration and the lower head (i.e., the penetration followed the lower head surface temperature). A modified penetration failure criterion was implemented using control function logic to more properly model realistic lower head thermal loading and failure. The penetration was

specified to fail (i.e., by control function logic) if a location 1-cm within the outer surface of the lower head[3] reached within 100 K of the steel melting temperature.

Based on observations from the Sandia Lower Head Failure experiments, tube penetration failure would not appear to be the dominant or expected mode of vessel failure until temperatures nearing the melting point are encountered near the tube welds, especially under low differential pressure conditions. Moreover, the present penetration model is judged to be overly simplistic and not useful. We propose basically disabling the model and deferring the lower head failure to the global creep rupture model. The important parameter determining the action of the creep rupture model is the value used for the heat transfer coefficient between core debris in the vessel head and the head material itself. A parametric model is presently in use that uses a heat transfer coefficient analogy to what is actually a conduction problem at the time that core materials initially arrive in the lower plenum. A heat transfer coefficient appropriate for representing conduction can be estimated as follows

$$H = \frac{k}{\delta x}$$

where k is the thermal conductivity of the fuel crust/debris and δx is the characteristic dimension over which conduction takes place. The following figure illustrates the range of heat transfer coefficient appropriate for different conduction thicknesses assuming thermal conductivity appropriate for a ceramic urania crust. As can be seen, until crust thickness become very thin (as might be expected for fully developed molten pool natural circulation) the resulting H is considerably smaller than the current MELCOR default constant value of 1000 watt/m^2K. Values ranging between 20 and 200 are considered more appropriate for use during the "conduction" period of lower head heating by core materials. Indeed, without external water-cooling, the head might likely fail before such fully developed molten pool circulation has time to develop.

As the lower head debris reaches higher and higher temperatures, radiation heat transfer is expected to begin to dominate. For this reason, at high temperatures regardless of the conduction regime thermal conductivity in use, the effective radiation heat transfer must be considered. A simple black-body radiative exchange term was added to the convective heat transfer coefficient. In particular, the radiation term was estimated as follows,

$$q = h_{rad,effective}\, A\, (T_{Debris} - T_{Lower\ Head}) = \sigma\, A\, (T^4_{Debris} - T^4_{Lower\ Head})$$

---

[3] If the outer surface of the lower head happened to be in nucleate boiling, there could be a sharp temperature gradient through the lower head. In this configuration, the penetration would not fail because a location that was 1-cm from the outer surface would be close to the saturated water temperature (~400 K). Consequently, the lower head could be cooled sufficiently to retain its mechanical integrity. In this configuration, the lower head Larson-Miller thermal stress correlations would be used to assess the integrity of the lower head. If the outer surface departed from nucleate boiling (or there was no water) and the outer surface heated close to the steel melting temperature, then the described penetration failure was active (i.e., a fallback if the Larson-Miller thermal-stress criteria did not predict failure a low mechanical stress conditions).

or,

$$h_{rad,effective} = \sigma (T^4_{Debris} - T^4_{Lower\ Head}) / (T_{Debris} - T_{Lower\ Head})$$

Figure 3-8 Estimation of heat transfer coefficient for lower heat heating by fuel debris.

Finally, if debris temperatures sufficiently high are attained such that a molten pool would be expected, the heat transfer must again be increased and order to reflect the effect of natural circulation convection heat transfer. In this regime, heat transfer coefficients on the order of 1 to 2000 are expected. Presently, MELCOR's treatment of heat transfer to the lower head surface is quite primitive with respect to the phenomena just discussed. Minor code modifications have been implemented allowing control function access to the previously constant user input heat transfer coefficient from lower head debris to the lower head wall. The control function access allows us to calculate a varying heat transfer coefficient based upon monitored values of the lower plenum debris temperature, and the lower head temperature both on the surface and within the head thickness. With this model we first assume an initial conduction regime heat transfer coefficient on the order of 100 w/m^{2}K. As the debris temperature heats up following dry out, the heat transfer coefficient is increased using the simple radiation model described above. When the debris temperature reaches 2800 K, it is assumed that debris melting will take place, and the heat transfer coefficient will be

C01

increased to 2000 w/m^{2}K as the temperature approaches 3300 K. Finally, the temperature of the center of the lower head is monitored high control function. If this temperature reaches 1600 K, it is assumed that the head will fail due to loss of strength. Figure 3-9 and Figure 3-10 illustrate the behavior of this control function model.

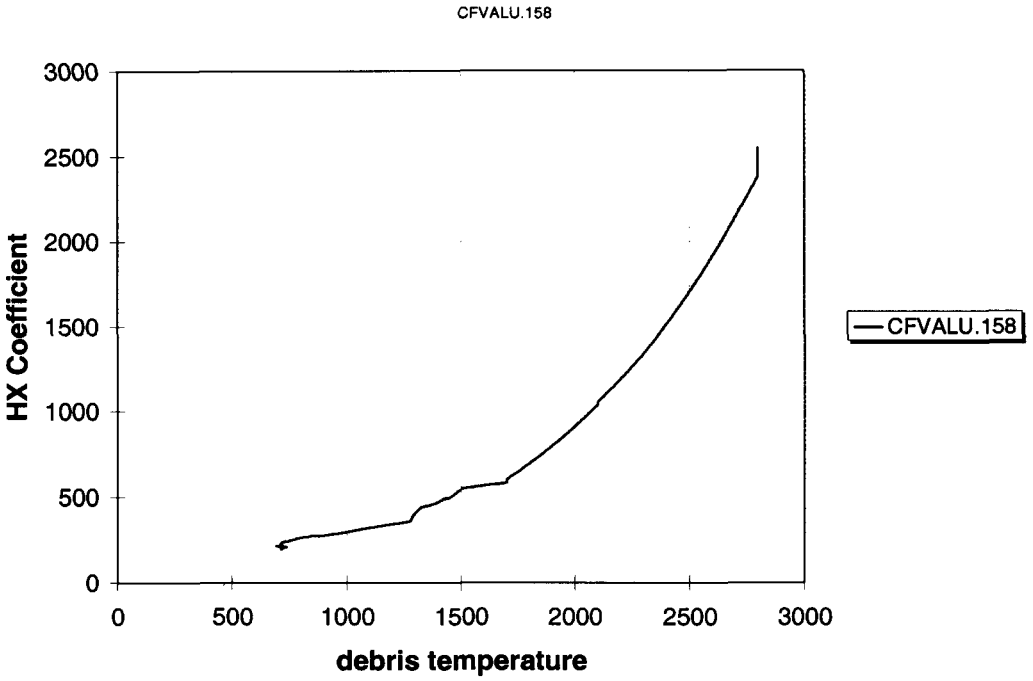

Figure 3-9 Debris to lower head heat transfer coefficient predicted by control function.

Failure of the lower head will be calculated using the Larson-Miller correlation, given the heat load supplied by the previously discussed heat transfer mechanisms. In addition to Larson Miller, as mentioned previously, failure of the head will also be assumed if the internal head temperatures are calculated to be in excess of 1600 K. This condition will actually result in the activation of the penetration failure model using control function logic.

3.5 Reactor Coolant System Nodalization

The Westinghouse steam generators are of the inverted U-tube design. When the secondary side of these steam generators is water filled, heat rejection from the primary coolant system can be sustained during an accident with loss of pumping power by full-loop natural circulation. Additionally, when the void fraction in the primary coolant system hot legs and steam generator becomes large, vapor phase hot leg counter-current natural circulation patterns can form which have important heating effects on the hot leg, surge line and steam generator tubes. These two types of circulation behavior are illustrated in Figure 3-11.

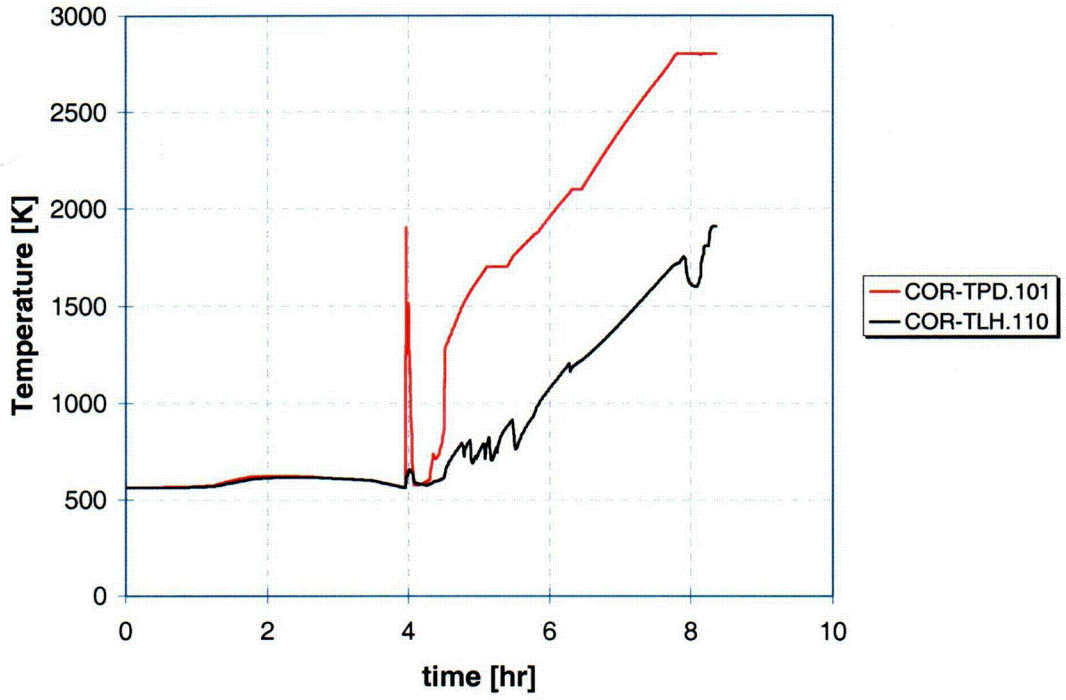

Figure 3-10 MELCOR-predicted temperatures of lower head debris and head wall for the Sequoiah model using the control function heat transfer coefficient.

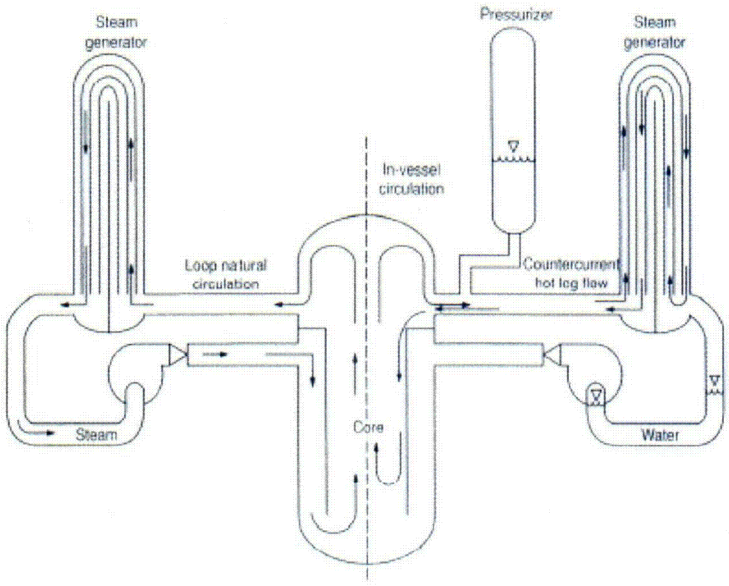

Figure 3-11. Illustration of the full-loop and hot leg counter-current natural circulation patterns in the Westinghouse PWR reactor coolant system.

C02

This MELCOR model uses a single reactor coolant system nodalization shown in Figure 3-12 that captures both of these important natural circulation phenomena that affect significantly the progression of high pressure accidents. This point is emphasized here because previous analyses of these phenomena using MELCOR and SCDAP/RELAP-5 up to now have used two separate nodalizations, one to describe the water-filled RCS behavior, and a second nodalization to describe the hot leg countercurrent flow behavior. This approach involved running the first nodalization up until the point that voiding of the RCS occurred, and then manually mapping thermal hydraulic conditions to the second nodalization in order to continue the analysis. It was not uncommon that different flow resistances were used in each nodalization. The present study uses a significantly improved approach requiring only the single nodalization. Details on this models are described in reference [4], but in short, this is accomplished by splitting the hot and surge line nodalizations into an upper and lower half that exhibit the correct flow resistances when the predominant coolant flow is either unidirectional or counter-current for either liquid water or vapor flows. Transition from unidirectional liquid flow to counter-current vapor flow (motivated by vapor density differences within the steam generator tubes) is automatically handled by the model as the void fraction in the hot leg and steam generator becomes sufficiently large. When hot leg flows in the upper and lower halves are in opposing directions (countercurrent) a pressure drop term representing the shear forces between the opposing flows is introduced using the MELCOR Quick-CF pump feature. The shear forces vanish when the flows become unidirectional. Not shown in Figure 3-12 are the flow paths for the cold leg accumulators. RCS primary and secondary pressure control and coolant injection characteristics are summarized in Table 3-4.

Table 3-4 Summary of RCS Primary and Secondary pressure control and coolant injection characteristics.

Parameter	Rated flow or volume	Setpoint [MPa]
Pressurizer PORV (2)	26 [kg/s] (each)	16.2
Safety Relief Valves (3)	53.5 [kg/s] (each)	17.2
Accumulators (4)	29.5×10^3 [kg]	4.24
SG secondary safety valves (5)	5 x 99 [kg/s] per SG	7.44 – 7.81
SG relief valves	112 [kg/s]	7.62

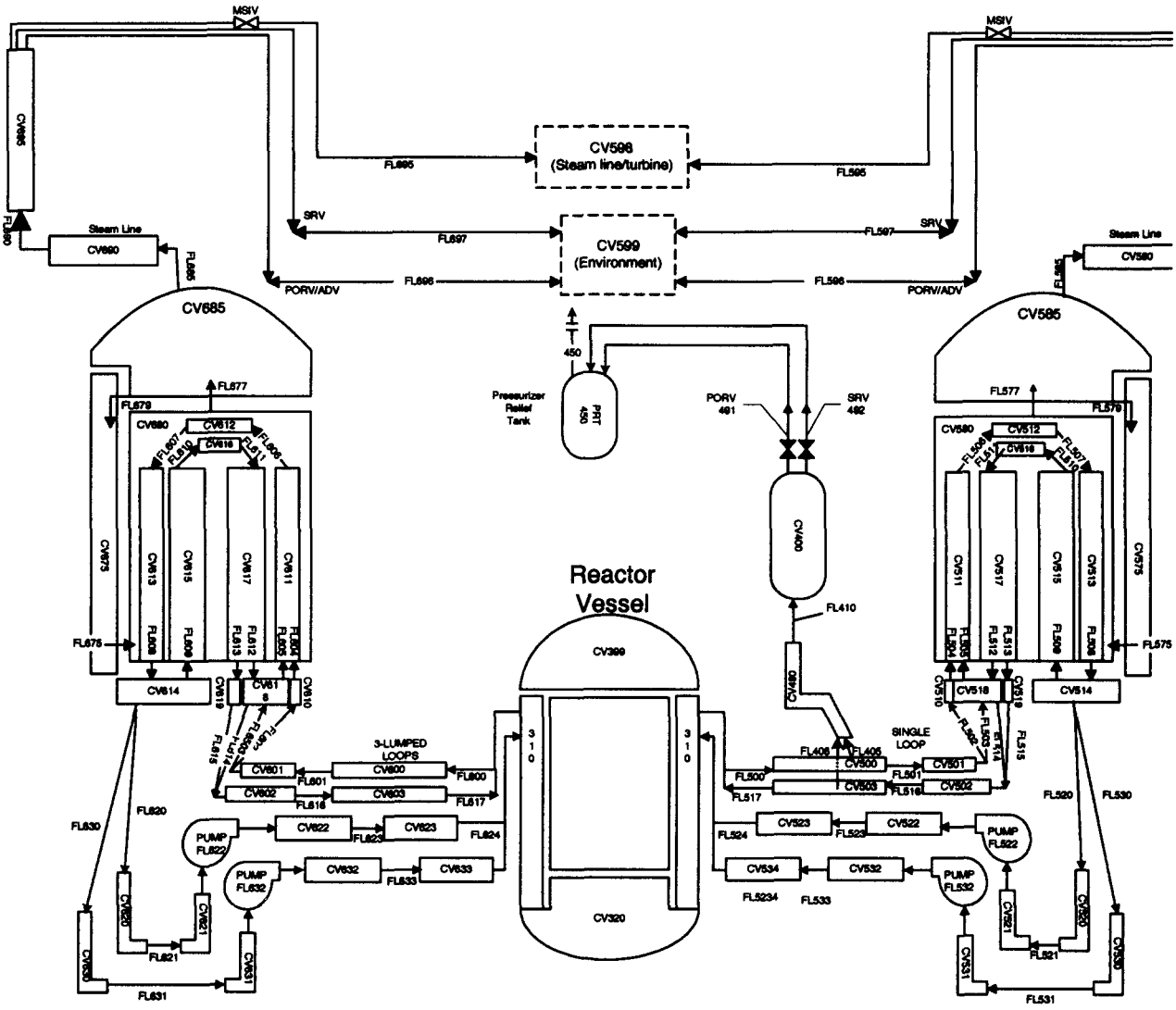

Figure 3-12 Nodalization of Westinghouse 4-loop PWR reactor coolant system used in the Sequoah MELCOR model.

Creep rupture models are applied in considering the potential failure of the hot leg nozzles, the surge line and the steam generator tubes as detailed in a previous report describing models for three Westinghouse plants [4]. These models use the RCS pressure and the heat structure temperatures to estimate cumulative damage, and when failure is predicted, a flow path is opened to allow for system depressurization at that location. In addition, both creep rupture and penetration failure models are available for the lower vessel head. In this study only the penetration failure model was exercised; the creep rupture model could delay melt ejection to the cavity owing to the fact that these analyses predict hot leg or surge line failure prior to lower head failure, hence the system is depressurized at the time of lower head loading and failure.

3.6 Containment Nodalization

The 12-cell containment nodalization for the Sequoyah Ice Condenser model is shown in Figure 3-13. Briefly, this nodalization divides the containment into 12 separate volumes. A summary of the free volumes associated with the Sequoyah CV nodalization is provided in Table 3-5.. The RCS volumes are associated appropriately with the containment volumes so that pipe breaks or lifting relief valves vent into the correct containment locations. Containment rooms are connected with the flow paths indicated with respect to the constraints offered by walls and partitions, and liquid flow paths are defined with consideration given to fill elevations required for flooding in one room to spill over to other rooms. RCS pipe ruptures will result in steam entering the bottom of the ice condenser volumes and exiting into the upper containment dome region. An alternative 25-cell containment model shown in Figure 3-14 is also available for use but was not used in this uncertainty analysis in order to reduce computation run time.

The reactor cavity in the containment is modeled as having a floor of radius 4.28m, and therefore a surface area of 57.5m2. The floor concrete is limestone concrete with iron rebar as described in Table 3-6 [5].

Table 3-5. Summary of containment control volumes and physical volume.

CV Number	Description	Volume [m^3]
1	cavity	396
2	Steam Generator doghouse - single	362.5
3	Steam Generator doghouse - triple	1,087.5
6	Reactor space	439
7	Pressurizer doghouse	135
8	Lower compartment - single	1,510
9	Lower compartment - triple	2,800
11	Lower annulus	2,556
14	Ice Condenser lower plenum	685
18	Ice Condenser Baskets	2,440
22	Ice Condenser upper plenum	1,330
24	Upper dome	18,626
	Total Volume	32,367 (1,143,029 ft^3)

Table 3-6. Composition of cavity concrete in the MELCOR model of the Sequoyah containment.

Compound	Mass Fraction [kg/kg]
SiO_2	0.36
Al_2O_3	0.03
$CaCO_3$	0.55
$Ca(OH)_2$	0.05
H_2O	0.03
Fe (rebar)	0.09

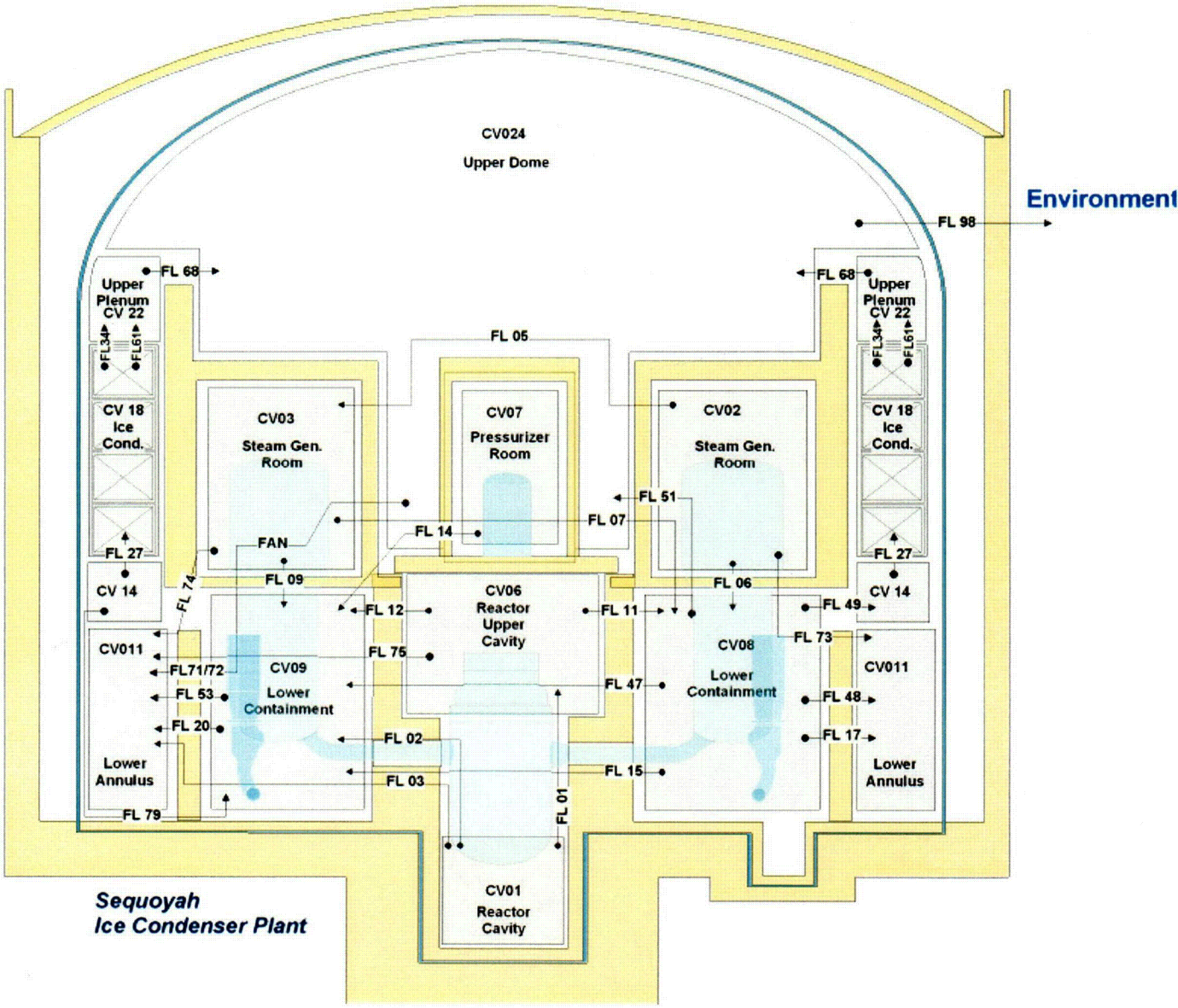

Figure 3-13 MELCOR 1.8.5 nodalization of the Sequoyah Ice Condenser containment.

C03

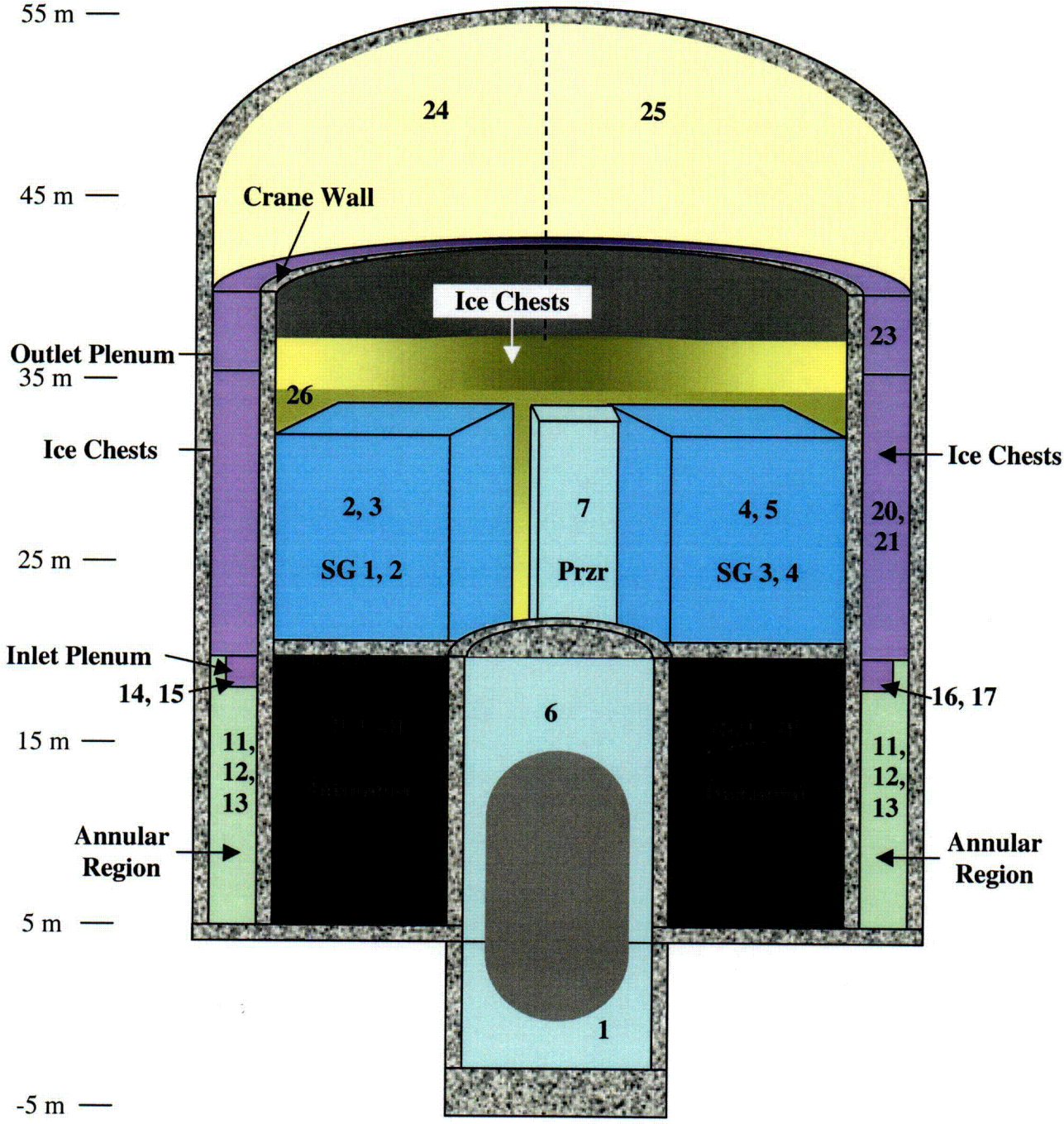

Figure 3-14 Alternative 25-cell model of Sequoyah containment - *not used in this study*.

C04

4 Characterization of Uncertainty Parameters and Distributions

4.1 MELCOR Physics Parameters Affecting Hydrogen Generation

4.1.1 SC1001 Oxidation Rate Coefficients:

The choice of cladding oxidation models or the uncertainty associated with any given model are obvious parameters to consider in evaluating hydrogen generation uncertainty. A Siemens study [6] considered different models as the principal means of exploring this uncertainty as opposed to considering variations in either the rate coefficients or exponents. The general form of the oxidation models used in MELCOR correspond to a parabolic growth rate law of the form

$$\frac{dw^2}{dt} = K(T),$$

or equivalently,

$$\frac{dw}{dt} = \frac{1}{2}\frac{K(T)}{w}$$

where w, in the case of the MELCOR implementation, is the specific mass of cladding metal (not oxide *as is often expressed by different authors*) reacted in units of [kg/m^2]. The rate of growth factor is expressed as

$$K(T) = A\exp\left[\frac{-B}{T}\right],$$

where the parameters A and B are adjusted to reflect different models. Often different values of A and B are applied over two discrete temperature regimes to reflect an observed step increase in oxidation rate when the ZrO_2 outer layer undergoes a phase change in the crystal structure near 1800K. The default values in MELCOR correspond to the Urbanic-Heidriech model for oxidation. Other similar models are of course available which can be specified via this sensitivity coefficient array. Figure 4-1 shows a number of commonly used oxidation models expressed in terms of the temperature dependent rate constant, $K(T)$. While uncertainty certainly exists for both the A and B parameters, simply varying these parameters independently over uncertainty ranges is not judged to be the best way to explore uncertainty in the models. We feel it would be preferable to vary the linear curve fit (i.e. vary the A and B in a consistent way) to the data that were used to fit the experimental data so as not to arrive at very poor or even unphysical curve fits. Alternatively, one can also simply select between different models, as Siemens did, to express the desired uncertainty. We used the latter approach since the various models would appear to encompass the typical experimental uncertainty associated with any particular oxidation model.

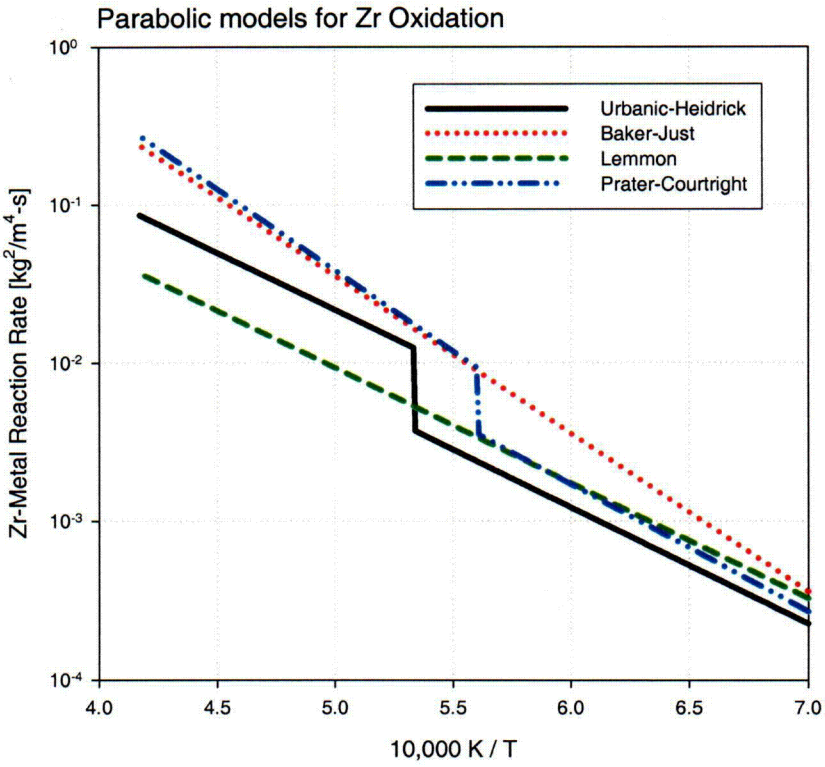

Figure 4-1 Comparison of different parabolic rate models representing zircaloy oxidation in steam.

4.1.2 SC1131 Molten Material Holdup Parameters

The MELCOR parameter that controls the retention of molten zircaloy within the outer ZrO_2 shell is probably the most important factor affecting the total amount of hydrogen produced in the early stage of core degradation. The default value is 2400K, considered to be a most likely value based upon assessment of many experimental studies, including the Phebus FPT-1 test. Highly reducing (H_2) conditions could encourage melt breakout at a lower temperature, as could protracted time encountered in the 2200K-2400K temperature range, owing to effects of oxygen profiles in the cladding oxide phase layers and on kinetics respectively. It is not considered likely that breakout could be delayed to temperatures higher than ~2500K owing to the strong tendency for Zr metal to dissolve its oxide and due to the fact that complete rod collapse by slumping and/or liquefaction seems to begin at about this temperature as evidenced from Phebus tests. A reasonable range for parameter variation is considered to be 2250K to 2500K, with a most probable value of 2400K. The Siemens report is consistent with this determination. The corresponding cumulative probability distribution taken for describing this parameter is shown in Figure 4-2.

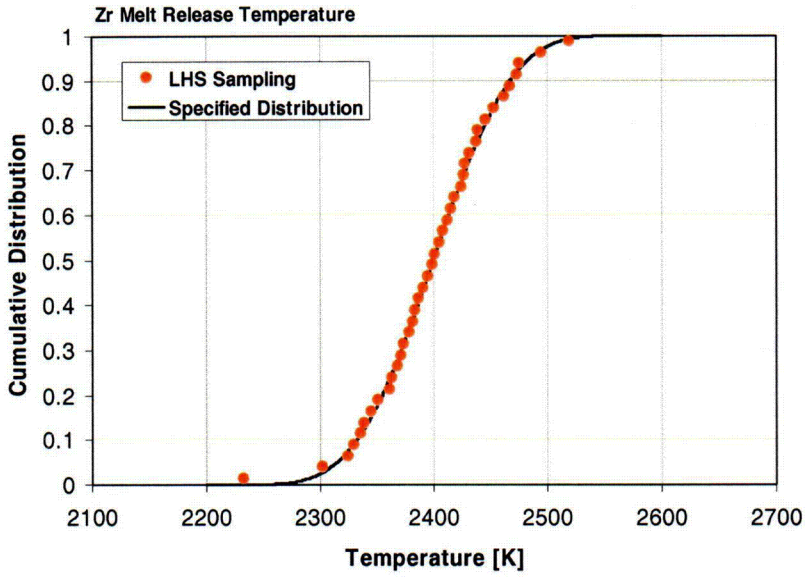

Figure 4-2 Cumulative probability distribution for molten zircaoly breakout temperature.

4.1.3 SC1132 Core (Fuel) Component Failure Parameters

The temperature at which intact fuel rods are assumed to transition from rod-like geometry to a rubble form can affect the core degradation progression, which in turn can influence hydrogen generation. The current MELCOR default value is 2500K, which represents the combined effects of eutectic interactions and fractured nature of irradiated fuel pellets. This value was considered to be a good estimate based on MELCOR assessment of the Phebus FPT-1 experiment. The French are leaning towards a value of ~2650 for this parameter based on their more recent analysis of test FPT-2. Fresh fuel could call for an increased value to as high as 2800K. Uncertainty in the 2500K could range from 2400K to 2700K, and based on the findings from Phebus FPT-1 and FPT-2 may be most likely between 2500 and 2650K. This parameter should be distributed normally about 2500K. The Siemens study reached very similar conclusions.

C06

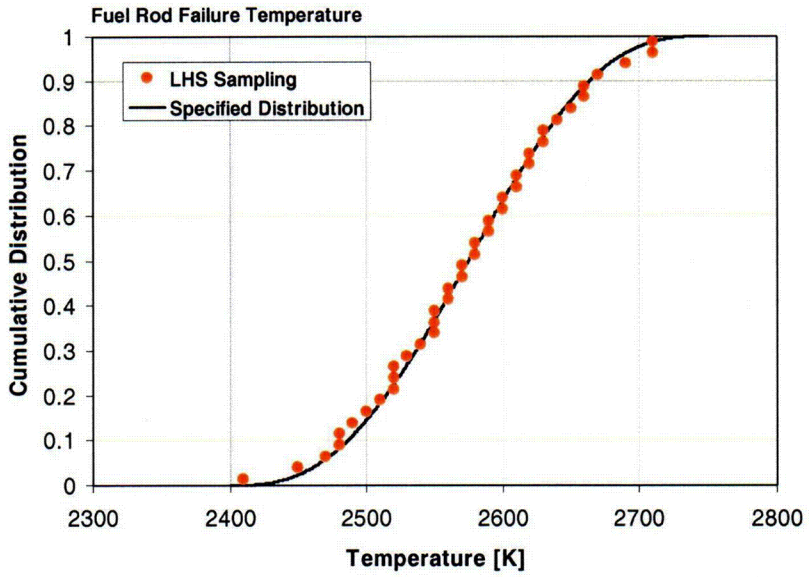

Figure 4-3 Cumulative probability distributions estimated for fuel rod collapse temperature.

4.1.4 COR00007 Secondary Material Transport Parameters

The zircaloy cladding, when molten, attacks the UO_2 fuel material by dissolving some of the fuel into the metallic melt. Later, when this molten material is released from the outer ZrO_2 layer, a fraction of the fuel material is relocated also. The MELCOR default assumes that the molten metallic cladding will incorporate adjacent UO_2 fuel material so that 20% by mass of the total melt is dissolved fuel. The effect of this phenomenon is to relocate fuel material and thereby to redistribute the decay heat source to some extent. While this phenomenon would not appear to be a first order parameter affecting melt progression, moving greater fractions of fuel material with draining Zr could move more decay heat to the locations of blockages and thermally affect blockage stability, which can subsequently influence hydrogen generation. Phase diagrams provide some guidance with respect to the range of UO_2 that can be dissolved in molten zircaloy, however experimental evidence has shown that fuel grains can be dislodged from the fuel and made mobile without becoming completely dissolved. A value of 20% UO_2 in metallic melts is considered typical and the MELCOR default for this parameter is justified on this basis, however, a range of fuel attack has been observed in experiments. The distribution shown in Figure 4-4 reflect reasonable ranges of dissolved UO_2 proposed for this study, with 20% being the most probable and the range bracketed between 0 and 50%. It should be emphasized that the mathematical representations do not imply suggest anything about the underlying physics that might be influencing the distribution. They simply reflect our intuitions concerning the likelihood of their particular value.

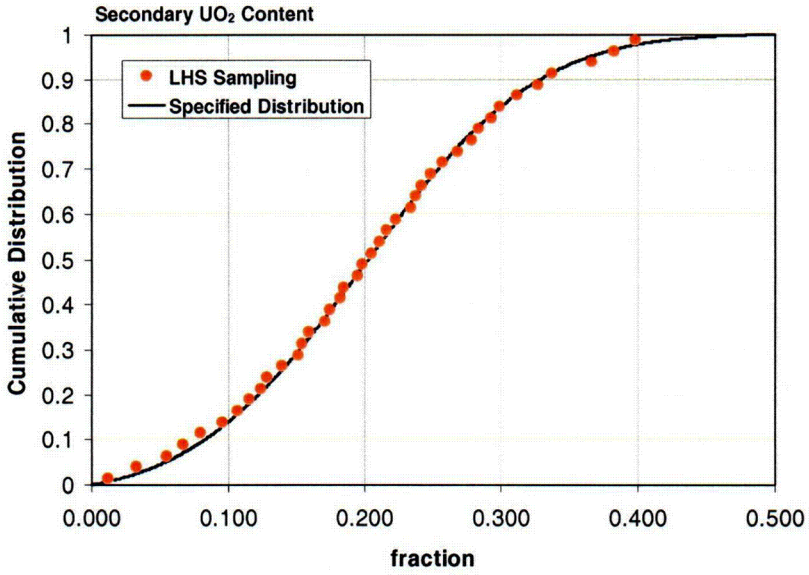

Figure 4-4 Cumulative probability distribution describing dissolved UO_2.

4.1.5 Parameters Affecting Freezing Versus Draining of Relocating Core Materials

Materials melting and relocating within the reactor core, particularly fuel-laden metallic zircaloy, can either freeze in cooler regions of the core to form blockages, or drain to the core plate or lower plenum, depending on the modeling of the freezing process. MELCOR parameters affecting this phenomenon include the fuel/cladding gap conductance and the melt/cladding (candling) heat transfer coefficient. Since irradiated fuel is generally swollen and the fuel/cladding gap dimension is very small, we propose minimizing the gap resistance by assuming a negligible gap dimension.

4.1.6 COR00005 Candling Heat Transfer Coefficients

The COR0005 parameters, along with the gap conductance controls (COR00001 record) affect the tendency to form blockages by the freezing of relocating melts, principally molten Zircaloy, but also molten steel. Because MELCOR does not use a separate field for molten material, any melt which begins to relocate will be distributed somewhere below the point of release during a single time step. A velocity of relocation is not modeled; hence the concept of a heat transfer coefficient used in this context is not the normal one. The heat transfer coefficient is applied over the time step interval (*generally much smaller than the characteristic time for melt to transit the COR cell were a relocation velocity to be considered*) to move heat from the melt at temperature T_{melt}, to the underlying surface at temperature T_{surf}. The amount of heat rejected in freezing a given mass of melt is also limited by the heat capacity of the surface material (i.e. cladding) and some fraction of the fuel

C08

pellet (in MELCOR version 1.8.5). The degree of participation of the fuel pellets is influenced by the thermal resistance of the fuel-cladding gap, a function of the gap dimension and the gap gas conductivity. MELCOR modeling in this area is presently undergoing improvement; nevertheless we can explore this uncertainty by increasing the heat transfer coefficient appropriately. The following paragraphs develop some insight into appropriate values for the candling heat transfer coefficient, giving consideration to the thermal conductance of the materials involved and the actual time of heat transfer appropriate to the process which is considerably longer than the MELCOR computational time step.

A simple conduction analogy where conduction heat transfer is equated to the heat transferred by the heat transfer coefficient approximation is expressed as:

$$Q = -k\frac{dT}{dr}A\,\Delta t \equiv h\,A\,\left(T_{melt} - T_{surf}\right)\Delta t\,.$$

From this, we can estimate h to be on the order of

$$h \approx \frac{k}{dr},$$

where k is the mean thermal conductivity of the materials and dr is the characteristic radial dimension for heat conduction, reasonably on the order of .5 cm for melt draining into a rod geometry. Values of k could range from 2 W/m-K to 50 W/m-K for metallic UO_2 and zircaloy respectively. Using these values we can come up with numbers for h in the range of **250 to 6,000 W/m^2-K**. Moreover, since MELCOR completes the relocation of draining materials during a single time step (*having no separate computational field with which to track a molten component*), the heat transfer coefficient must also account for the fact that the draining melt might otherwise transfer heat to the same cladding and fuel over many time steps for melts that have a *cooperative* relocation velocity. Measurements taken from video observation of CORA experiments reveal that, while some free-falling molten droplets relocate very rapidly, most of the downward draining melt moves more on the order of millimeters per second, justifying much increased values of the candling heat transfer coefficient, as will be subsequently explained.

Considering that a typical axial node is about 60 cm and relocation velocities could range from 1 m/s for very fast drainage to 2 mm/s for slow drainage, melt transit times can therefore range between on the order of a second to a few hundred seconds. Given that MELCOR numerical time steps are on the order of .1 to .01 sec (or shorter) during core degradation, we are justified in enhancing the heat transfer coefficient range of 250 to 6000 watt/m^2-K by factor of between 10 and 1000, or even more. In view of this, we have specified the distribution of heat transfer coefficients as shown in Figure 4-5. It can be pointed out that the present MELCOR default value for this parameter is 1000 watt/m^2-K. In truth, even after the preceding argument for truly large values for this parameter, we ultimately assign likelihood for this parameter biased somewhat to the low end of values discussed, principally to avoid using values that are too different from those commonly used by present MELCOR users (and the current default value). At the same time we also use a log-normal form to ensure that half of the LHS cases sampled use values between about 5,000 and 10,000 watt/m^2-K (see Figure 4-5).

Having made the preceding arguments on heat transfer rates and characteristic time scales, it is important to realize that use of a high heat transfer coefficient does not result in the freezing of a large mass (i.e. complete blockage) unless sufficient heat sink is available to absorb the latent heat. The heat sink is affected by the degree of thermal participation of the underlying fuel pellets.

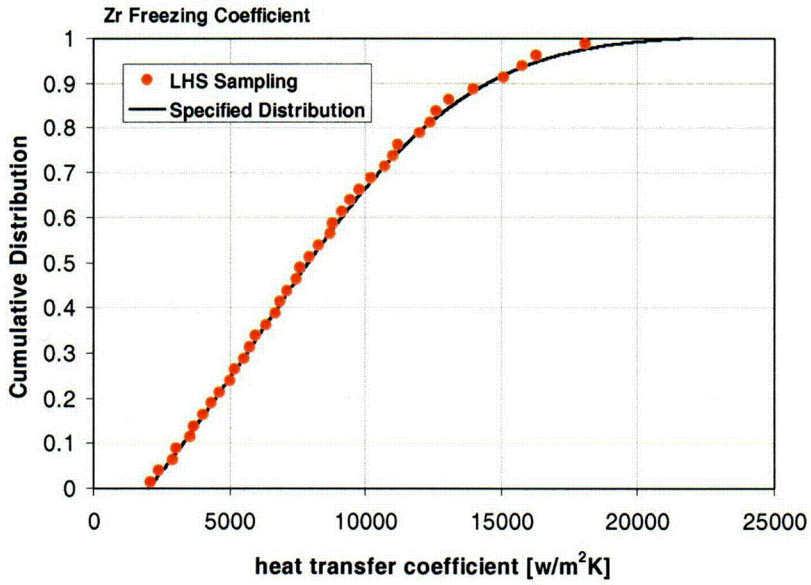

Figure 4-5 Cumulative distribution proposed for the candling heat transfer coefficient.

4.1.7 Particulate Debris Characteristics

The characterization of particulate debris affects heat transfer and oxidation of core materials following their loss of rod-like geometry. The size of the debris may be specified on a cell-by-cell basis. The value specified for regions that were once intake fuel rods should reflect the character of the initially formed fuel debris. In the lower plenum regions, however, this parameter should reflect the character of debris that has perhaps become molten or formed conglomerates of smaller debris constituents. In the following we specify different debris characteristics for the core regions and the lower plenum.

Core-Region Particulate Debris Diameter: When the fuel rods have reached a certain critical temperature above which it is deemed that loss of stability must occur, the fuel materials are converted be MELCOR into particulate debris. The user supplies a characteristic diameter for this debris in order to evaluate subsequent heat transfer and oxidation surface areas. The particulate debris will fill available space on formation and after relocation, limited by a presumed characteristic debris porosity. Particulate debris diameter is defined on the **CORijj04** record. In view of the fact that fuel pellets are on the order of a centimeter in diameter, it would seem reasonable for particulate debris to range in size between centimeter-sized particles to a few millimeters. Siemens' view of this

C09

parameter is consistent with this. The distribution specified for particulate debris diameter is showin in Figure 4-6.

Lower Plenum Particulate Debris: When debris materials relocate to the lower plenum region it is likely that the core materials have become sintered or fused to form larger conglomerates. The relocating material may even be in a molten form. In either case, it is expected that the characteristic size will be considerably larger than the roughly millimeter size of the core region debris. Molten material relocating downward may exhibit a characteristic size more on the order of ~5 cm if relocating as a stream, perhaps draining through holes in the lower core structures. The principal effect associated with this parameter is on the heat transfer to lower plenum water. Certainly, the extremely large surface area associated with an assumption of millimeter sized particles (as in the core region) would over-predict the fuel-coolant interaction, although if molten materials are involved, some jet fragmentation with enhanced heat transfer could be reasonably expected. While detailed fuel coolant interaction modeling is beyond the scope of this study, we seek to accommodate some effects associated with this phenomena. We specify a range of debris sizes between 1 cm and 10 cm to reflect the aforementioned arguments. Unfortunately little basis other than intuition can be provided to rationalize this assumption.

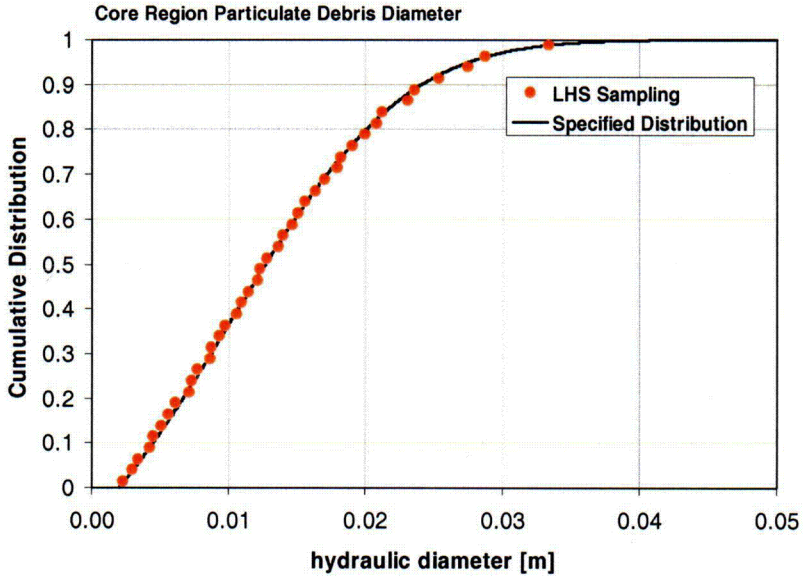

Figure 4-6 Cumulative probability distribution for core region particulate debris diameter.

C19

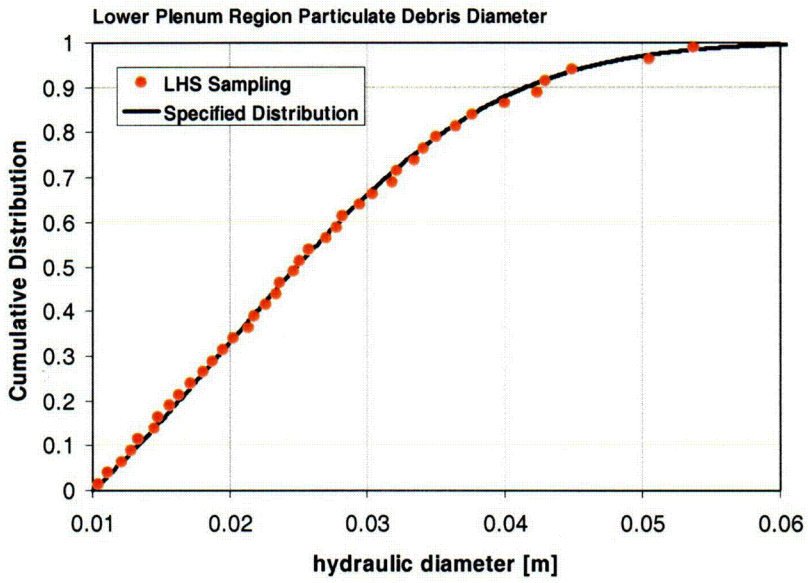

Figure 4-7 Cumulative probability distribution for lower plenum region particulate debris diameter.

Debris porosity (PORDP): PORDP is defined on the CORZjj01 records and should be centered at a value of 0.4 and varied between 0.1 and 0.5. Greater porosity cannot be considered structurally stable, and lesser porosity cannot reasonably achieved by random packing of solid debris particles. Experience in this regard is derived from characterization of the TMI-2 upper debris bed and from insights from both the MP-1 and 2 debris bed tests and the more recent FPT-4 experiment in the preparation of debris beds from particulate similar in size to TMI-2 debris. Siemens considered porosity between 0.05 and 0.3 with 0.3 as their guess as the most probable. The lower range used in the Siemens study may have been selected as a surrogate to simulate sintering or fusing or particulate by intrusion of molten material. Since MELCOR models exist to accommodate this phenomenon, we are not inclined to lump this effect into this parameter. The distribution function for the debris porosity is provided in Figure 4-8.

4.1.8 COR00012 In-Vessel Falling Debris Quench Model Parameters

The principal parameters governing quenching of debris relocating into the lower plenum are the falling debris heat transfer coefficient and the prescribed falling velocity. The defaults values of 100 W/m^2-K and 1 m/s were used in the Sequoyah cases. As discussed earlier, all particulate debris, whether solid particles or molten materials, are characterized with an effective diameter. The diameter implies a total surface area that is the sum over all particles formed from the relocation of a quantity of material. Effects such as the boiling caused by neighboring particles, which will impair heat transfer, must be reflected in value of the heat transfer coefficient.

In order to gain some insight into possible values for the heat transfer coefficient to be used here, we can consider the heat transfer predicted for a single spherical particle falling through a fluid. An appropriate correlation is available in Bird, Stewart and Lightfoot as follows.

$$\frac{h\,D}{k} = 2.0 \quad + \quad 0.6 \cdot \left(\frac{D\,V\,\rho}{\mu_f}\right)^{1/8} \left(\frac{C_p\,\mu}{k}\right)^{1/3}$$

Using values typical for water and corium, the following relationship between particulate diameter and heat transfer coefficient results as shown in Figure 4-9 below. Without interference from other particles in the swarm of particulate typically falling through the lower plenum water, heat transfer coefficients as high as 10,000 watt/m^2 K can be predicted for small particles. However, it is not possible for all particles to encounter such ideal conditions. Due to swarming effects and boiling induced by neighboring particles we might estimate that the effective heat transfer coefficient for falling debris would be only about 5% of that for a single particle if we assumed only 5 percent of the melt mass actually participated effectively and heat transfer. Were this the case, the effective heat transfer might be as suggested in Figure 4-9.

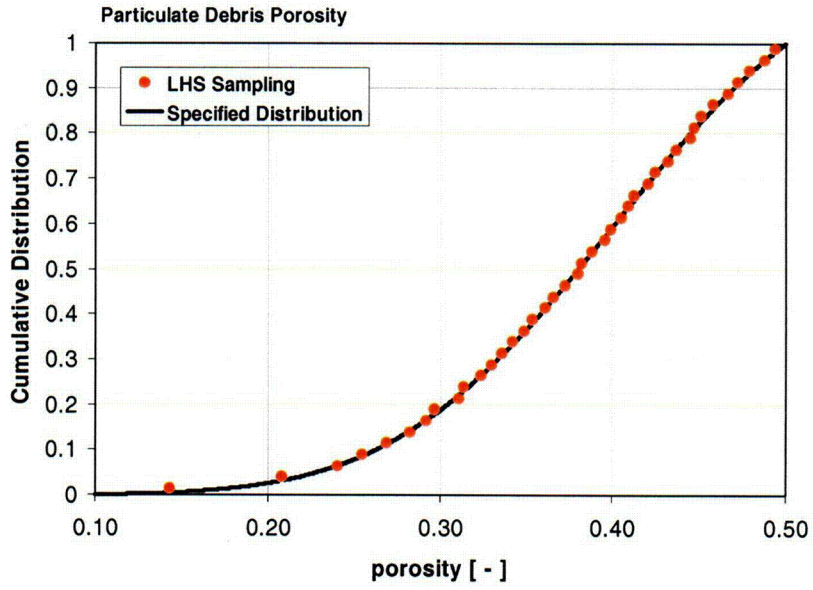

Figure 4-8 Cumulative distribution for debris porosity.

C12

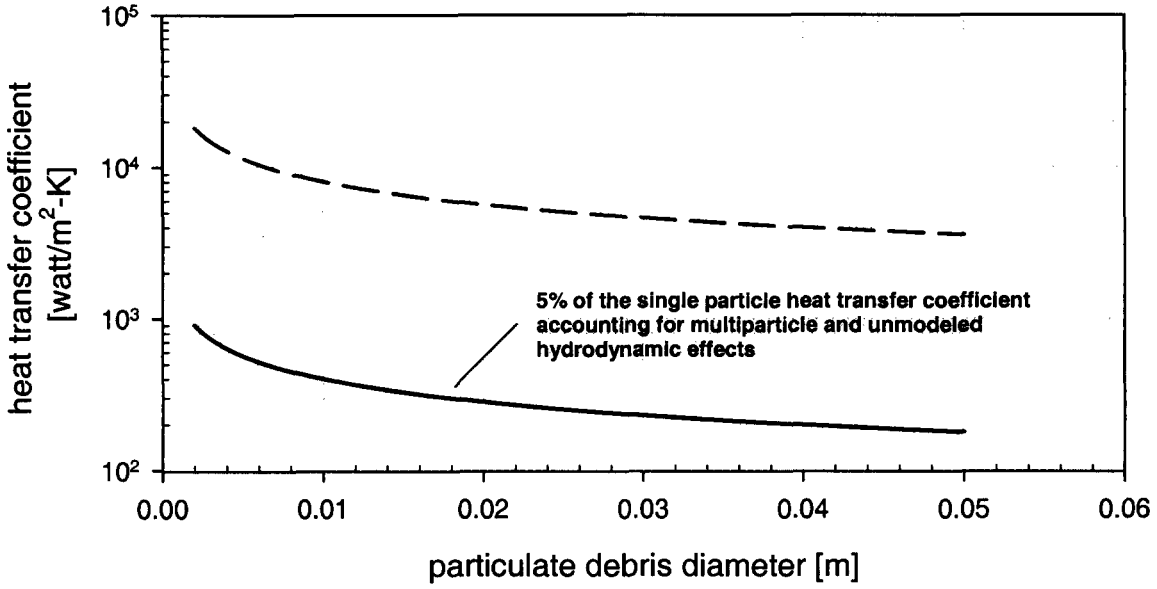

Figure 4-9 Heat transfer coefficient recommended to be associated with particulate debris diameter.

A review of the FARO experiments [7], involving molten masses on the order of 150 kg, shows generally that fragmented particle sizes are on the order of five millimeters. Using this information together the stated energy transfer during the approximately two second quenching time in these experiments, one arrives at a heat transfer coefficient on the order of 1000 watts/m^2K. This value is significantly lower than that suggested for the ideal single particle heat transfer coefficient shown in Figure 4-9, and is fairly close to the 5 percent value shown in the same figure. We take this to be indirect evidence that highly ideal heat transfer does not occur, and that use of a "de-rated" 5 percent value leads to not-unreasonable values. The FARO tests showed high percentages of melt fragmentation. It seems doubtful that such complete fragmentation as observed in the 150 kg Faro tests could be realized in the 10000 to 30,000 kg melt relocation events calculated by MELCOR. Instead, we expect some fraction of a realistic melt relocation event to fragment as observed in FARO, and a larger fraction to arrive on the lower head without fragmenting.

Finally, recent MELCOR analyses have been performed wherein roughly 30,000 kg relocation events are predicted. These analyses produce in-vessel pressurization events on the order of 3 MPa when 2 cm debris are assumed with 1 m per second relocation velocity and 100 watt/m^2K heat transfer coefficient. The selection of parameters seems to produce pressurization events quite similar to that observed in the TMI-2 accident.

Based upon the preceding arguments and order of magnitude analyses, we specify the following distribution to be used in order to capture uncertainty associated with falling debris heat transfer. We recognize that this characterization does not envelope the kinds of pressurization's that might be expected from steam explosions. We expect this characterization, together with the variation in

lower head debris size, to result in vessel pressurization's ranging from minimal to on the order of 10 MPa, with a mean value on the order of 3 MPa.

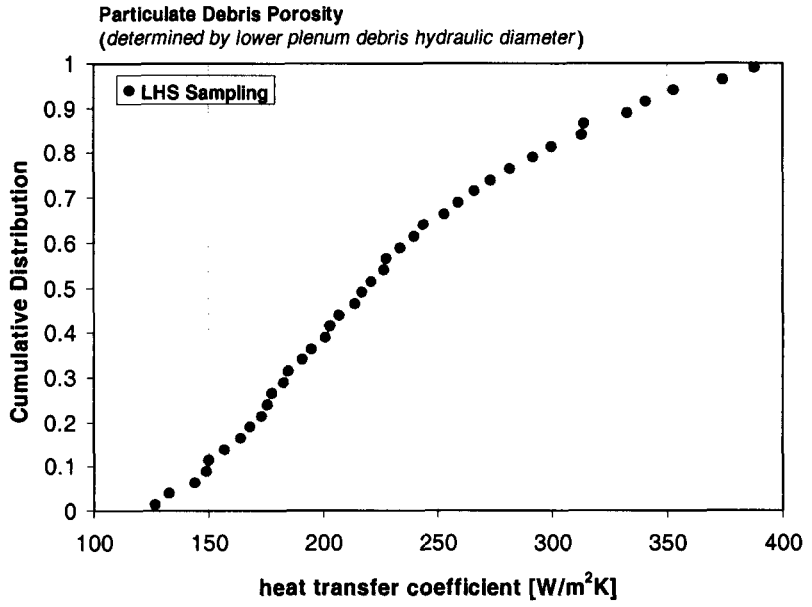

Figure 4-10 Cumulative distribution proposed for falling debris heat transfer coefficient.

4.1.9 COR00003 Radiation Exchange Factors: FCELR and FCELA

The calculation of radiation heat transfer in complex geometries such as that of a reactor core is computationally a very challenging problem to perform correctly. The radiation transport models in MELCOR are extremely simple in this respect. The MELCOR parameters used to control radiation transport are summarized below. Default values for these parameters are indicated in parentheses.

```
FCNCL - fuel cladding to canister wall factor (.25); BWR only
FSSCN - blade to canister wall factor (.25);BWR only
FCELR - radial cell to cell exchange factor (.25)
FCELA - axial cell to cell exchange factor (.25)
FLPUP - exchange factor from pool to core (.25)
```

Most important in the global heat transport in the reactor core are the radiative couplings between COR cells, axially (FCELA) and radially (FCELR). This was generally confirmed by the Siemens study that found the parameter FCELR (radial exchange between COR cells) to have the greatest effect on hydrogen production. This is as opposed to the coupling between say fuel rods and fuel canisters in BWRs that exist *within* a COR cell. For example, the radiation transport radially between two COR cells of height, h, at the cell radius of r, would be calculated as something like $\sigma\varepsilon\left(T_2^4 - T_1^4\right)\cdot\left(2\pi rh\right)\cdot F$, where F is a "view factor" between the two cells with temperature T_1 and T_2, and σ and ε are the Stefan-Boltzman constant and emissivity respectively. The actual calculations is more complex, invoking reciprocity and gray gas participation as described in the MELCOR COR

Manual Reference Guide, however, the preceding general form expresses the essential character of this calculation. While the following simplification does not do justice to the true complexity of the problem, we can argue that radiative coupling, represented by the view MELCOR radiative view factor, should be somewhat proportional to the volume of the COR cell that can "see" the adjacent cell, relative to the total COR cell volume. This can be expressed by the ratio

$$F \approx \frac{\left([r_1 - \delta]^2 - r_1^2\right)}{r_1^2 - r_0^2}$$

where δ is the radial thickness of the core cell defined by the volume $(r_1^2 - r_0^2)\pi h$ which is coupled radiatively to the adjacent COR cell. For rod bundle geometry the view factor for rod-to-rod radiation (i.e. radial), when viewed as "rows" of rods, becomes vanishingly small after more than 3 rod rows, or beyond $\delta \cong$ 5cm for example. For a typical reactor core region cells, the radial factor based on this ratio of radiatively coupled volumes is on the order of 0.1. Strong radiative coupling across only 2 rod rows, or over a distance of 3cm, reduced this view factor to the order of 0.05. Axial factors would not be very different although axial conduction is also participating in this case. This does imply a COR cell size dependence of the radiation factors, and smaller core volumes, for example like the COR cell volumes used in the analysis of Phebus experiments would warrant considerably larger view factors, approaching the 0.75 to 1.0 range.

The ranges used by Seimens for FECLR and FECLA were 0.01 to 0.25 and 0.02 to 0.3 respectively, and based on our order of magnitude analysis presented above, we generally concur with this range. The following distribution (Figure 4-11) we feel adequately expressed the likelihood for both the axial and radial factor, which we feel should be equal for both axial and radial radiation calculations given the approximate nature of the underlying calculation.

4.1.10 Uncertainties in Ex-Vessel Molten Core Concrete Interaction Modeling

This final section addresses uncertainty in the modeling of interactions between molten core materials and the concrete of the cavity below the vessel (MCCI). These phenomena are treated by the CORCON model in MELCOR. Perhaps needless to say, without overlying water, the core materials are generally not coolable and MCCI proceeds to completion, producing large quantities of hydrogen as well as non-condensable CO and CO_2. In the presence of overlying water however, many researchers argue that such configuration ought to be coolable owing to water penetration into the crust and breakup of the insulating crust. In general, the CORCON model assumptions are such that quenching of core debris by overlying water in the cavity region can occur only is the debris layers are very thin. This is due to the significant thermal resistance offered by the surface crusts at the water interface and resting upon the concrete.

In order to explore uncertainty with respect to the amount of heat removal that can be removed by overlying water pools, the CORCON model will be adjusted to allow greater amounts of heat to be removed from the otherwise highly insulating crusts. This is accomplished by increasing the effective thermal conductivity of the crust material in order to simulate much shorter conduction path lengths that might be present if surface cracks are present in the crust. With these modifications, the limiting

factor in heat removal is that which can be transferred to the overlying water by means of the crust to water heat transfer coefficient.

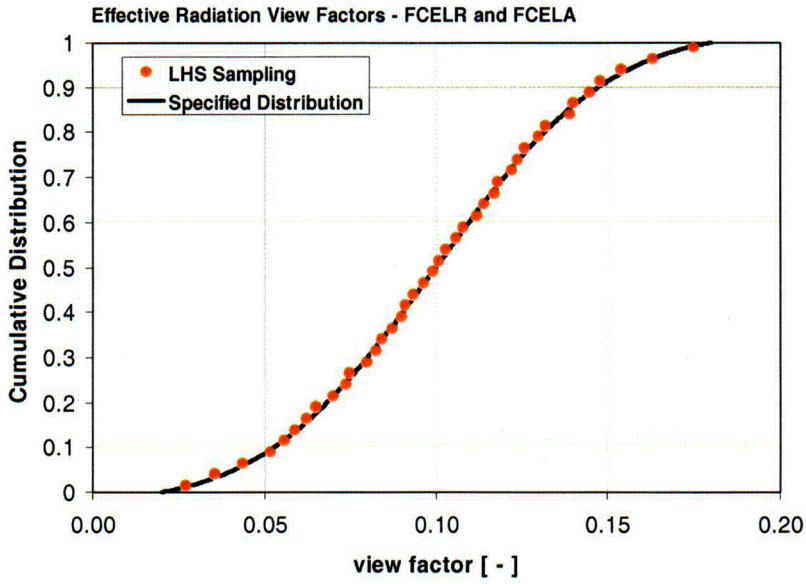

Figure 4-11 Proposed cumulative distribution of COR radiative view factors FCELA and FCELR.

This is illustrated in the following two figures. Figure 4-12 shows predicted debris temperature for the default CORCON modeling and two other cases, one with only the pool heat transfer coefficient increased and another with both the pool heat transfer coefficient and the crust conductivity increased. It can be seen that increasing pool heat transfer alone cannot increase the cooling rate, but increasing the crust conductivity together with an increase in the crust conductivity can produce debris cooling by overlying water. Figure 4-13 shows the predicted heat flux rejected to the water for these cases. This allows the user to effective control the heat flux rejected to the water pool and allow for the possibility of cooling and mitigating the MCCI. We propose to parameterize the heat flux rejected to the water by appropriate adjustment of the heat transfer coefficient, based on observations from experimental studies of MCCI (MACE) or on projections of expected cooling behavior from other experts. A distribution of heat rejection ability can therefore represent uncertainties in this area of admittedly diverse opinion.

Based on reviewing test data from the MACE 8 program, we are characterizing heat rejection in term of the peak initial heat rejection rate observed in experiments. Peak heat flux rejected in MACE tests range from 2000 to 5000 kW/m^2; however, CORCON-predicted peak heat fluxes using default parameters can be significantly lower. Figure 4-14 shows CORCON-predicted heat rejection for 80MT corium that is deeply flooded by water using the conductivity multipliers described earlier for several different values. Multipliers near 1 are typical of default CORCON application and result in peak heat fluxes of about 400 kW/m^2, whereas multipliers above 10 produce results that are more

C13

typical of those observed in MACE tests. The effect of the different heat rejection rates on corium cooling is shown in Figure 4-15.

Figure 4-16 show the distribution function prescribed for the characterization of ex-vessel corium cooling. The distributions are specified so that the median of the distribution reflect the approximate division from configurations that are coolable and those that are not, reflecting approximately the diversity of scientific opinion on this subject.

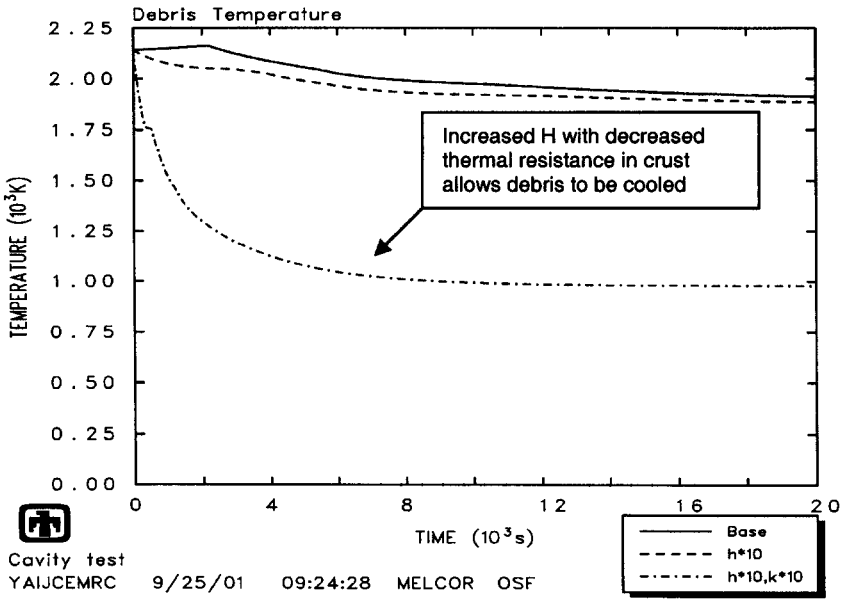

Figure 4-12 Predicted cavity debris temperature for default and modified CORCON analysis of MCCI in a Sequoyah cavity.

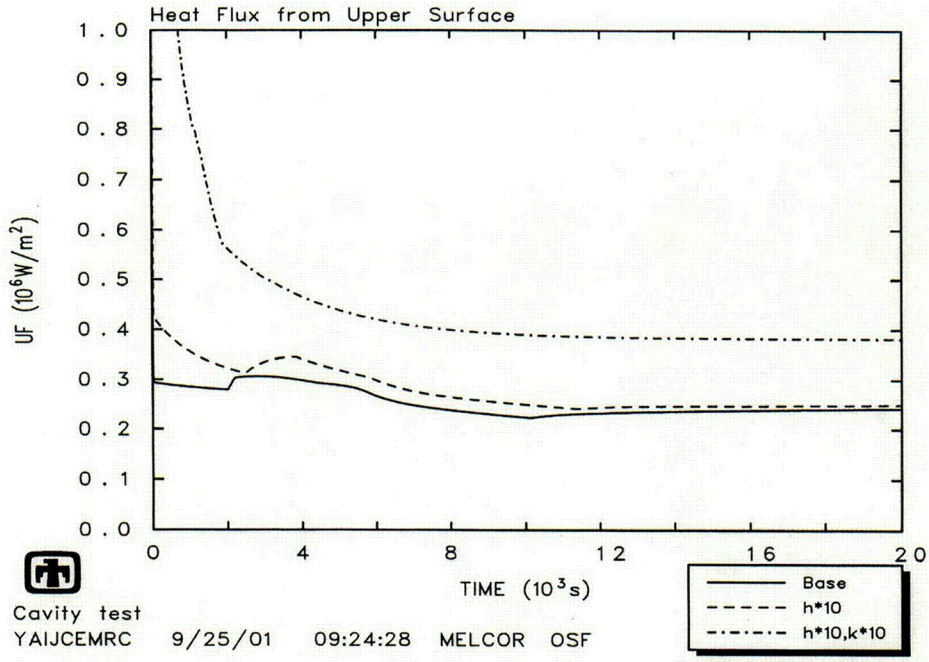

Figure 4-13 Predicted heat flux to the pool for default and modified CORCON analysis of MCCI in a Sequoyah cavity.

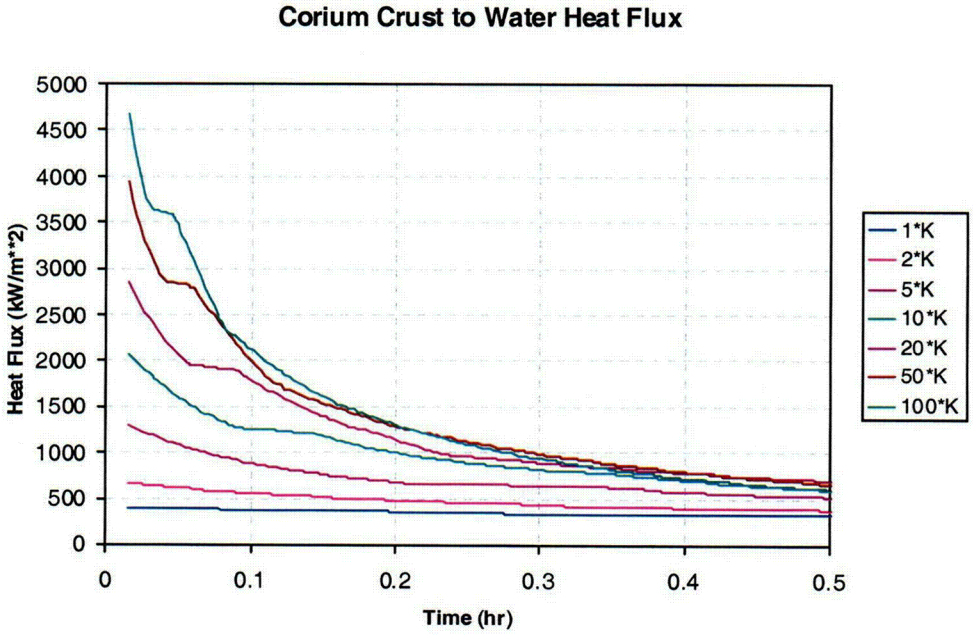

Figure 4-14 Heat rejection for different values of the conductivity multiplier.

C14

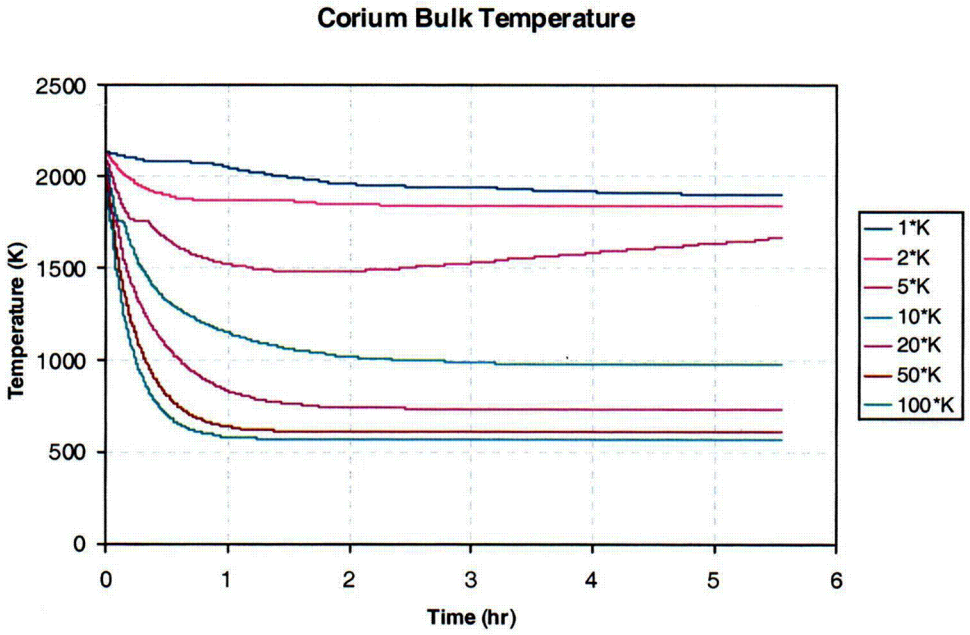

Figure 4-15 Corium cooling resulting from different values of the conductivity multiplier. The concrete ablation temperature is 1650K.

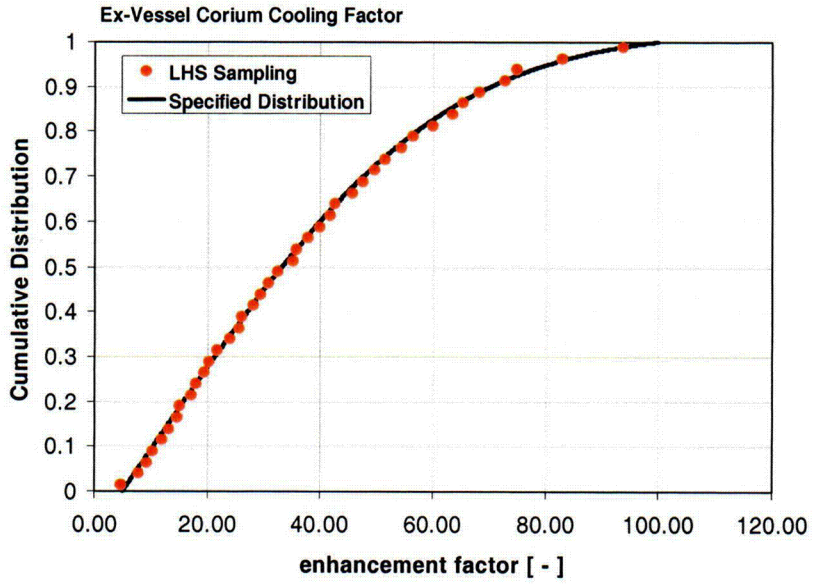

Figure 4-16 Proposed cumulative distribution for ex-vessel debris cooling.

4.2 Parameters Considered of Lesser Importance and Omitted from Study

4.2.1 COR00006 Various Model Switches

The MELCOR default values were used for the following considered parameters. We include this discussion to indicate that these parameters were considered and subsequently dismissed for inclusion in the uncertainty study.

4.2.2 COR00008 Component critical minimum thickness

These parameters are not considered to be significant presently in light of MELCOR 1.8.5 modeling of molten cladding breakout. More important are the sensitivity coefficients associated with cladding oxide failure and melt release.

4.2.3 SC1101 Fuel/Cladding gap emissivities:

There is generally no appreciable difference between cladding and fuel temperatures hence these parameters are judged to be unimportant for this study. (Fuel=0.8/Clad=0.325 ; Low Importance)

4.2.4 SC1020 Radial Relocation Time Constants

These affect the rate of radial relocation from ring to ring of either solid debris material or molten materials that may be supported by complete underlying blockages. Significant changes (upwards) in the default values for these parameters were made in the 1.8.5 release of MELCOR, based mostly on recommendations from ORNL and on intuitive reasoning with respect to smooth behavior in the melt progression. The previous values (short time constants) produced sometimes-erratic behavior that did not seem physically reasonable. Siemens uncovered sensitivities here and explored ranges below those currently recommended in the MELCOR 1.8.5 defaults. At this point, we do not recommend varying these parameters for this study as sensitivities to hydrogen are not expected from variations about the currently used values. Additionally, the basis for variation of this parameter would be difficult to rationalize.

4.2.5 SC1600 Larson Miller (LM) Parameters for Vessel Failure

Other issues concerning the transfer of heat to the lower head are judged to be dominant over the parameters of the LM models.

4.2.6 SC4413 Flow Blockage Model flow resistance parameters

The defaults here are the Ergun equation values that increase the pressure drop in a partially blocked COR cell based on open porosity and on particulate debris size. Decreasing the particulate debris size will increase flow resistance. As the cell porosity decreases, the flow resistance will also increase. Factors affecting this include the refreezing parameters discussed earlier. A minimum attainable

porosity of 0.001 is imposed via SC1503 which should for practical purposes stop all flow through a cell. Use of the flow blockage model is always recommended; however, varying these parameters is probably not profitable. Rather we defer to varying the freezing parameters and the particle size for debris.

5 Method of Sampling Uncertain Variables

5.1 Latin Hypercube Sampling (LHS)

LHS is Sandia's Latin Hypercube Sampling Software for performing standard or stratified, Monte-Carlo, multivariate sampling (Wyss and Jorgensen, 1998). In the current study, LHS provided a mechanism for creating multiple MELCOR input files to characterize the uncertainty in the variables that are thought to have the greatest effect on the production of hydrogen during a severe, nuclear-reactor accident. While LHS allows uncertain variables to be correlated, this feature was not employed in the current study because the variables were considered to be independent. For example, in atmospheric dispersion modeling, cross-wind and vertical dispersions are often considered to be correlated because wind conditions that produce large dispersions in the cross-wind dimension generally produce large dispersions in the vertical dimension. In the current study, no correlations between the uncertain variables were apparent or could be justified.

Each of the uncertain input variables was sampled using LHS and forty input files (i.e., realizations) were created. Because of the way the LHS software is designed, each of these realizations were equally likely based on the assigned distributions. This property of LHS (and Monte-Carlo techniques in general) facilitates statistical analysis of the final results.

5.2 DesktopPA

DesktopPA (Desktop Performance Assessment) was created to implement performance assessment of the WIPP (Waste Isolation Pilot Plant) site. This code integrates user input of probability distributions for uncertain input variables, random sampling using LHS, creation of a set of input files or realizations, and limited graphical and statistical analysis of the results. DesktopPA was used as the interface for creating the 40 MELCOR input files and, in a limited capacity, for evaluating the results.

The DesktopPA tool was modified to integrate the MELCOR input file structure into DesktopPA. Once this was done, a MELCOR input file for a specific plant was converted into a template following the process described in the next paragraph. In addition, DesktopPA was extended to read the MELCOR plot file and construct a database of results. The database can then be used to extract results, create plots, and perform simple statistical analyses, such as calculating means and percentiles.

The process for creating a template file began by taking a set of MELCOR input files (a master file and others that are read into the master file) for a specific plant and converting them into a single file that had been stripped of any comment lines. Input variables that were to be treated as uncertain had to be "exposed." The "exposed" variables were later replaced by values generated by LHS sampling.

The next step in the process was for the user to assign probability distributions for each uncertain input variable. DesktopPA currently supports only a subset of the more than 30 distribution types

allowed by LHS. The probability distribution in the DesktopPA suite that proved to be most versatile for the current application was the user-cumulative distribution, which allows the user to specify a piecewise linear cumulative distribution function. The process of inputting a probability distribution is illustrated in Figure 5-1 for the hydraulic diameter of particulate debris in the lower plenum. A probability distribution is assigned by completing the table shown in the figure.

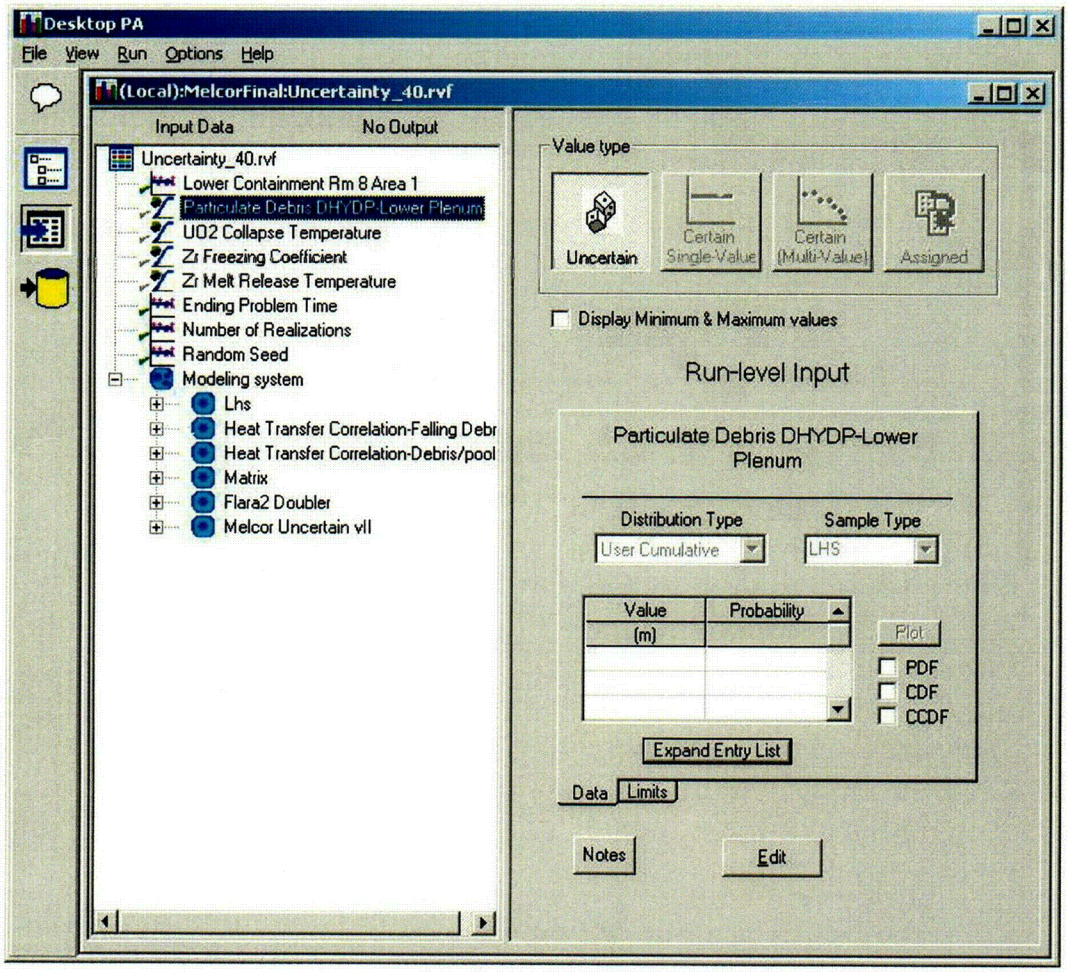

Figure 5-1. Illustration of the process of assigning a probability distribution to a MELCOR input variable.

DesktopPA automates the process of taking the realizations created by LHS and converting them into a set of MELCOR input files. MELCOR was executed for each of these input files, as described in the next subsection.

After completing the set of MELCOR runs, the plot file data were read into a SQL database. Data could then be extracted and plotted, as illustrated in Figure 5-2. Furthermore, simple statistical analyses were applied to the results to generate a mean and percentiles, as illustrated in Figure 5-3. Finally, data could be exported for further analysis by other software. For the current study, a regression analysis was applied to determine which input variables were most responsible for the variability in hydrogen production. This method and the results are described further in Section 7.

C16

5.3 Code Execution

MELCOR was run on a cluster of DEC Alpha 700 MHz processors. This cluster contains over 100 processors and it was possible to run all 40 calculations simultaneously. Thus, the entire set of MELCOR runs needed for this study was completed in about 5 days of real time.

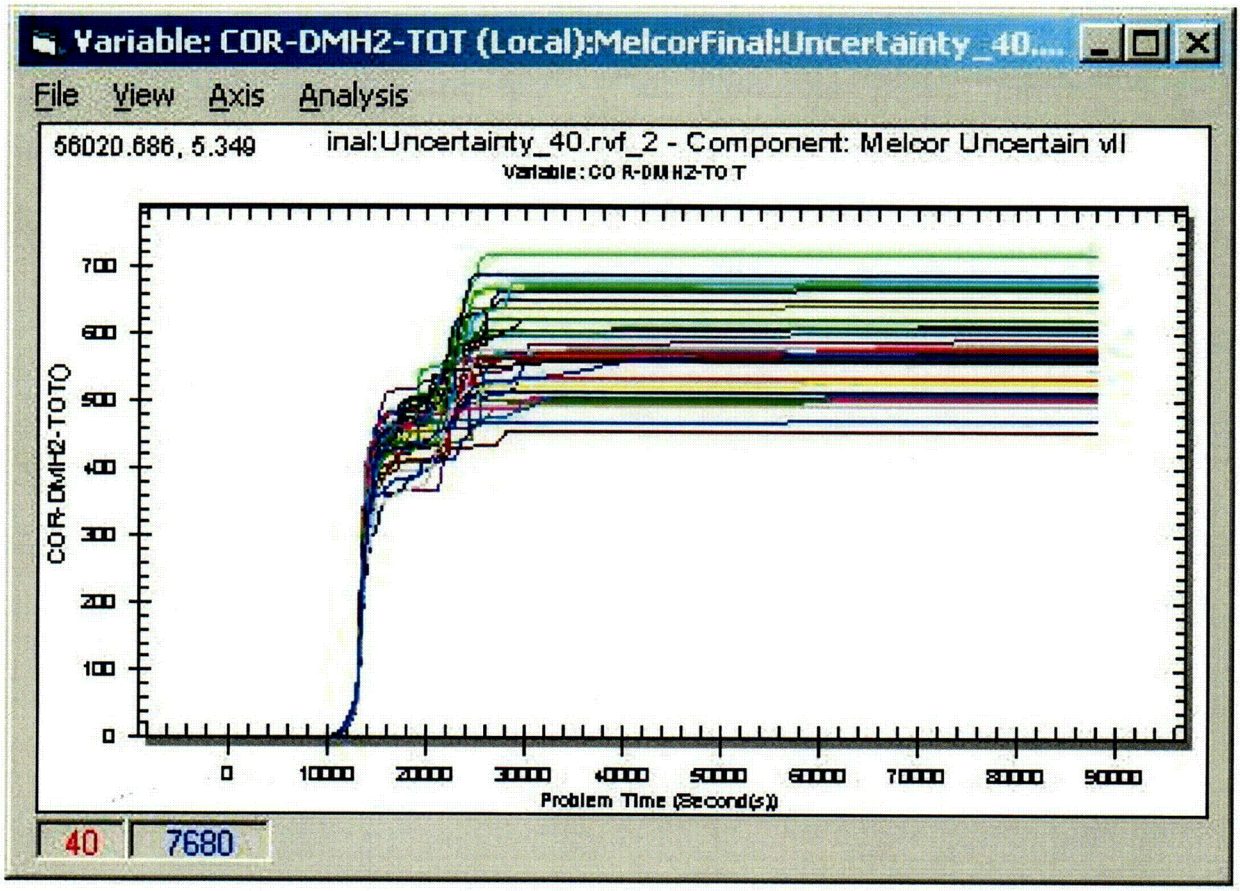

Figure 5-2. Illustration of plotting feature of DesktopPA. The plot shows in-vessel hydrogen production (kg) as a function of time (s). One curve is displayed for each of the 40 realizations.

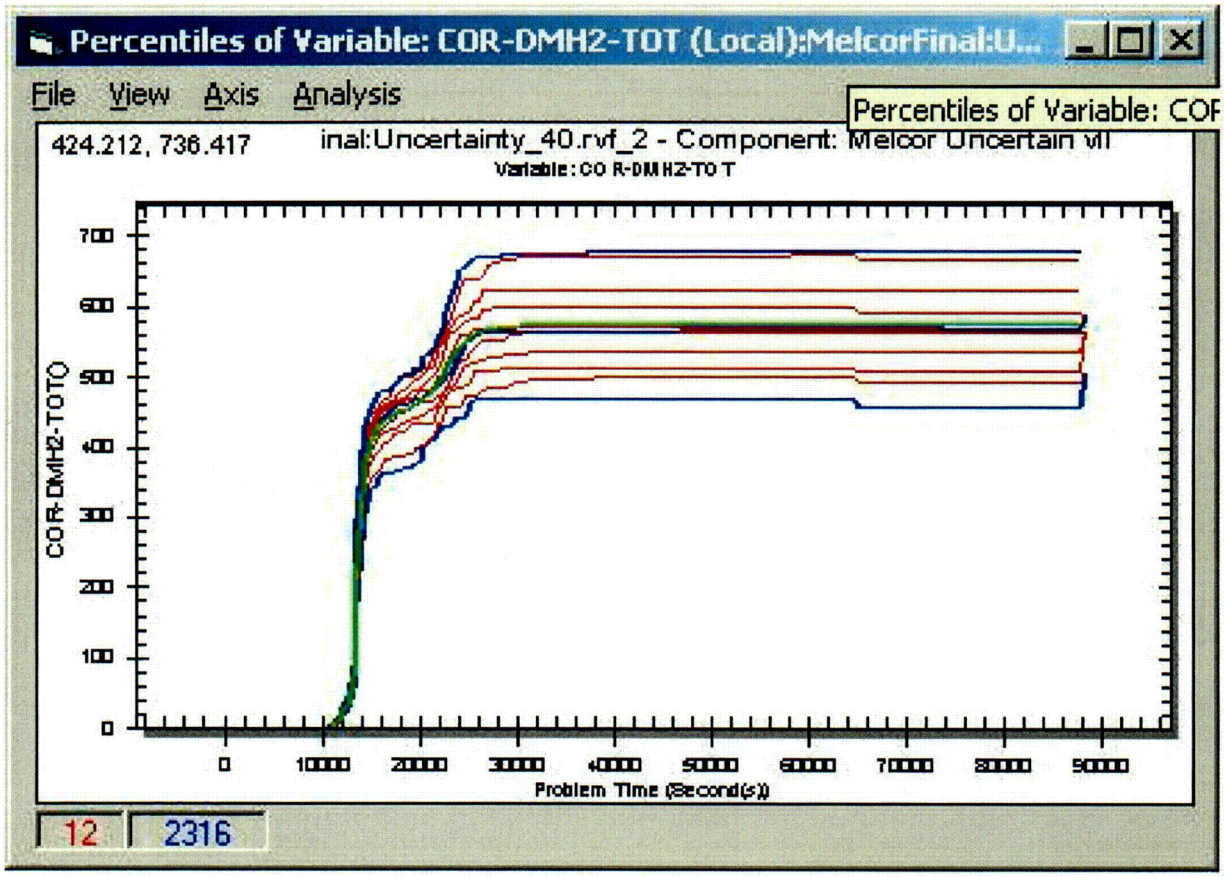

Figure 5-3. Illustration of the simple statistical analysis features in DesktopPA. The plot shows the 5, 10, 20, 30, 40, 50, 60, 70, 80, 90, and 95 percentiles of the in-vessel hydrogen production (kg) versus time (s). The 5^{th}, 50^{th}, and 95^{th} percentiles are dark blue. Other percentiles are red. It also shows the mean in light green.

6 Results of the MELCOR Analyses of Station Blackout in Sequoyah

6.1 Description of Short Term Station Blackout with Leaking Pump Seals

This sequence begins with the MELCOR model simulating full steady state reactor power when the calculation initiates at –500 sec. At time 0 sec, the station blackout condition is initiated, after which scram occurs and accident conditions develop. The analysis assumes that the steam generator secondary side remains pressurized while heat is rejected from the primary system by full loop natural circulation. The heat rejection to the steam generators during the time that water in the secondary side is sufficient to remove the decay heat from the core; however, after the steam generators dry out, the primary system pressurizes to the relief valve setpoints whereupon venting of steam from the primary system to the containment takes place. Eventually enough coolant is lost by relief valve venting and leaking RCS pump seals that the core becomes uncovered and severe damage, including cladding oxidation and core melting takes place. During this time hydrogen from cladding oxidation escapes with the steam venting through the cycling PORV relief valves as well as the leaking and degrading pump seals. Counter-current vapor phase circulation in the hot leg and steam generators transports significant heat to hot leg piping, surge line and steam generator tubes, and creep rupture failure of these components is modeled. Core relocation to the lower head eventually occurs, followed some time later by failure of the vessel head and ejection of core materials to the lower cavity region. The ex-vessel stage of the accident is characterized by core concrete interactions producing H_2, CO, CO_2 and steam. The analyses were terminated at 24 hours.

The short term station blackout sequence described considers that, with the loss of AC power, the RCS pump seals leak due to loss of fluid backpressure and cooling of the seals [9]. Leaks are modeled at each of the four reactor coolant pumps that allow the liquid RCS coolant to escape at the pump locations. Initially these leaks are sized such that at normal operating conditions the liquid leak rate is 21 gpm per pump. It is further assumed that as the RCS fluid temperature in the pumps approaches saturation conditions, the seal leaks worsen considerably. The MELCOR model enlarges the leak openings at this time to allow 250 gpm per pump (based on normal operating conditions) to escape from the RCS.

6.2 Summary Results of the Analyses

The following sections present detailed results of selected calculation to illustrate the general nature of the accident signatures for the short term station blackout analyses in this study. As summarized in Table 6-2, 18 of the calculations predicted a failure of the hot leg nozzle, and 22 calculations predicted failure of the lower vessel head, by creep rupture in all cases. Failure of either the hot leg nozzle or the lower vessel head occurred between 6 and 7.5 hrs into the accident sequence. In all of the analyses, both the lower head failure and hot leg nozzle failure processes were in competition for "first to cause failure." In the cases where hot leg nozzle failure was predicted, a subsequent lower head failure followed some time later by high temperature yielding of the head. Summary statistics on the timing to failure of either hot leg nozzle or lower head are provided in Table 6-1.

Table 6-1 Summary Statistics on Timing to Nozzle or Head Failure.

	Observations	Frequency	Mean	Standard Deviation
Time to Hot Leg Nozzle Failure	18	45%	7.5 h	0.7 h
Time to Lower Head Failure	22	55%	6.2 h	0.6 h

Figure 6-2 displays the predicted in-vessel hydrogen produced for all 40 calculations in the sensitivity study, showing the full range of the uncertainty results for in-vessel hydrogen produced by the LHS parameter variations. The LHS parameter variations used in each of the calculations is summarized in Table 6-2.

Hydrogen produced *in-vessel* can be distinguished from the hydrogen that is subsequently produced *ex-vessel* when vessel lower head failure transfers core materials to the reactor cavity and core-concrete interactions initiate. The *in-vessel* hydrogen may be further classified as being *early in-vessel* and *late in-vessel* hydrogen. *Early* in-vessel hydrogen, in this document refers to hydrogen produced prior to any failure of the RCS pressure boundary (lower head or hot leg nozzle), and *late in-vessel* refers to hydrogen produced in-vessel after RCS failure and depressurization. Subsequent sections will refer to this distinction in an exploration of the phenomenological explanation of hydrogen sensitivity for the varied parameters, and as will be shown, differences exist with respect to parameter sensitivity for early and late in-vessel hydrogen.

Referring to Figure 6-2, there is clearly less total predicted uncertainty (or variation) in the quantity of early in-vessel hydrogen that has been produced by ~5 hrs, than for the late in-vessel hydrogen produced by ~8 hrs. In some cases, a calculation that produced low early in-vessel hydrogen, subsequently goes on to produce a large late in-vessel amount. The following sections examine several cases in detail to determine the phenomena operative in producing some of the observed variations in hydrogen production. Cases examined in detail are highlighted in Table 6-2 and identified by their hydrogen signature in Figure 6-3.

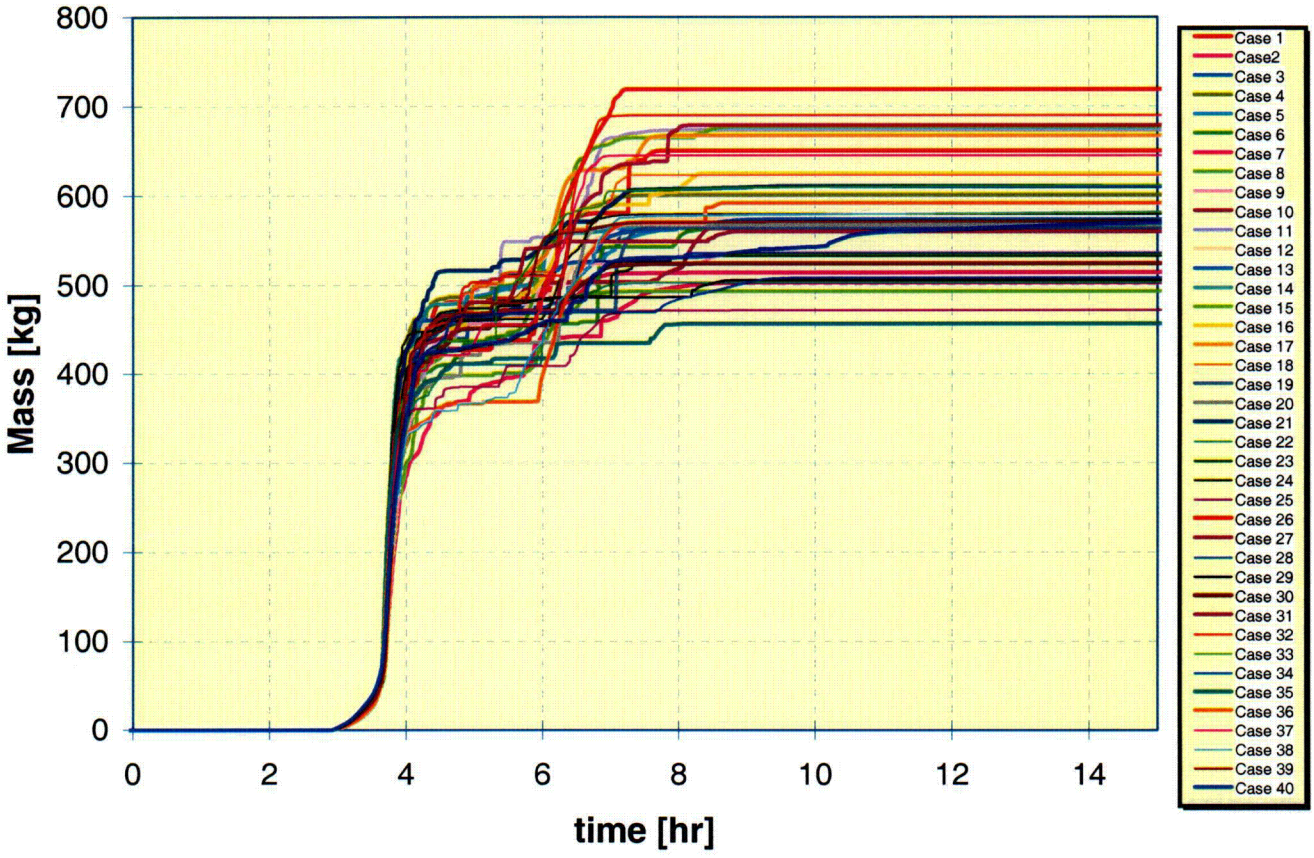

Figure 6-2 Summary of in-vessel hydrogen results for all cases in study.

Table 6-2 Summary of Parameter Selection for Each MELCOR Run and Resulting Total In-Vessel Hydrogen

Run Number	RCS Failure	Zr Melt Release SC11310	UO2 Collapse Temp SC11320	Radiation Factor FCELR COR00003	Zr Freezing Coefficient COR00005	Secondary UO2 Transport COR00007	Lower Head Initial HX COR00009	Falling Debris HX COR00012	Core Region PD CORijj04	Lower Plenum Region PD CORijj04	Debris Porosity PORDP CORZjj01	CAV000 Multipliers	Oxidation Model	In-Vessel Hydrogen
		[K]	[K]	[-]	[W/m^{2}K]	[-]	[W/m^{2}K]	[W/m^{2}K]	[-]	[-]	[-]	[-]		[kg]
1	Hot Leg 3	2415	2620	0.1300	11200	0.312	150	228	0.01700	0.02340	0.366	43	Baker-Just	650
2	Lower Head	2233	2610	0.1630	7580	0.012	150	183	0.01230	0.03220	0.208	12	Urbanic-Heidrick	514
3	Lower Head	2428	2580	0.0590	3540	0.327	150	127	0.00862	0.05370	0.409	42	Prater-Courtright	567
4	Lower Head	2473	2550	0.1180	8270	0.079	150	164	0.01090	0.03770	0.445	35	Baker-Just	601
5	Lower Head	2495	2590	0.1060	10700	0.238	150	150	0.01400	0.04240	0.437	19	Urbanic-Heidrick	563
6	Lower Head	2361	2610	0.0622	7940	0.198	150	133	0.01630	0.05050	0.388	65	Urbanic-Heidrick	564
7	Hot Leg 3	2405	2450	0.1400	3060	0.268	150	341	0.00561	0.01280	0.382	60	Prater-Courtright	503
8	Lower Head	2324	2670	0.0747	3670	0.293	150	259	0.00447	0.01950	0.488	75	Urbanic-Heidrick	493
9	Hot Leg 3	2336	2640	0.1220	6710	0.185	150	234	0.02310	0.02260	0.451	64	Urbanic-Heidrick	536
10	Hot Leg 3	2476	2710	0.1320	5960	0.096	150	292	0.00928	0.01630	0.399	28	Lemmon	563
11	Lower Head	2339	2600	0.0519	9790	0.032	150	191	0.00973	0.03040	0.349	68	Lemmon	673
12	Hot Leg 3	2467	2480	0.0270	5760	0.067	150	227	0.02080	0.02360	0.380	55	Urbanic-Heidrick	574
13	Lower Head	2401	2560	0.0900	2930	0.211	150	374	0.01560	0.01110	0.354	29	Baker-Just	574
14	Lower Head	2439	2710	0.1240	5200	0.216	150	149	0.02880	0.04300	0.241	50	Baker-Just	566
15	Hot Leg 3	2373	2650	0.0826	9450	0.279	150	214	0.00769	0.02570	0.432	8	Lemmon	676
16	Hot Leg 3	2438	2570	0.1010	15800	0.115	150	178	0.02000	0.03340	0.467	38	Prater-Courtright	624
17	Hot Leg 3	2432	2410	0.0650	7470	0.124	150	221	0.02360	0.02460	0.255	17	Urbanic-Heidrick	667
18	Lower Head	2399	2490	0.1750	2080	0.367	150	185	0.01900	0.03180	0.292	26	Prater-Courtright	622
19	Lower Head	2345	2570	0.0990	13100	0.171	150	314	0.01820	0.01450	0.330	83	Lemmon	564
20	Lower Head	2424	2530	0.1260	11000	0.107	150	157	0.00420	0.04000	0.269	40	Lemmon	568
21	Hot Leg 3	2462	2660	0.0700	10200	0.055	150	313	0.01790	0.01470	0.373	52	Baker-Just	611
22	Lower Head	2302	2550	0.1120	12000	0.182	150	253	0.01360	0.02020	0.458	5	Prater-Courtright	503
23	Hot Leg 3	2384	2590	0.1030	16300	0.223	150	282	0.00873	0.01710	0.396	13	Prater-Courtright	533
24	Lower Head	2418	2520	0.1080	6870	0.174	150	168	0.02750	0.03650	0.472	10	Baker-Just	579
25	Lower Head	2387	2520	0.0559	4620	0.128	150	173	0.00336	0.03500	0.405	26	Prater-Courtright	471
26	Lower Head	2382	2630	0.0933	4030	0.154	150	217	0.00730	0.02510	0.297	22	Baker-Just	718
27	Hot Leg 3	2391	2470	0.1480	12600	0.159	150	207	0.01140	0.02700	0.494	56	Lemmon	678

C20

Run Number	RCS Failure	Zr Melt Release SC11310	UO2 Collapse Temp SC11320	Radiation Factor FCELR COR00003	Zr Freezing Coefficient COR00005	Secondary UO2 Transport COR00007	Lower Head Initial HX COR00009	Falling Debris HX COR00012	Core Region PD CORijj04	Lower Plenum Region PD CORijj04	Debris Porosity PORDP CORZjj01	CAV000 Multipliers	Oxidation Model	In-Vessel Hydrogen
		[K]	[K]	[-]	[W/m^{2}K]	[-]	[W/m^{2}K]	[W/m^{2}K]	[-]	[-]	[-]	[-]		[kg]
28	Hot Leg 3	2330	2480	0.0966	14000	0.234	150	240	0.02120	0.02180	0.311	33	Lemmon	536
29	Hot Leg 3	2519	2520	0.0841	6360	0.284	150	273	0.00504	0.01800	0.336	46	Lemmon	506
30	Lower Head	2395	2500	0.1390	4310	0.139	150	333	0.01460	0.01330	0.413	15	Prater-Courtright	524
31	Hot Leg 3	2363	2600	0.0797	5020	0.299	150	300	0.03340	0.01560	0.425	24	Lemmon	560
32	Lower Head	2446	2580	0.1540	8800	0.205	150	244	0.01060	0.02130	0.361	94	Prater-Courtright	690
33	Lower Head	2368	2510	0.0355	2420	0.249	150	203	0.01210	0.02780	0.324	36	Baker-Just	615
34	Hot Leg 3	2453	2660	0.0874	7110	0.195	150	388	0.00710	0.01040	0.479	15	Urbanic-Heidrick	508
35	Hot Leg 3	2379	2690	0.1170	5540	0.151	150	266	0.00608	0.01870	0.314	18	Baker-Just	456
36	Hot Leg 3	2351	2560	0.1450	9140	0.242	150	144	0.00232	0.04490	0.447	48	Baker-Just	591
37	Lower Head	2408	2540	0.0910	18100	0.383	150	353	0.01280	0.01210	0.283	73	Prater-Courtright	644
38	Lower Head	2412	2550	0.0738	15100	0.338	150	195	0.00298	0.02950	0.143	9	Urbanic-Heidrick	586
39	Lower Head	2427	2630	0.1140	12400	0.398	150	201	0.02540	0.02820	0.342	20	Urbanic-Heidrick	571
40	Hot Leg 3	2371	2620	0.0436	8700	0.257	150	176	0.01510	0.03410	0.421	31	Lemmon	573

Table 6-3 Summary of Failure Location/Time, RCS Pressure at Breach and Early/Late In-vessel Hydrogen

Run Number	RCS Failure Location	In-Vessel Hydrogen [kg]	Hot Leg Failure time [hr]	Head Failure Time [hr]	RCS Pressure at Breach MPa	H_2 at Breach [kg]	H_2 After Breach [kg]	Water Lost by RCS Breach [10^3 kg]
1	Hot Leg 3	650	6.1	7.3	6.3	484	166	173
2	Lower Head	514	0.0	5.6	2.4	395	119	165
3	Lower Head	567	0.0	6.1	4.1	479	88	175
4	Lower Head	601	0.0	5.7	6.8	503	98	179
5	Lower Head	563	0.0	6.8	1.6	503	60	1909
6	Lower Head	564	0.0	7.9	1.9	547	17	217
7	Hot Leg 3	503	6.2	6.9	6.2	435	68	174
8	Lower Head	493	0.0	5.5	4.6	401	92	173
9	Hot Leg 3	536	5.5	8.3	7.6	463	73	170
10	Hot Leg 3	563	5.5	7.6	7.9	475	88	169
11	Lower Head	673	0.0	6.7	4.4	611	62	210
12	Hot Leg 3	574	5.3	6.4	5.2	466	108	157
13	Lower Head	574	0.0	6.7	2.1	526	48	204
14	Lower Head	566	0.0	5.8	3	504	62	160
15	Hot Leg 3	676	5.5	8.2	8.6	441	235	176
16	Hot Leg 3	624	5.9	7.6	5.7	499	125	172
17	Hot Leg 3	667	5.7	6.9	3	511	156	167
18	Lower Head	622	0.0	6.6	4.1	568	54	195
19	Lower Head	564	0.0	7.1	3.4	473	91	206
20	Lower Head	568	0.0	6.4	3	497	71	192

Run Number	RCS Failure Location	In-Vessel Hydrogen [kg]	Hot Leg Failure time [hr]	Head Failure Time [hr]	RCS Pressure at Breach MPa	H_2 at Breach [kg]	H_2 After Breach [kg]	Water Lost by RCS Breach [10^3 kg]
21	Hot Leg 3	611	5.4	6.4	5.8	528	83	162
22	Lower Head	503	0.0	6.0	6.3	411	92	1752
23	Hot Leg 3	533	6.2	7.0	4.9	485	48	180
24	Lower Head	579	0.0	6.0	2.5	467	112	154
25	Lower Head	471	0.0	6.4	4.9	413	58	187
26	Lower Head	718	0.0	5.8	2.6	443	275	165
27	Hot Leg 3	678	6.2	7.8	3.9	476	202	176
28	Hot Leg 3	536	6.6	7.9	6.6	527	9	201
29	Hot Leg 3	506	5.7	8.2	8.9	477	29	179
30	Lower Head	524	0.0	6.1	5.2	454	70	174
31	Hot Leg 3	560	5.5	8.4	4.5	484	76	167
32	Lower Head	690	0.0	6.3	1.8	518	172	171
33	Lower Head	615	0.0	5.4	6.2	500	115	155
34	Hot Leg 3	508	5.6	7.7	6.5	469	39	183
35	Hot Leg 3	456	6.2	7.6	10	422	34	187
36	Hot Leg 3	591	6.0	8.4	7.2	369	222	181
37	Lower Head	644	0.0	5.9	6	455	189	163
38	Lower Head	586	0.0	5.5	7.9	382	204	167
39	Lower Head	571	0.0	5.8	3.4	490	81	185
40	Hot Leg 3	573	5.8	6.6	4	448	125	164

6.3 Characteristic Signatures Observed in Calculations

In the 40 calculations portrayed in Figure 6-2, four basic signatures can be identified based on whether RCS failure was by hot leg nozzle or lower vessel head creep rupture, and whether the final in-vessel hydrogen was relatively high or low in the range of results. Specific calculations representative of these possibilities are summarized in Figure 6-3. Subsequent sections will present details on the accident progression for these calculations in order to identify phenomena operative in producing these signatures. As seen in the following figure, larger variation is observed in the final in-vessel hydrogen than in the hydrogen produced early prior to failure and depressurization of the primary system. Clearly, the particular failure mode (head or nozzle) is not a determining factor in whether the final in-vessel hydrogen will be high or low relative to the total range. The cases selected for closer examination include both nozzle failure and lower head failure, both with high and low hydrogen. Examination of lower head failure Cases 25 and 26 is presented first. Subsequent sections will examine in detail each of the cases identified in Figure 6-3.

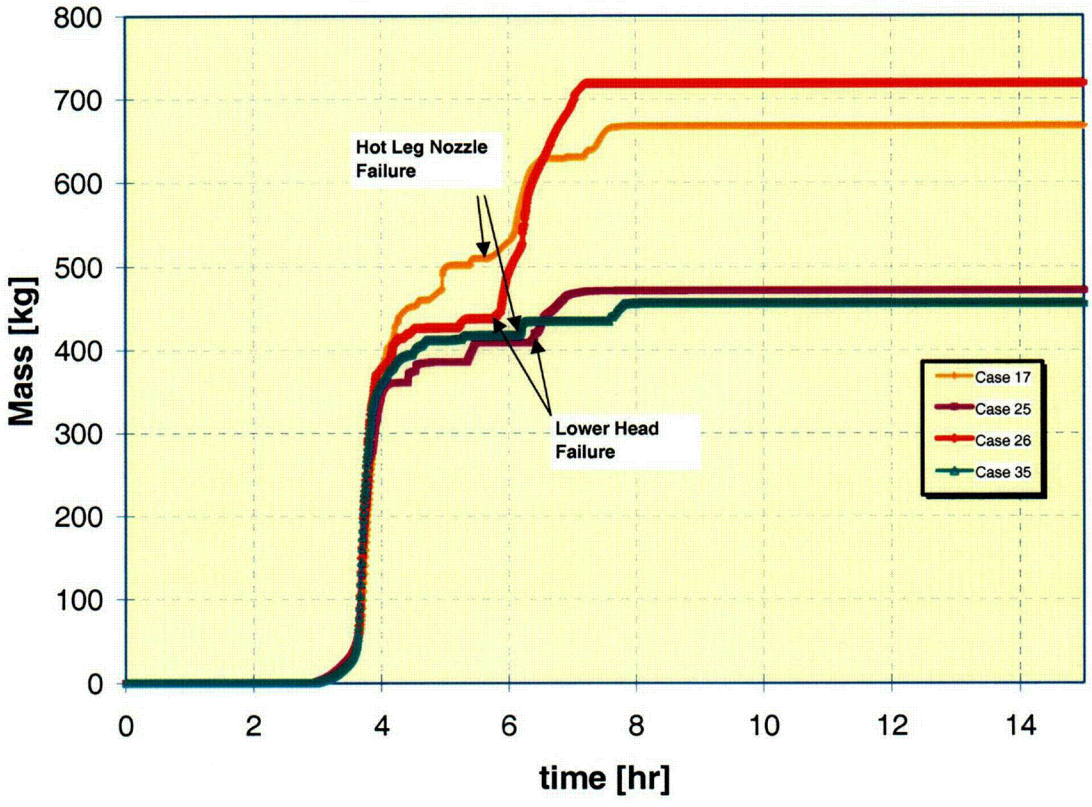

Figure 6-3 In-vessel hydrogen produced in high and low bounding calculations for both hot leg nozzle and lower head failures.

C22

6.3.1 Cases with Lower Head Failure

6.3.1.1 Case 26: Lower Head Failure with High In-Vessel Hydrogen Production

Presented in the following section are the results of MELCOR Case 26, a calculation which produced a large amount of hydrogen in comparison to other calculations, and which also resulted in failure of the lower head prior to any other failure of the reactor coolant system. As the accident initiates, the reactor power is scrammed, and owing to SBO-induced loss of cooling and backpressure to the main coolant pumps, leakage of RCS water via the pump seals begins, as shown in Figure 6-4. Initially, only liquid water escapes through the pump seal leaks, but after about 2 hrs, the coolant in the pumps becomes saturated and the seal leaks are presumed to worsen due to increasing temperatures. After this, mostly steam escapes via the seal leakage until accumulators inject liquid water into the loops at ~4.8 hrs.

The first four hours of the accident progression, for all cases examined, are quite similar, as shown in the subsequent four figures. The water level in the steam generator and the corresponding pressure of the primary system are shown in Figure 6-5 and Figure 6-6. The steam generator water level falls steadily as heat is removed from the primary system by boiling in the steam generator. At the point of steam generator dry out (~1.2 hours), having lost heat rejection capability to the steam generators, the system pressure is observed to rise rapidly (Figure 6-6), reaching the ~16Mpa setpoint of the safety relief valves. The system pressure remains at the safety relief valve (SRV) setpoint until nearly 2 1/2 hours when, because of the decreasing water level in the core (Figure 6-7), the boiling rate in the core becomes insufficient (owing to low water level) to maintain system pressure at the SRV setpoint value, and the pressure again begins falling. While the system pressure falls, water contained in the pressurizer drains into the RCS, as the pressurizer attempts to maintain the system pressure. At about 3.5 hrs, the pressurizer becomes fully drained (Figure 6-8) and the system pressure subsequently decreases at a faster rate.

As seen in Figure 6-9, fuel temperatures in the reactor core begin to increase as the water level falls below the top of the core. Oxidation of cladding with steam initiates when peak cladding temperatures exceed 1000K, producing hydrogen (Figure 6-10). By the time the core water level falls to the 1/3 core height level, peak fuel temperatures are on the order of 1500K, whereupon the cladding oxidation rate increases rapidly, producing rapidly increasing peak fuel temperatures. Shortly after the oxidation transient begins, both fuel cladding melt relocation and fuel rod collapse occurs, somewhat slowing the heatup rate and the production of hydrogen (Figure 6-10). By ~4.5 hrs, *early* in-vessel hydrogen production has nearly ceased, owing mostly to the boiloff of virtually all water in the lower head (Figure 6-7), and remains this way until the accumulator water injects when the RCS fully depressurizes upon lower head failure.

Between 4 and 5 hrs into the damage progression, the core materials gradually relocate into the lower plenum, as shown in Figure 6-11. The lower head is predicted to fail by creep rupture nearly two hours after the first relocation of core materials in the lower plenum, and about 1.2 hrs after the lower head boils dry. Figure 6-12 shows the temperature response of the potential failure locations in the RCS, which, as discussed earlier, include hot leg nozzles, steam generator tubes, the surge line and the lower vessel head. In this figure, the inner surface temperature of the lower head is seen to reach

melting temperatures at the time that the lower head fails by creep rupture. Such high head temperatures could not have been sustained without failing the vessel if the RCS pressure had not been relatively low, a characteristic pressure signature associated with leaking pump seals. Indeed, creep rupture failures observed in these analyses occur generally when core materials falling into the water-filledlower plenum induce a transient pressurization of the RCS. Higher ambient RCS pressures would have led to greater creep damage at lower wall temperatures.

Figure 6-13 shows the temperature of fuel "corium" and the head wall temperature. A corium molten pool is seen to form at ~5.8 hrs in the roughly 20 minutes prior to head failure, as evidenced by the thermal arrest at ~2800K associated with the heat of fusion of the presumed corium mixture UO_2-ZrO_2. As discussed earlier, the heat transfer coefficient from the lower plenum debris to the head wall increases as the debris temperature increases because of thermal radiation and pool convection effects, hastening head failure at high debris temperatures.

After ~4.8 hrs, the RCS pressure has fallen below the accumulator injection pressure and accumulator water injection to the RCS begins, as shown in Figure 6-14. This water produces some minor re-pressurization as seen in Figure 6-6, but results neither in significant water injection into the core (Figure 6-7), nor in appreciable production of hydrogen (Figure 6-10). Instead, most of the accumulator water escapes through the leaking pump seals, as seen in Figure 6-4. The water drainage through the leaking pump seals is encouraged by the still-pressurized RCS. After failure of the vessel head at ~5.8 hrs, complete RCS depressurization and a larger accumulator injection occurs, draining the accumulators completely. Note that since the RCS is depressurized at this time that water loss through the leaking pump seals is greatly reduced (Figure 6-4). At this time, renewed hydrogen production *is* observed (Figure 6-10) as accumulator water rushes toward the debris-filled lower plenum and exits through the vessel breach (Figure 6-15). During this time period, virtually all of the unoxidized Zr metal resides in the lower head, as shown in Figure 6-16. In-vessel hydrogen production ceases as the unoxidized Zr content in the vessel eventually vanishes due to oxidation and relocation to the cavity (Figure 6-16).

Core materials begin draining from the head breach and into the reactor cavity at ~5.8 hrs, and continue to drain for about two hours, as shown earlier in Figure 6-11. Upon head failure, the last of the accumulator water makes its way to the reactor cavity by way of the lower head breach, and is quickly boiled away by the fuel debris accumulating in the cavity. Core-concrete interaction begins almost immediately, producing additional hydrogen generation as shown in Figure 6-18.

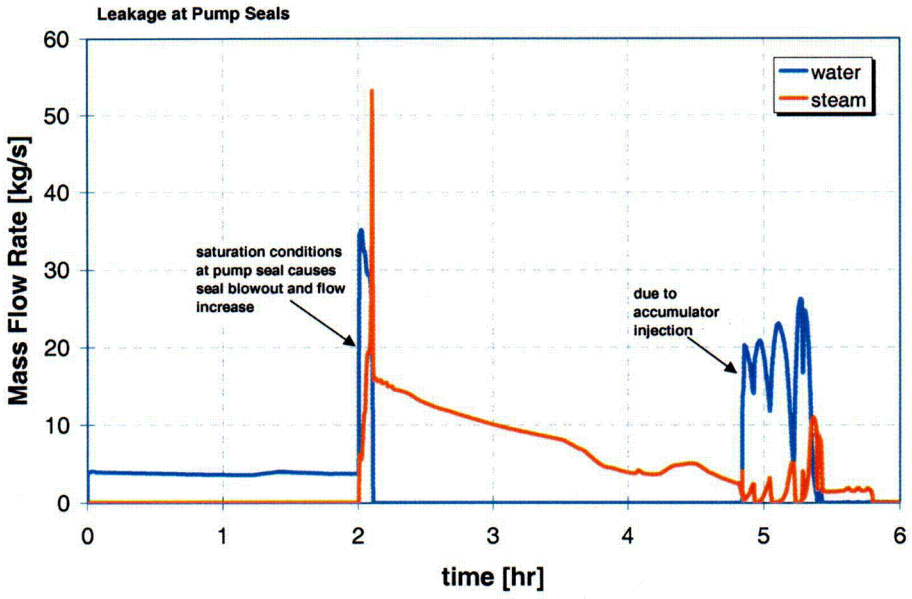

Figure 6-4 Case 26: Pump seal leakage of water and steam from four RCS pumps.

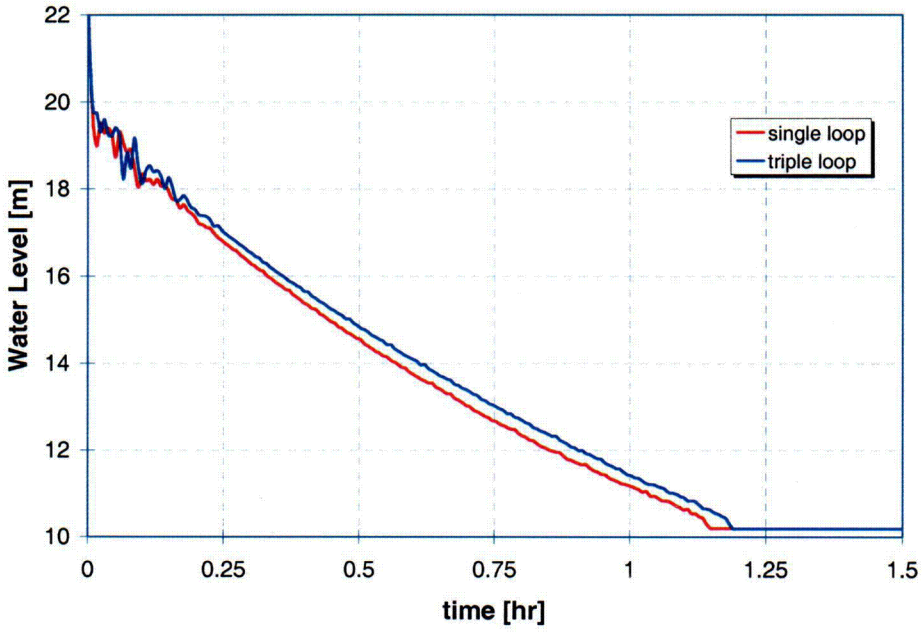

Figure 6-5 Case 26: Steam generator water level.

C23

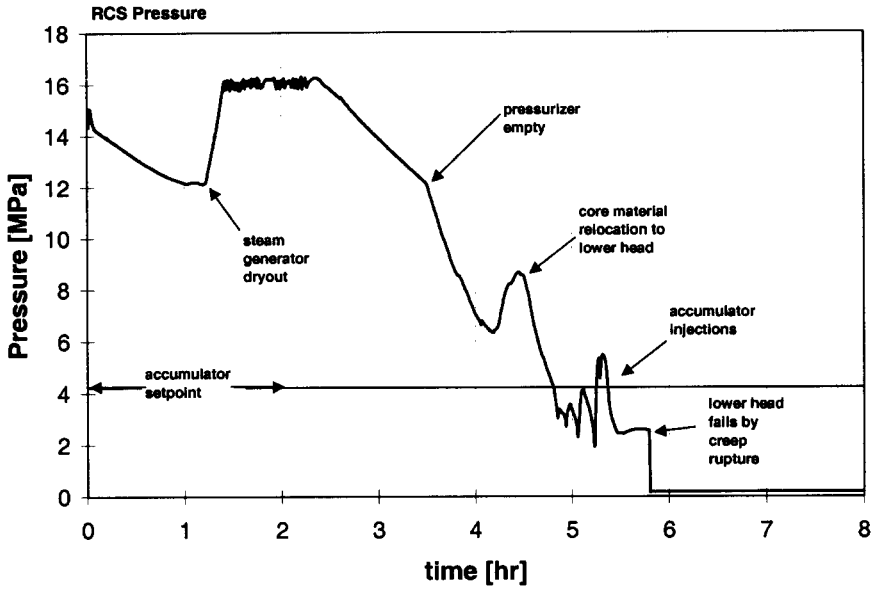

Figure 6-6 Case 26: Primary system pressure.

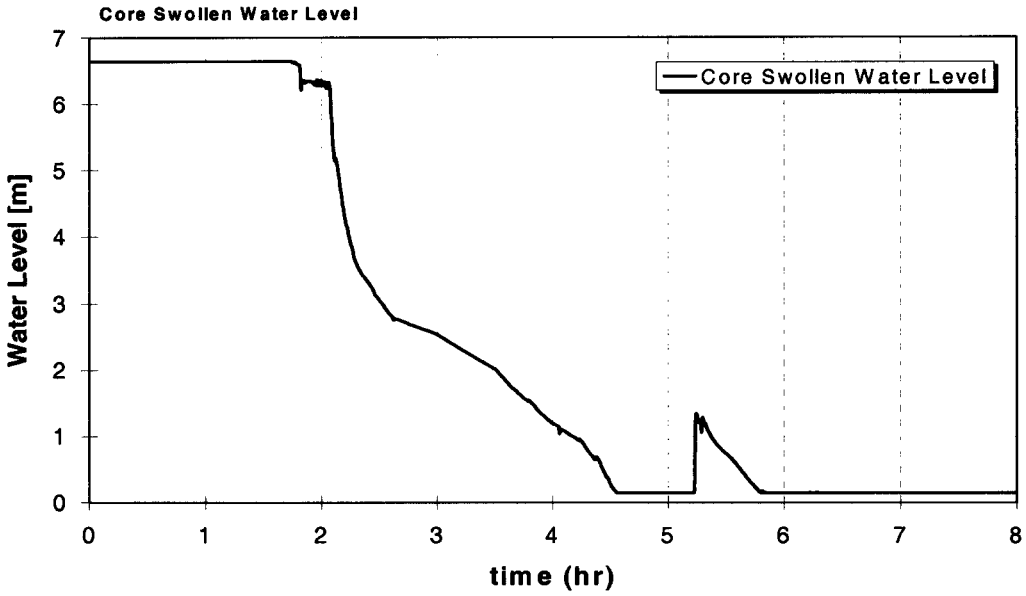

Figure 6-7 Case 26: Reactor core water level.

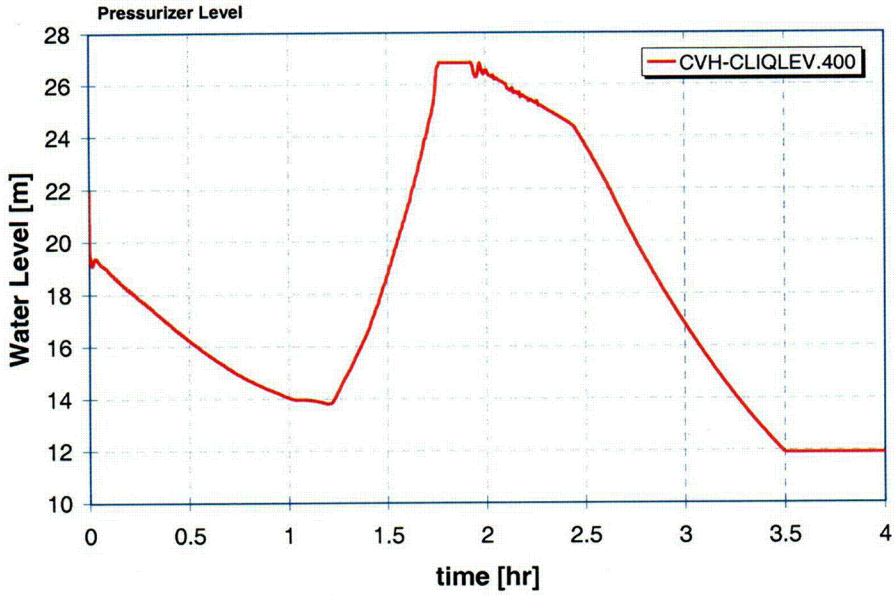

Figure 6-8 Case 26: Pressurizer water level.

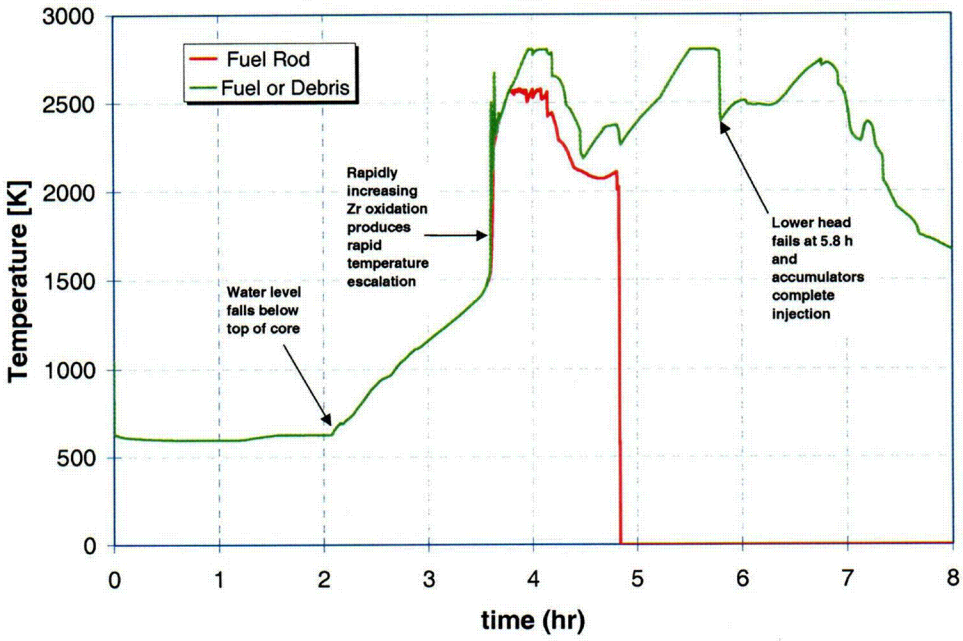

Figure 6-9 Case 26: Peak core region temperatures - intact fuel rods and fuel debris.

C24

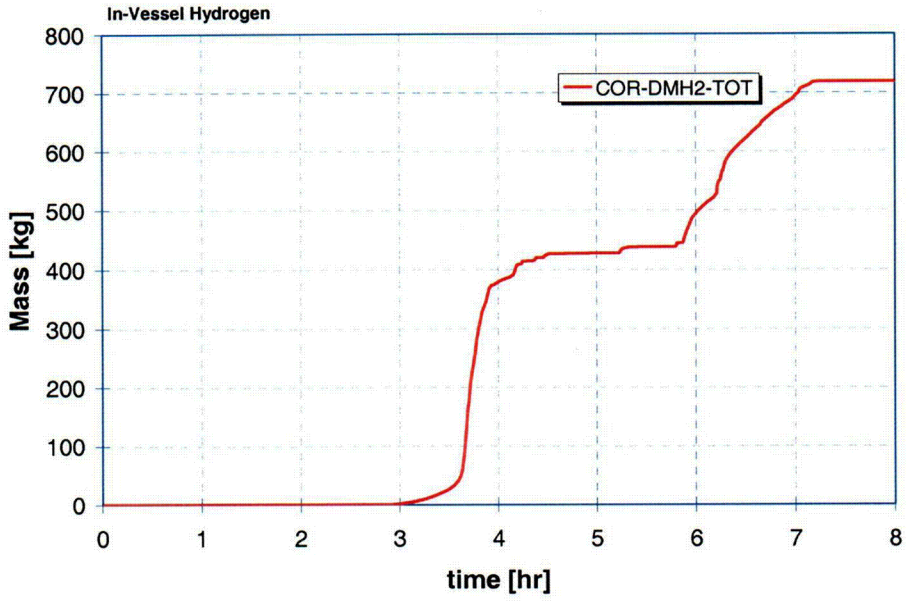

Figure 6-10 Case 26: In-vessel hydrogen production.

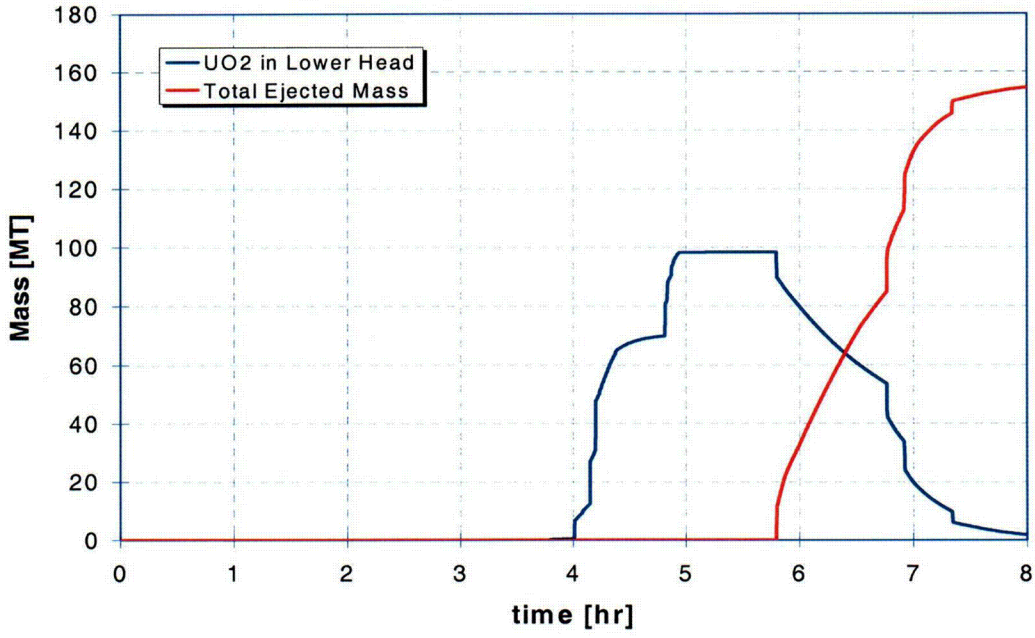

Figure 6-11 Case 26: Materials in lower head and in cavity.

C25

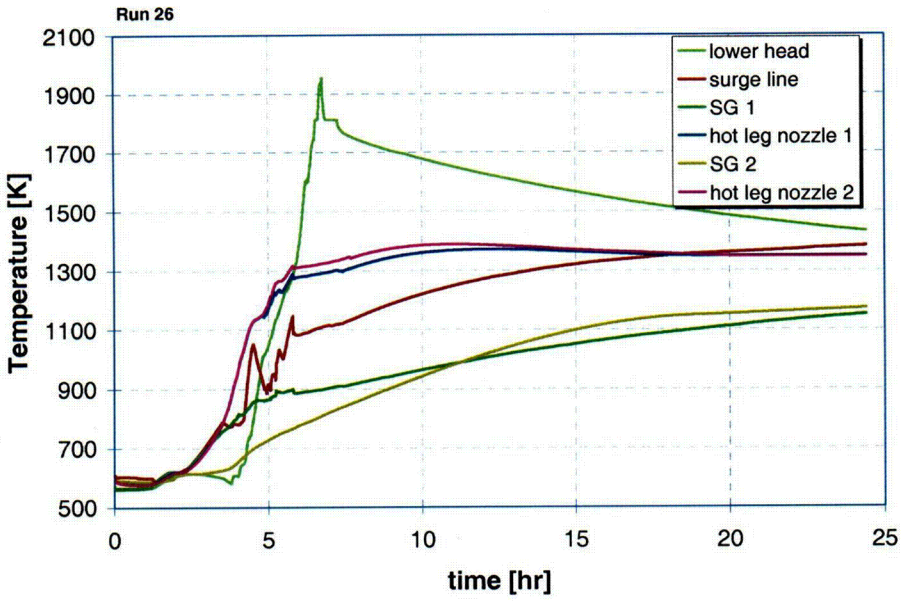

Figure 6-12 Case 26: Temperatures of potential RCS failure locations,

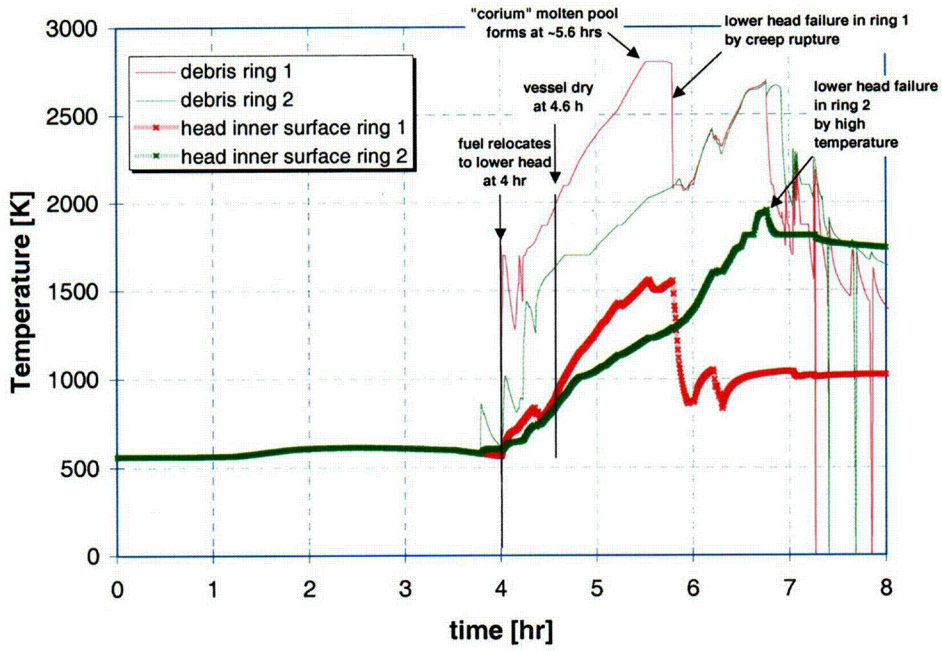

Figure 6-13 Case 26: Lower head fuel debris and head wall temperatures.

C26

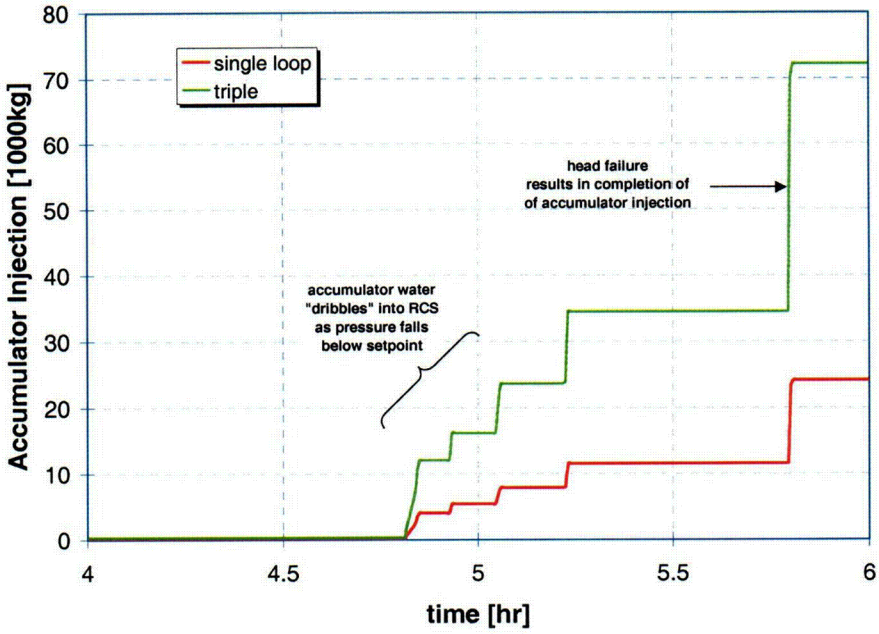

Figure 6-14 Case 26: Accumulator injection flow.

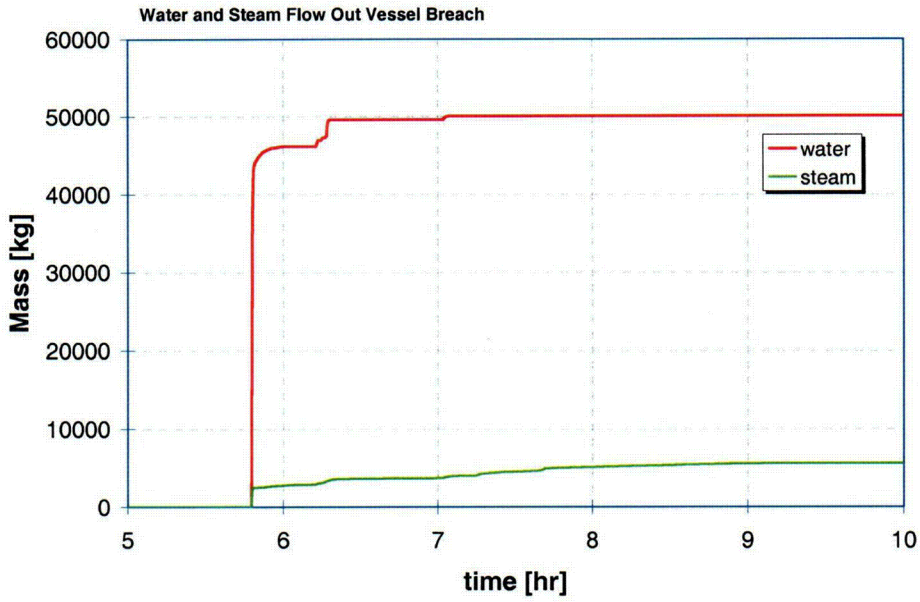

Figure 6-15 Water and steam escaping through breach in lower head.

C27

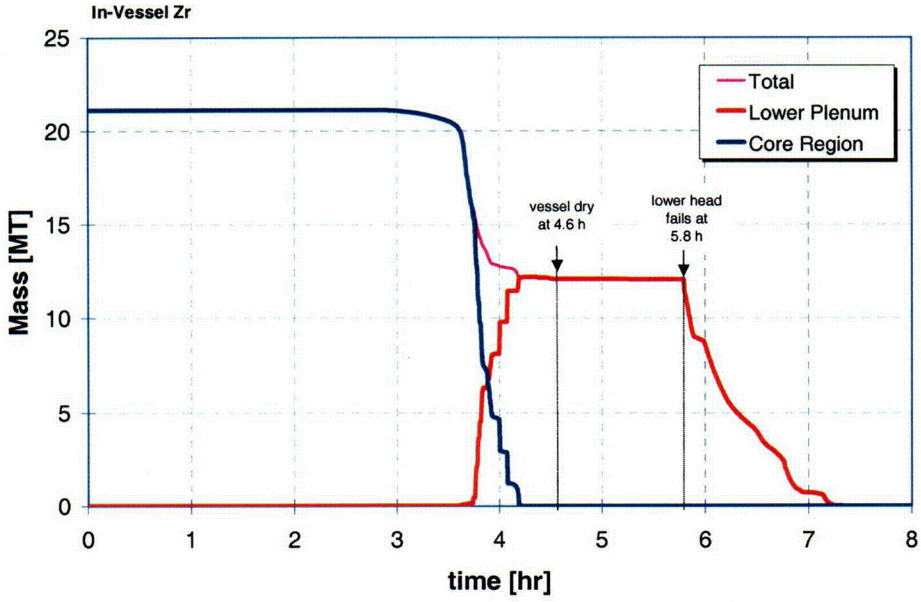

Figure 6-16 Case 26: Zr inventory in-vessel.

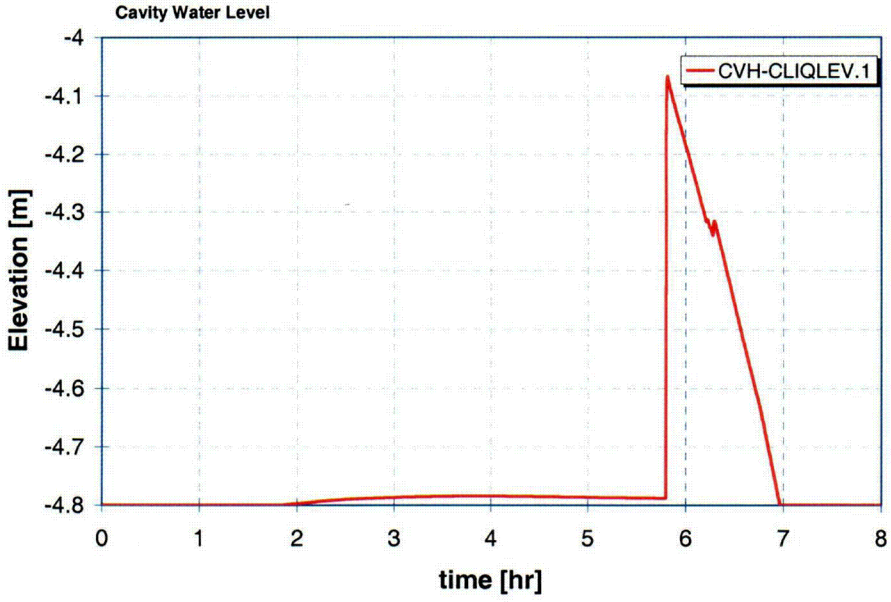

Figure 6-17 Case 26: Water level in the reactor cavity.

C28

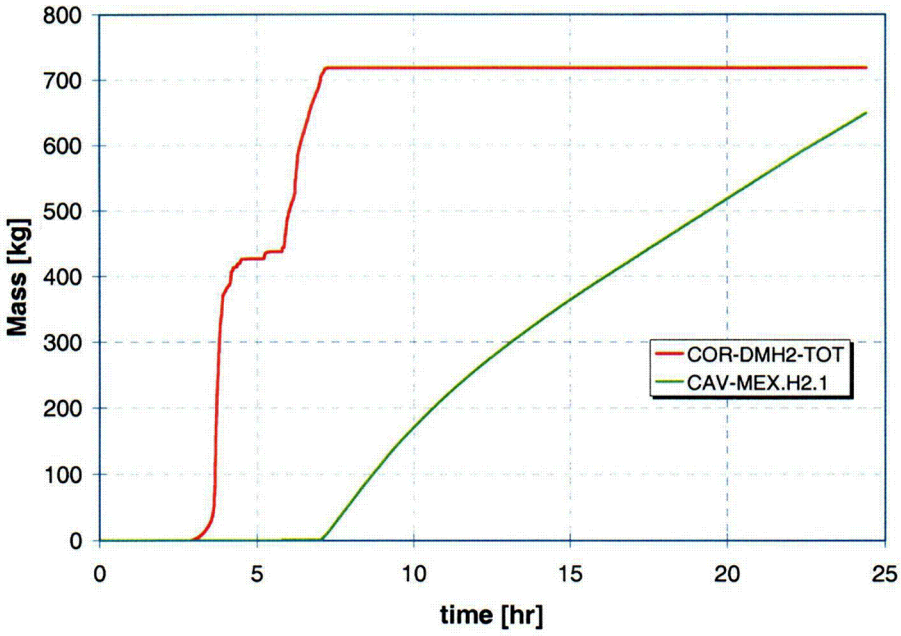

Figure 6-18 Case 26: In-vessel and ex-vessel hydrogen production.

C29

6.3.1.2 Case 25: Lower Head Failure with Low In-Vessel Hydrogen Production

In many respects, Case 25 proceeds very similarly to Case 26, producing similar amounts of "early" in-vessel hydrogen, but deviates significantly after lower head failure, producing comparatively little additional hydrogen following lower head failure. The following section illuminates the similarities and differences in the accident signature, and a subsequent section offers interpretation into the differences.

The first four hours of the accident in Case 25 are, for practical purposes, identical to that of Case 26, as seen in the pump seal leak rate and RCS pressures, Figure 6-19 and Figure 6-20. Differences in the RCS pressure signature between Case 25 and Case 26 are subtle to moderate after 4 hrs, the most notable being a higher pressurization due to accumulator injection at ~5.5 hrs and a delayed head failure in Case 25. The vessel water level signatures (Figure 6-21) are also quite similar. Examination of these figures suggests that the larger accumulator injection in Case 25 is responsible for the larger RCS pressure spike. Perhaps because greater vessel reflooding depth was attained in Case 25, somewhat cooler fuel/debris temperatures were experienced in this case relative to Case 26. Whereas, both cases resulted in about the same amount of fuel mass transferred to the lower plenum, the higher overall temperature of Case 26 produced creep rupture of the lower head sooner than in Case 25. Interestingly, although the lower head failed sooner in Case 26, the transfer of core materials to the reactor cavity was initially slower, as seen in Figure 6-23. The in-vessel hydrogen produced for Case 25 is shown in Figure 6-24, compared with that of Case 26. The cases appear different only in the late-time hydrogen produced after lower head failure. Figure 6-25 shows the ex-vessel hydrogen produced by core concrete interactions following lower head failure.

Figure 6-26 and Figure 6-27 may provide a partial explanation for the differences in late hydrogen observed in Cases 25 and 26. These figures show the hydrogen production rate plotted against the integrated steam flow out of the lower head rupture. Case 26 shows hydrogen produced as long as unoxidized Zr is present in the vessel (lower plenum), where the flow of steam out of the breach is maintained continuously during this period. Here, it is suggested that the steam leaving the vessel through the breach is oxidizing metallic Zr as it passes through. In contrast, Case 25 hydrogen production appears to be limited by the abbreviated period of steam flow out of the break associated with a more rapid boildown of the remaining accumulator water. It is also possible that flow restrictions arising from differences in debris geometry could be responsible for this observation.

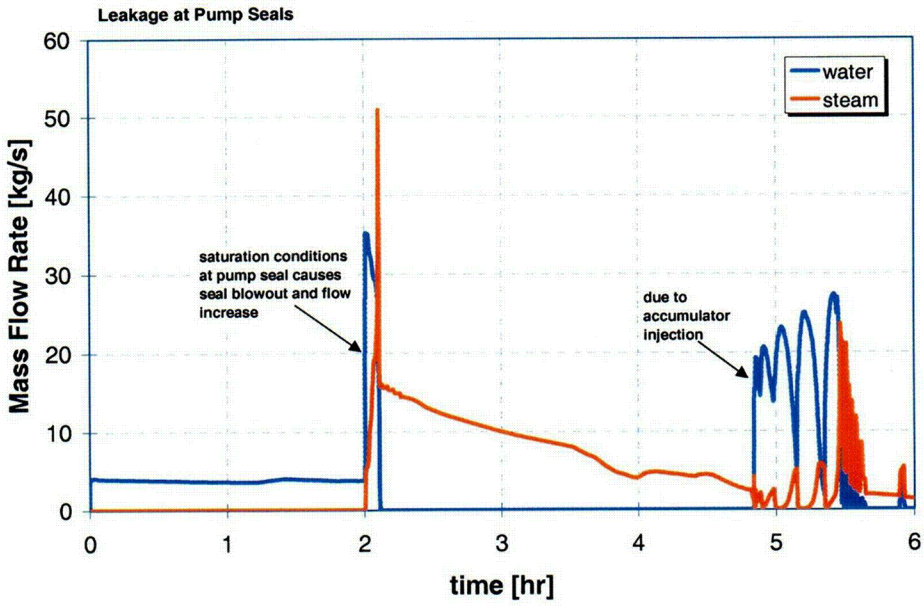

Figure 6-19 Case 25: Pump seal leakage for case with lower head failure and low hydrogen.

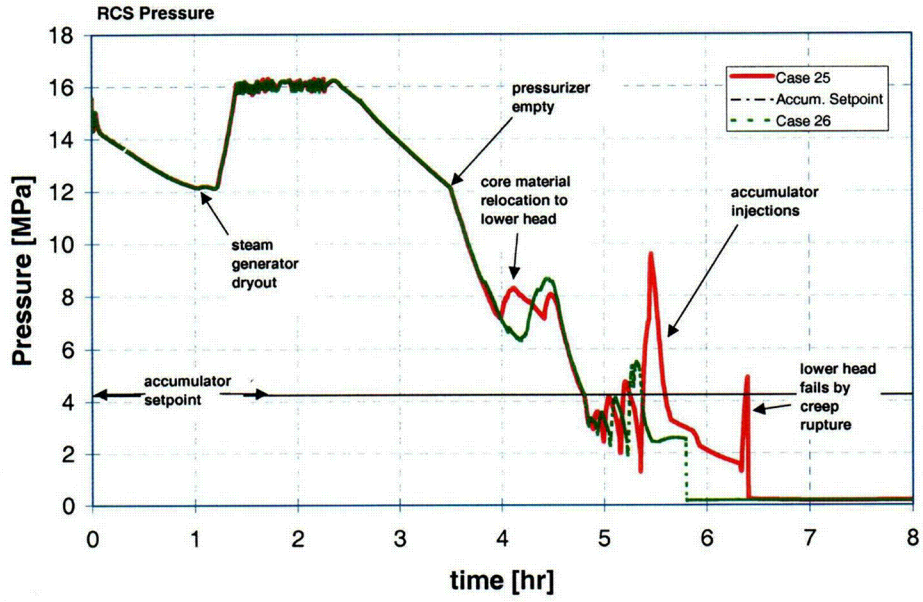

Figure 6-20 Case 25: RCS pressure for case with lower head failure and low hydrogen.

C30

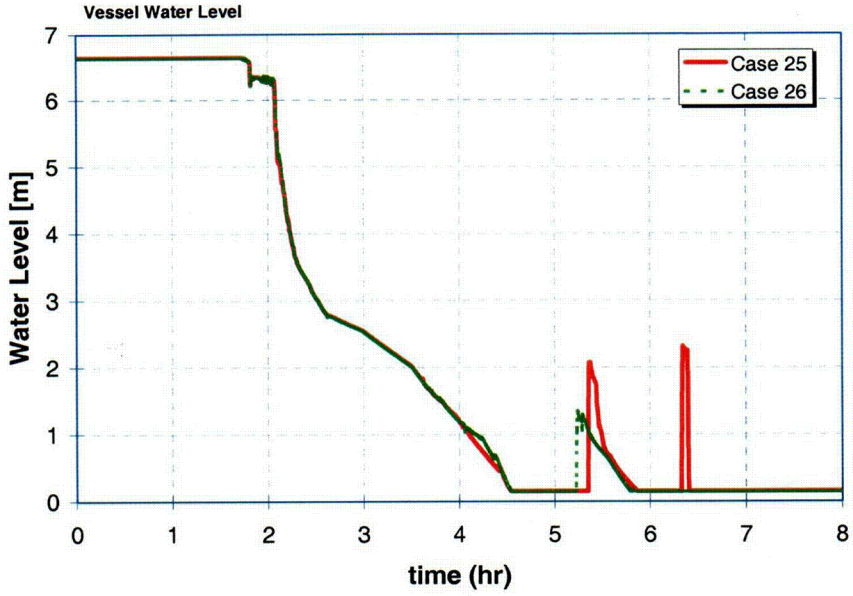

Figure 6-21 Case 25: Vessel water level for case with lower head failure and low hydrogen.

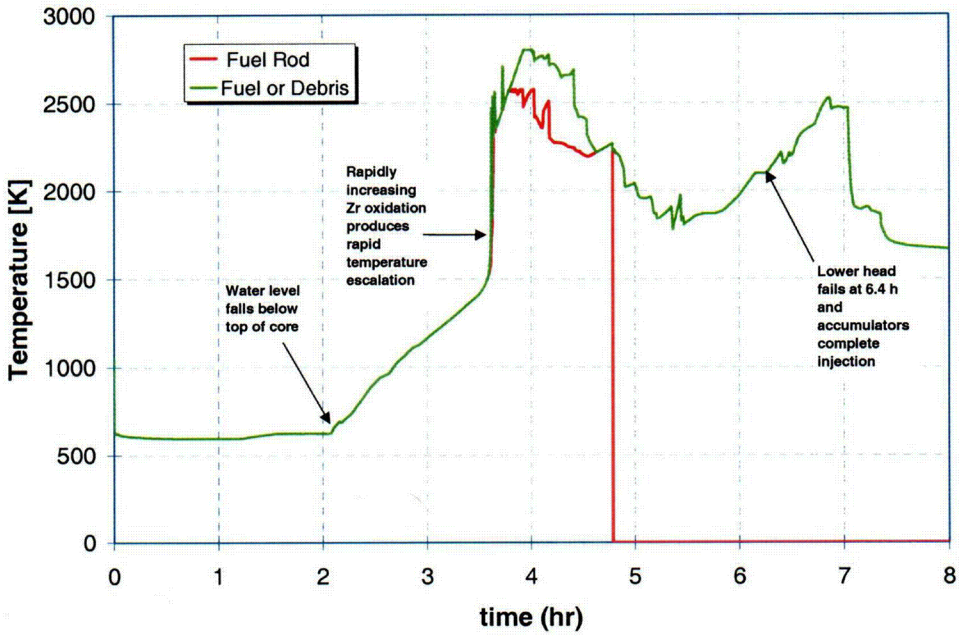

Figure 6-22 Case 25: Peak fuel rod and debris temperatures for case with lower head failure and low hydrogen.

C31

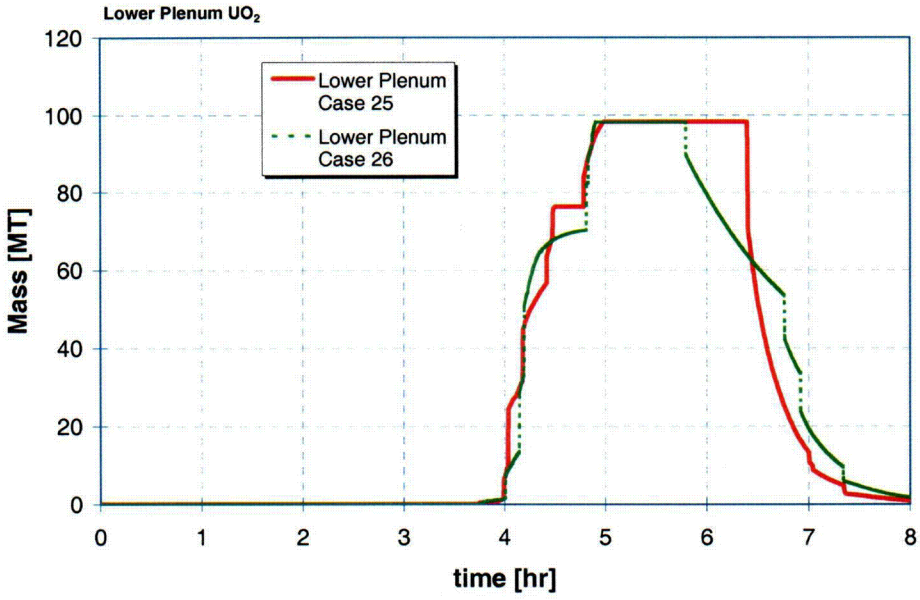

Figure 6-23 Relocation of fuel to lower plenum - comparison of Case 25 and Case 26.

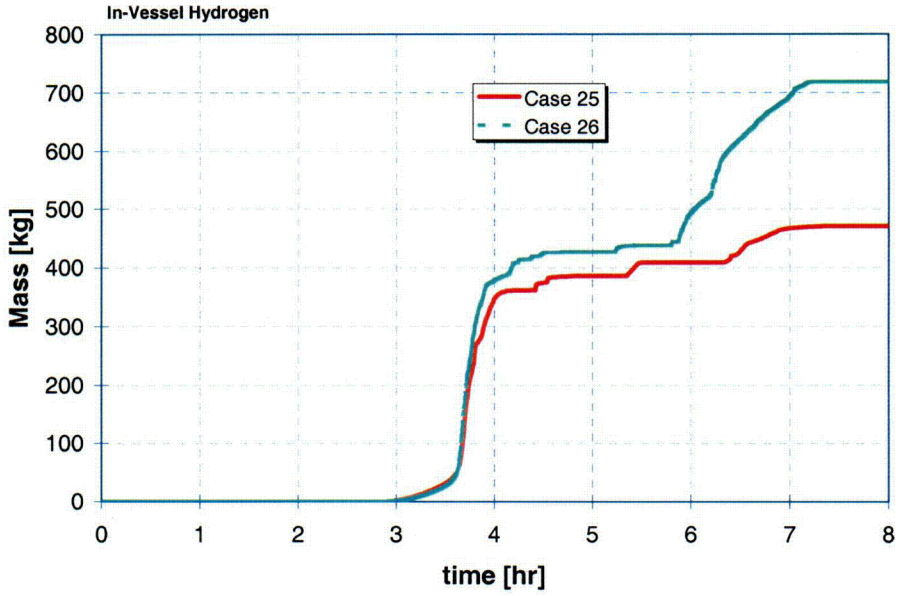

Figure 6-24 In-vessel hydrogen produced for Case 25 and Case 26.

C32

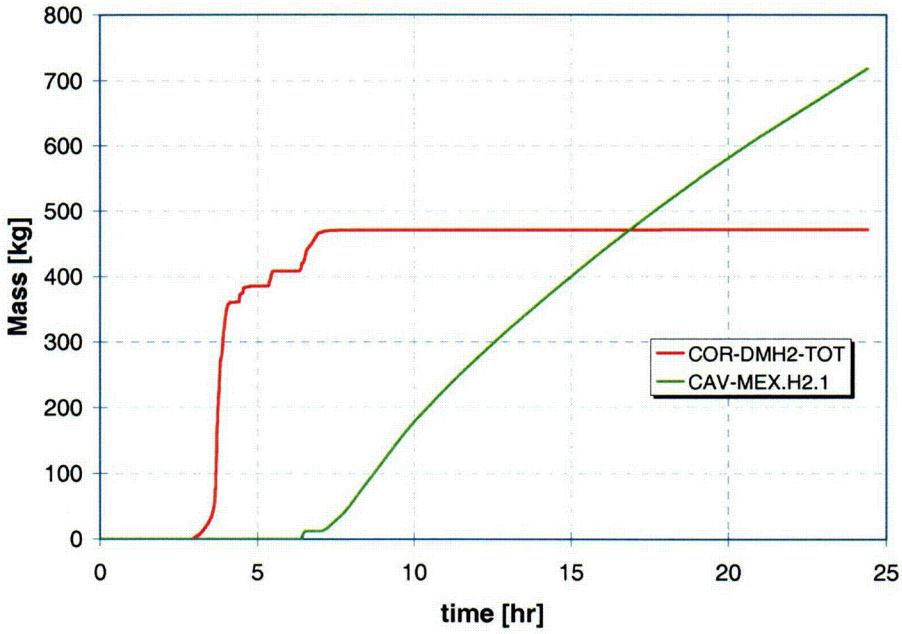

Figure 6-25 Case 25: Hydrogen produced for case with lower head failure and low hydrogen.

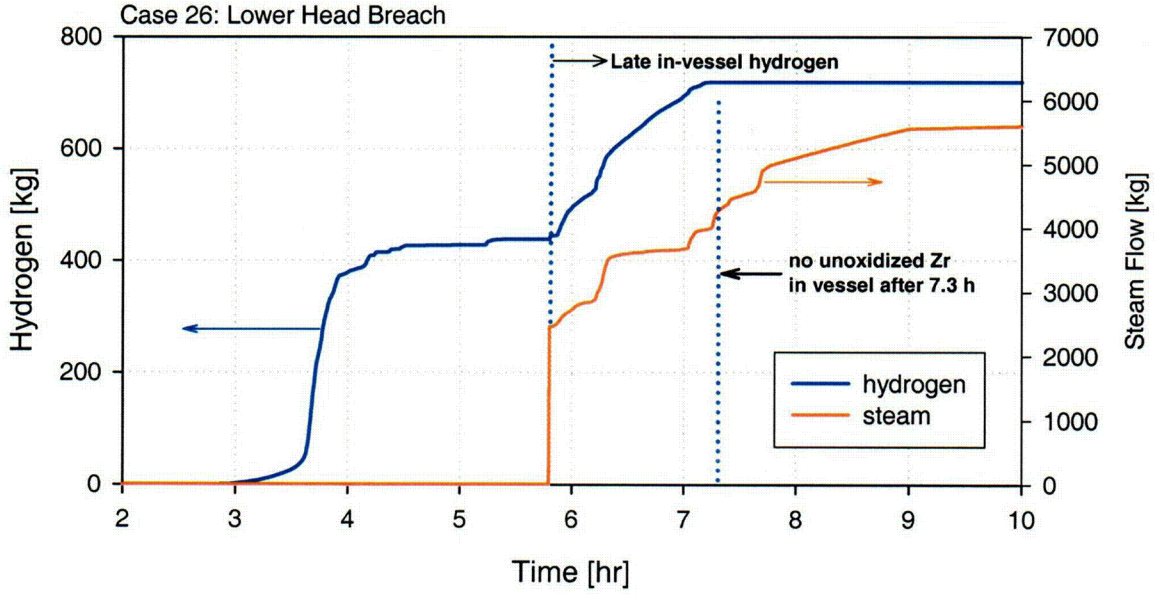

Figure 6-26 In-vessel hydrogen produced and break steam flow for Case 26 with high late-time in-vessel hydrogen.

C33

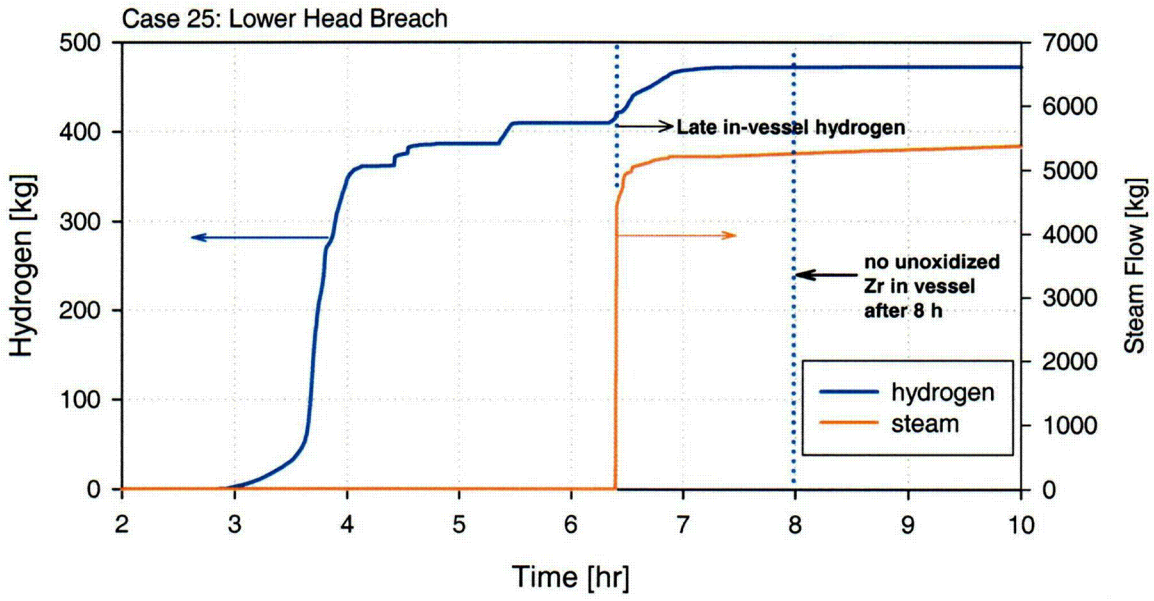

Figure 6-27 In-vessel hydrogen produced and break steam flow for Case 25 with low late-time in-vessel hydrogen.

C34

6.3.2 Cases with Hot Leg Nozzle Failure

The following two cases concern calculations resulting in hot leg nozzle failure produced by the RCS heating significantly assisted by the counter-current natural circulation patterns discussed earlier involving the vessel, the hot legs and the steam generators. Each of the two cases examined failed by hot leg nozzle creep rupture, one producing little hydrogen after the RCS rupture and one producing much.

6.3.2.1 Case 17: Hot Leg Nozzle Failure with High In-Vessel Hydrogen Production

The RCS pressure signature for Case 17 is shown in Figure 6-28, and appears remarkably similar to those for Cases 25 and 26, and indeed all those examined in this study. The first four hours of the damage progression is virtually identical in all cases. In both this case, and the next, temperatures in the hot leg were a little hotter earlier in time and led to failure of this component prior to lower head failure. As evident in Figure 6-29, upon failure of the hot leg nozzle and depressurization of the RCS, the subsequent accumulator injection produced a nearly complete reflooding of the reactor core. Figure 6-30 shows that this reflooding quenched fuel that was still in rod-like geometry, but did not quench fuel that had previously collapsed to form debris. In fact, the hottest debris regions continued to heat after reflooding. The in-vessel hydrogen produced in Case 17 is shown in Figure 6-32. As seen in this figure, hydrogen production continued even after the significant core region refloods, and examination of Figure 6-32, showing the unoxidized Zr inventory in the reactor vessel, indicates that the hydrogen produced after 5 hrs is not due to Zr oxidation. Instead, the additional hydrogen produced late in this sequence is due principally to oxidation of stainless steel in the lower plenum, as indicated in Figure 6-33.

The mass of fuel material relocated to the lower plenum is similar to previous cases, as seen in Figure 6-34. Even with the deep vessel reflooding after hot leg failure and accumulator injection, the lower plenum fuel material continued to heat (Figure 6-30), producing a thermally induced failure of the vessel head just before 7 hrs, whereupon fuel and other core materials was transferred to the reactor cavity region. The heating of critical pressure boundary components is shown in Figure 6-35, and as described earlier, failure conditions were attained in the hot leg nozzle prior to any other pressure boundary location. Temperatures in the inner head surface exceeding the melting point of the head material caused the lower head failure later in time. The ex-vessel hydrogen produced after 7 hrs by core concrete interactions is shown in Figure 6-36.

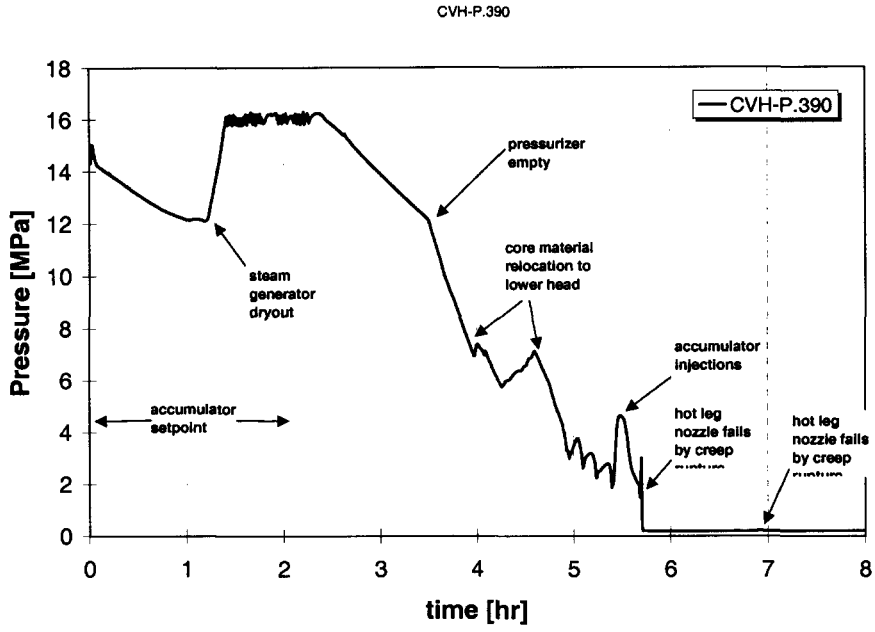

Figure 6-28 Case 17: Primary system pressure for case with hot leg failure and high hydrogen.

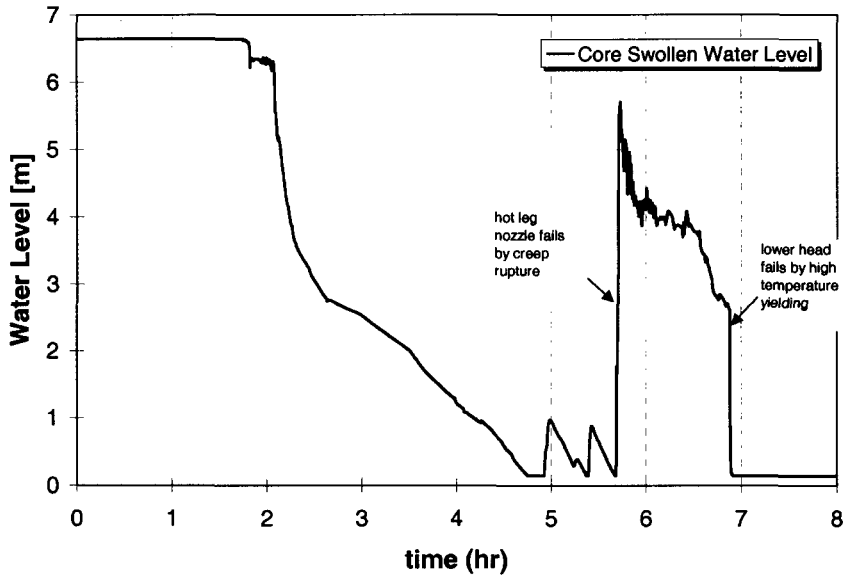

Figure 6-29 Case 17: Vessel water level for case with hot leg failure and high hydrogen.

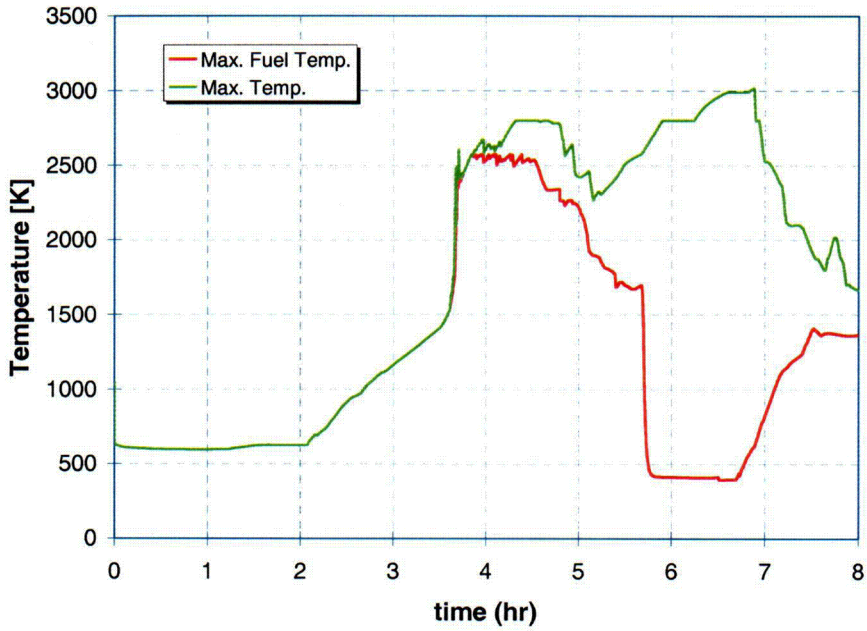

Figure 6-30 Case 17: Maximum fuel rod and fuel debris temperatures for case with hot leg failure and high hydrogen.

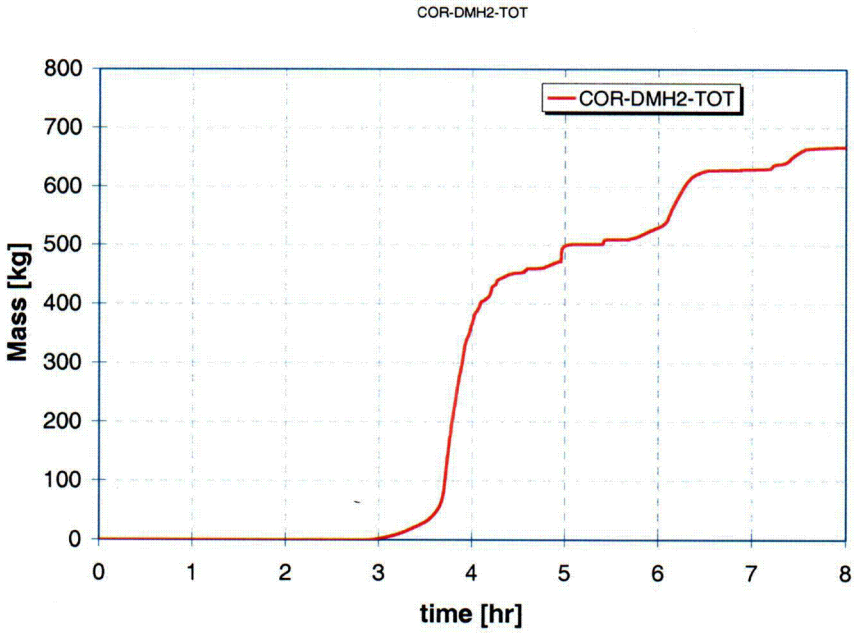

Figure 6-31 Case 17: In-vessel hydrogen for case with hot leg failure and high hydrogen.

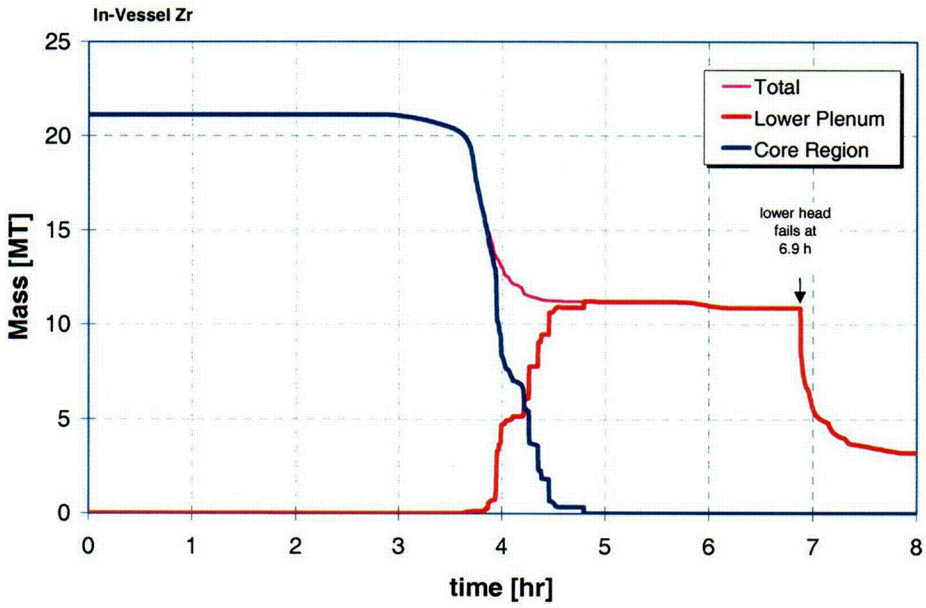

Figure 6-32 Case 17: Unoxidized in-vessel Zr for case with hot leg failure and high hydrogen.

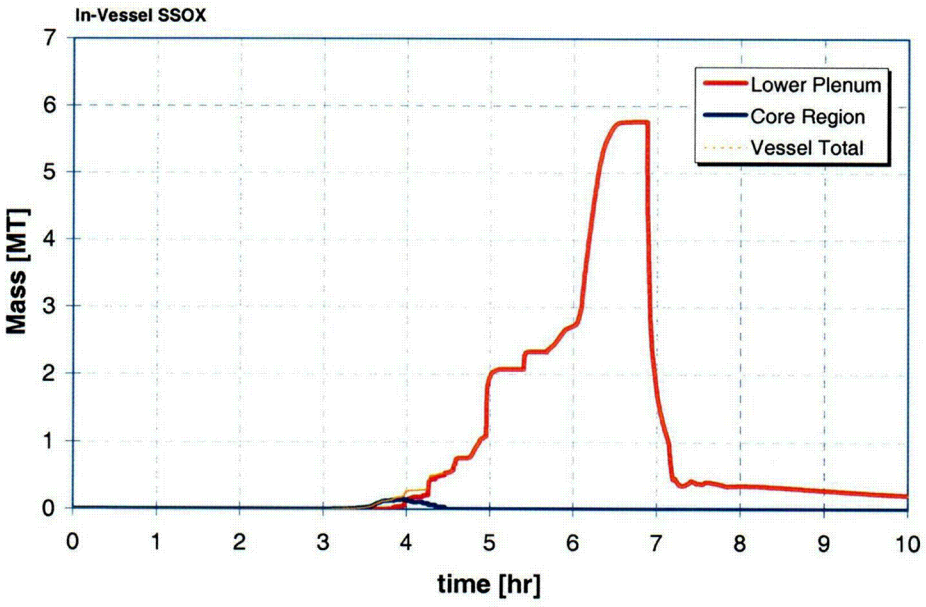

Figure 6-33 Case 17: Stainless steel oxide inventory in the reactor vessel.

C36

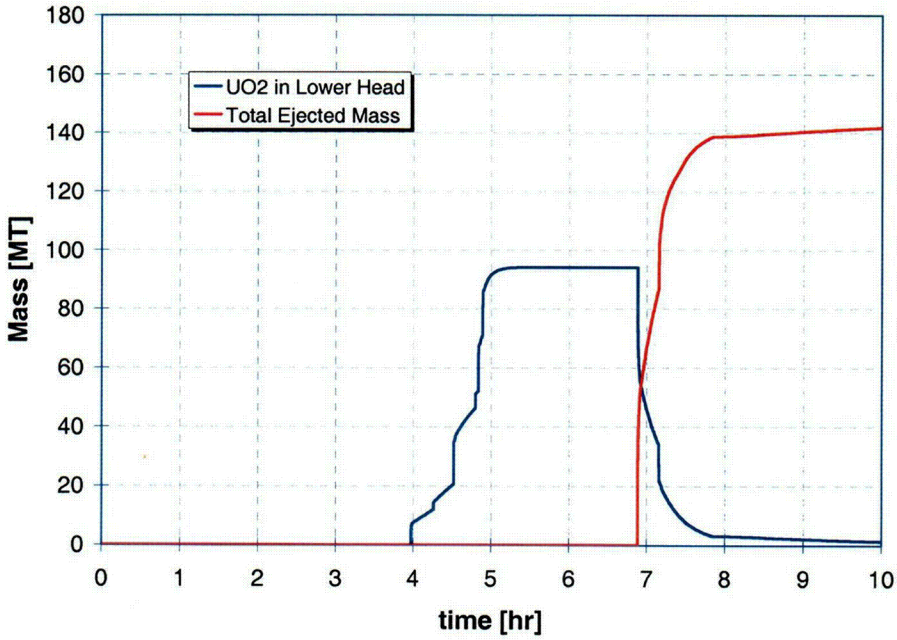

Figure 6-34 Case 17: Lower head debris and cavity debris for case with hot leg failure and high hydrogen.

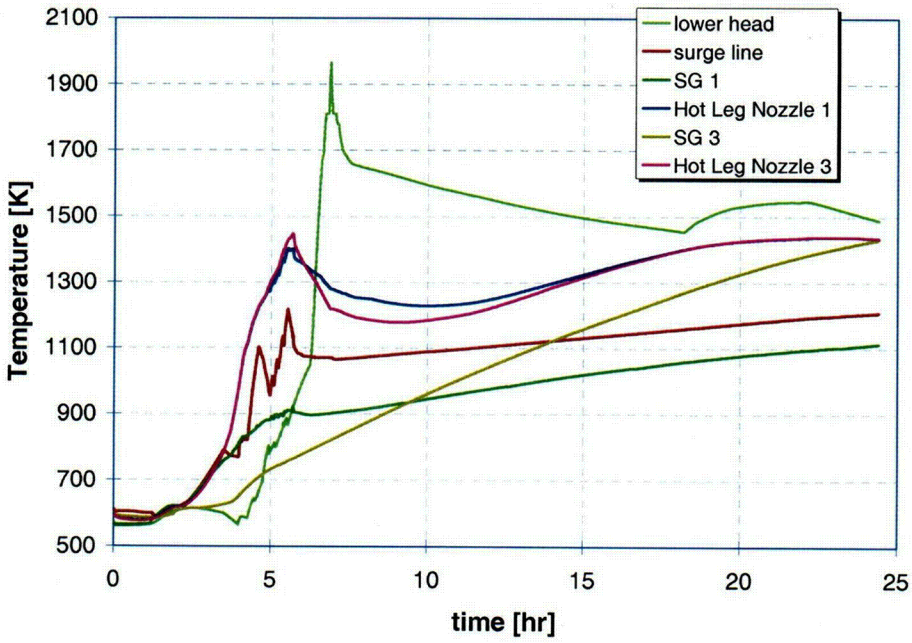

Figure 6-35 Case 17: Temperatures of potential RCS failure locations for case with hot leg failure and high hydrogen.

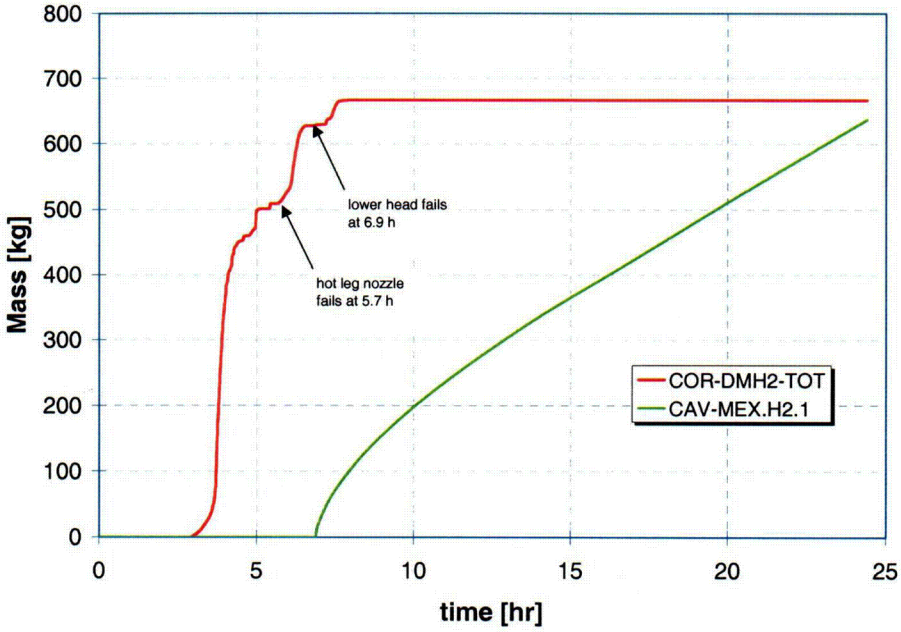

Figure 6-36 Case 17: In-vessel and ex-vessel hydrogen generation for case with hot leg failure and high hydrogen.

C38

6.3.2.2 Case 35: Hot Leg Nozzle Failure with Low In-Vessel Hydrogen Production

The final case to be examined is Case 35, involving again failure of the hot leg nozzle as the first failure of the RCS pressure boundary, but with a low late in-vessel hydrogen production. The now familiar pressure signature for this case is shown in Figure 6-37. Somewhat higher pressurization spikes are observed for this case for both core melt relocation to lower plenum and for accumulator reflood events. As with Case 17, this case involves a minor vessel reflood just after 5 hrs when the RCS pressure falls below the accumulator setpoint, and a more substantial reflood when the hot leg nozzle failure at shortly after 6 hrs results in complete depressurization of the RCS, as seen in the vessel water level plot in Figure 6-38. The peak temperatures predicted for fuel rods and fuel debris regions, shown in Figure 6-39, are quite similar to that of Case 17, with late-time peak temperatures in lower plenum debris regions indicating the formation of a molten pool.

In-vessel hydrogen for Case 35 is shown in Figure 6-40, compared with that of Case 17. While the early hydrogen produced for Cases 17 and 35 are fairly close in magnitude, the late hydrogen for Case 35 is quite minimal compared with that of Case 17. Figure 6-41 again reveals that oxidation of metallic Zr is not significant in the generation of late hydrogen (not surprising, since the late hydrogen generation is minimal for this case). Figure 6-42 confirms that oxidation of stainless steel is not large for this case either. Also apparent from Figure 6-42 is the fact that stainless steel oxidation was significant in affecting the magnitude of late in-vessel hydrogen generation only in Case 17. Figure 6-43 shows the ex-vessel hydrogen produced from core/concrete interactions following the failure of the lower head, again by high temperature loss of strength.

Figure 6-44 and Figure 6-45 present the correlation for hydrogen production with steam escaping from the RCS breach location, this time at the hot leg nozzle location. Even with considerably larger amounts of steam escaping from the RCS hot leg breach in comparison with the lower head failure cases, late in-vessel hydrogen production does not seem significantly influenced by this phenomenon. This may be due to the pathway that the escaping steam takes in leaving the break location, perhaps escaping significant contact with the lower plenum metals.

One final potential correlation is suggested in Figure 6-46, where total seal leak steam loss of RCS inventory is compared against late in-vessel hydrogen generation. In this figure, there is some indication that larger loss of inventory through the seal leaks, above 180,000 kg of coolant, is associated with the ultimate production of lower quantities of late hydrogen, suggesting availability of oxidant could be limiting in some cases.

This concludes the presentation of fundamental accident progression signatures. The following section presents an analysis of sensitivity of hydrogen production to the MELCOR physics parameters varied in the LHS procedure.

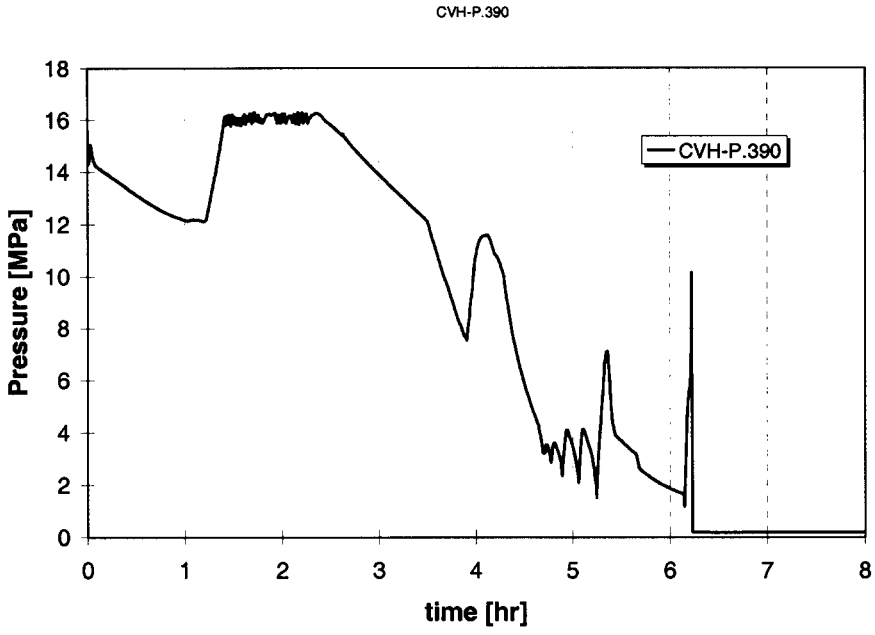

Figure 6-37 Case 35: RCS pressure for case with hot leg failure and low hydrogen.

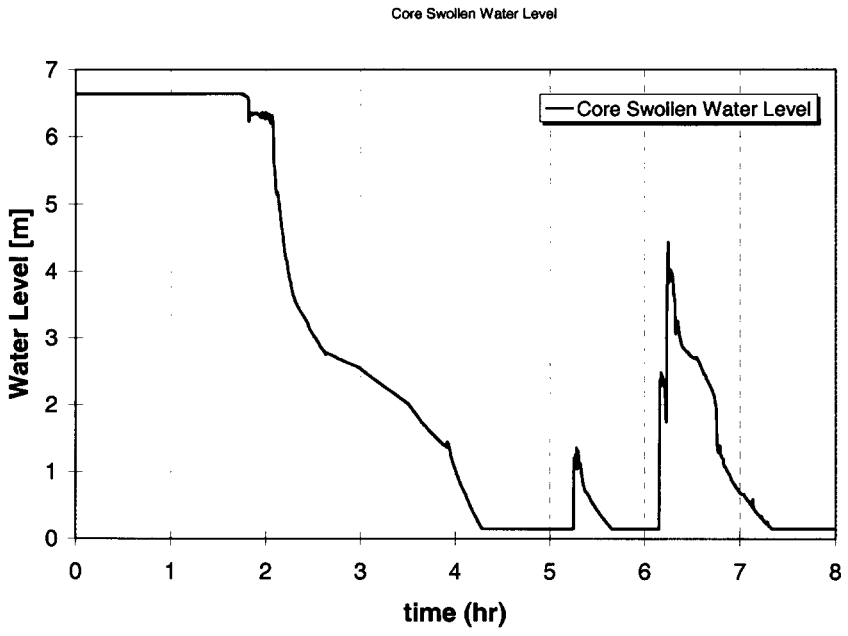

Figure 6-38 Case 35: Vessel water level for case with hot leg failure and low hydrogen.

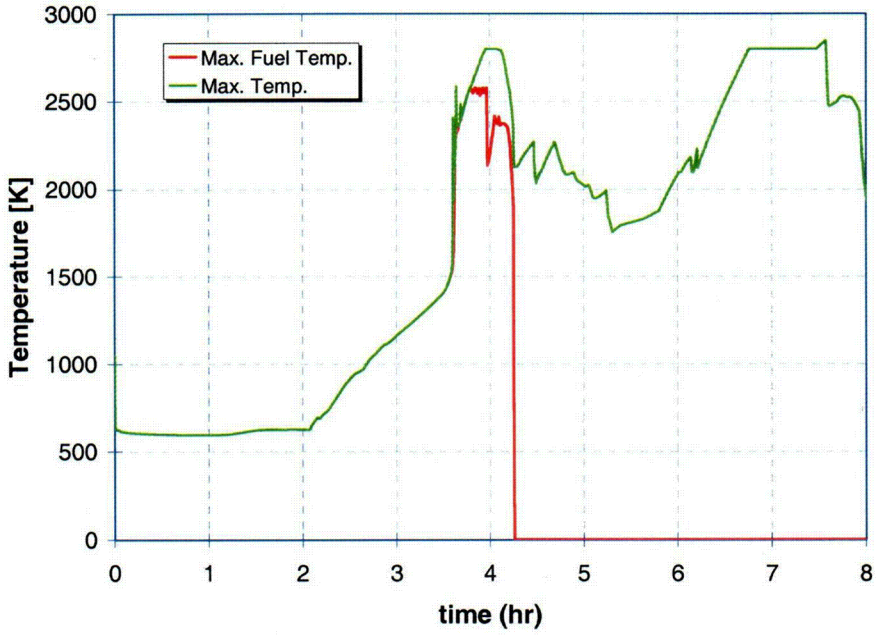

Figure 6-39 Case 35: Maximum fuel and debris temperature for case with hot leg failure and low hydrogen.

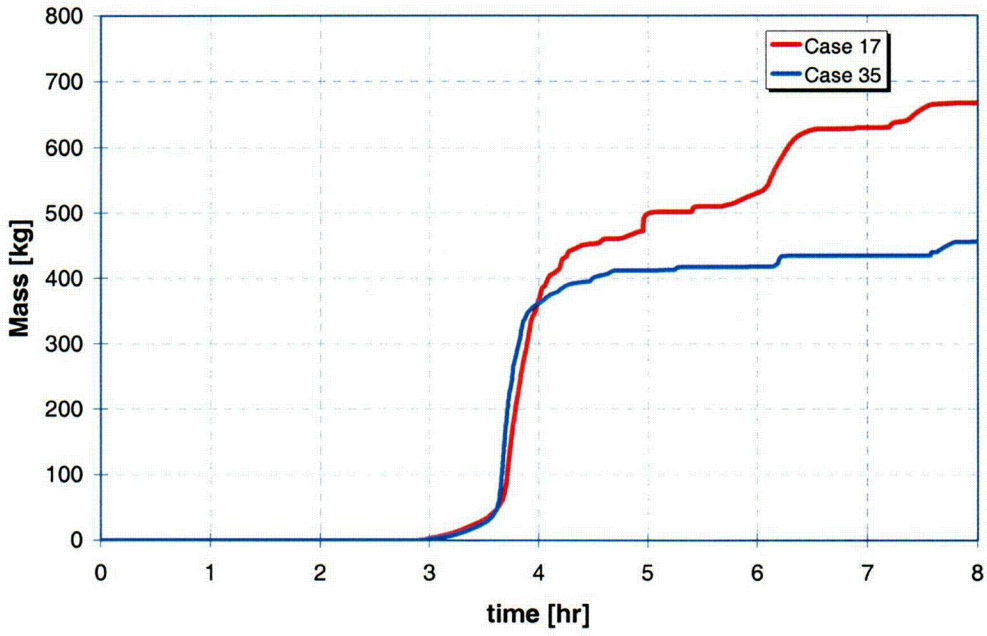

Figure 6-40 Case 35: In-vessel hydrogen for case with hot leg failure and low hydrogen, compared to Case 17.

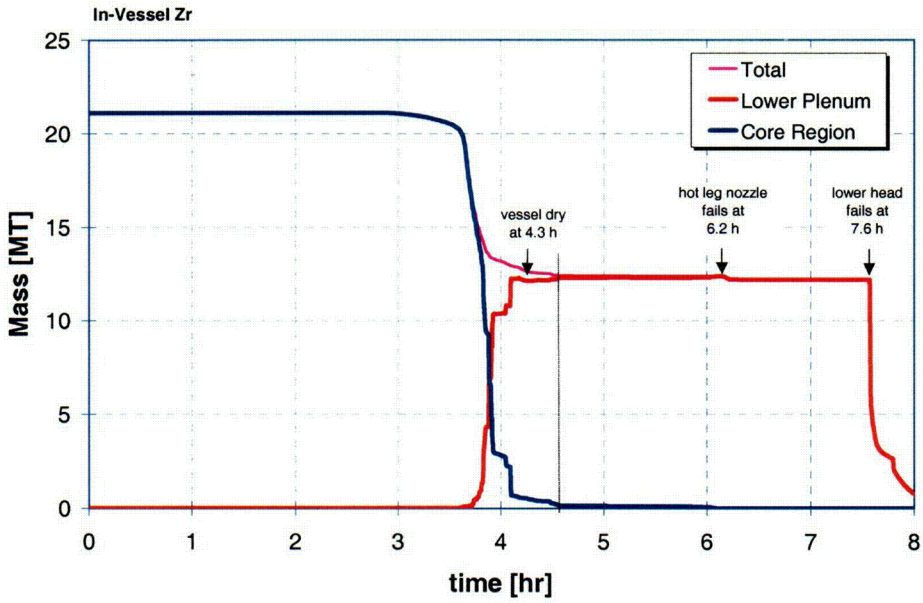

Figure 6-41 Case 35: Unoxidized in-vessel Zr for case with hot leg failure and low hydrogen.

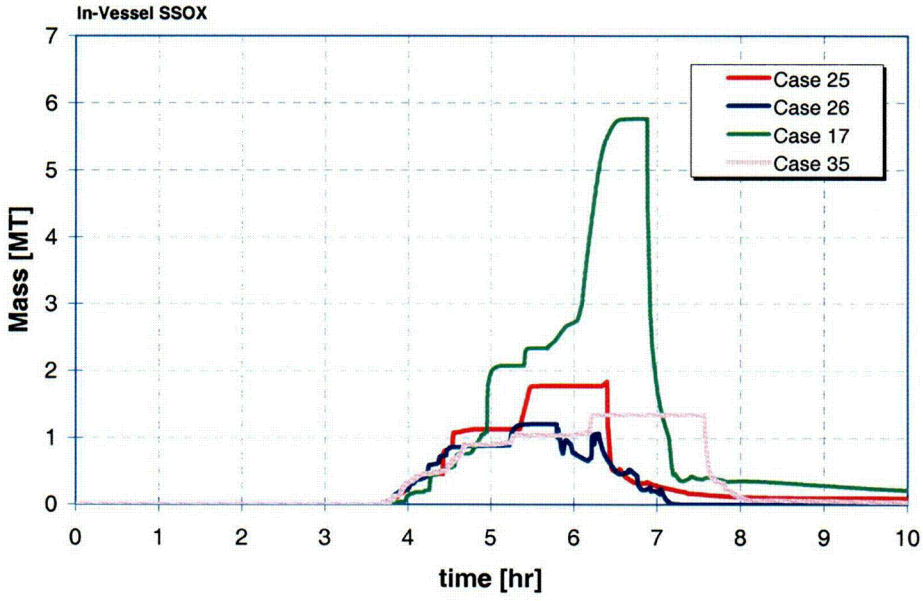

Figure 6-42 Case 35: Stainless steel oxide for case with hot leg failure and low hydrogen compared with other cases.

C40

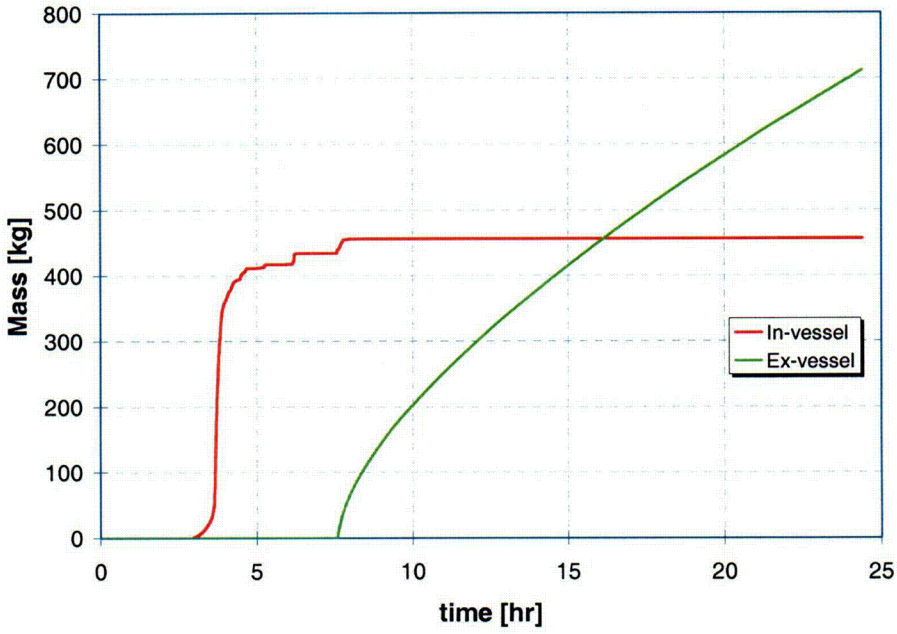

Figure 6-43 Case 35: Total in-vessel and ex-vessel hydrogen for case with hot leg failure and low hydrogen.

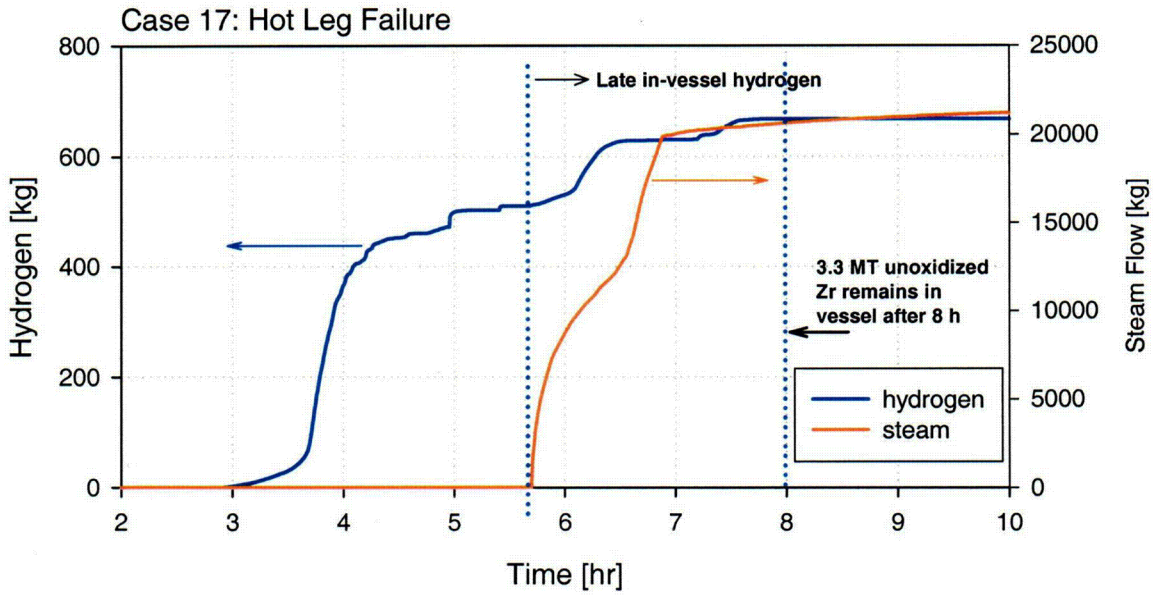

Figure 6-44 In-vessel hydrogen produced and break steam flow for case with high *late-time* in-vessel hydrogen for case with hot leg failure and high hydrogen.

C41

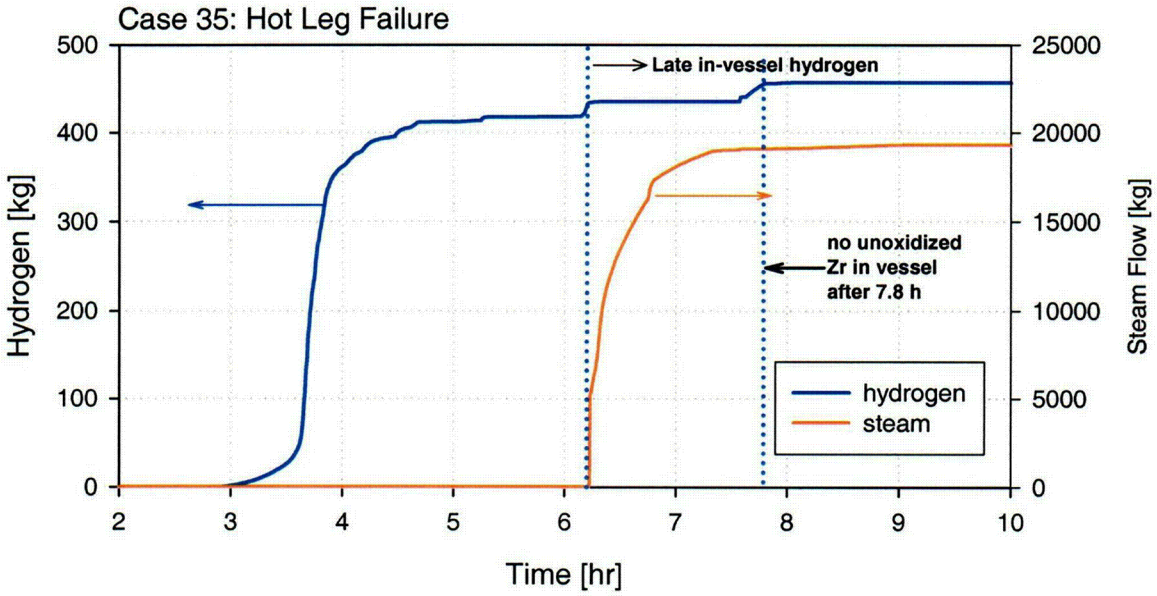

Figure 6-45 In-vessel hydrogen produced and break steam flow for case with low *late-time* in-vessel hydrogen for case with hot leg failure and low hydrogen.

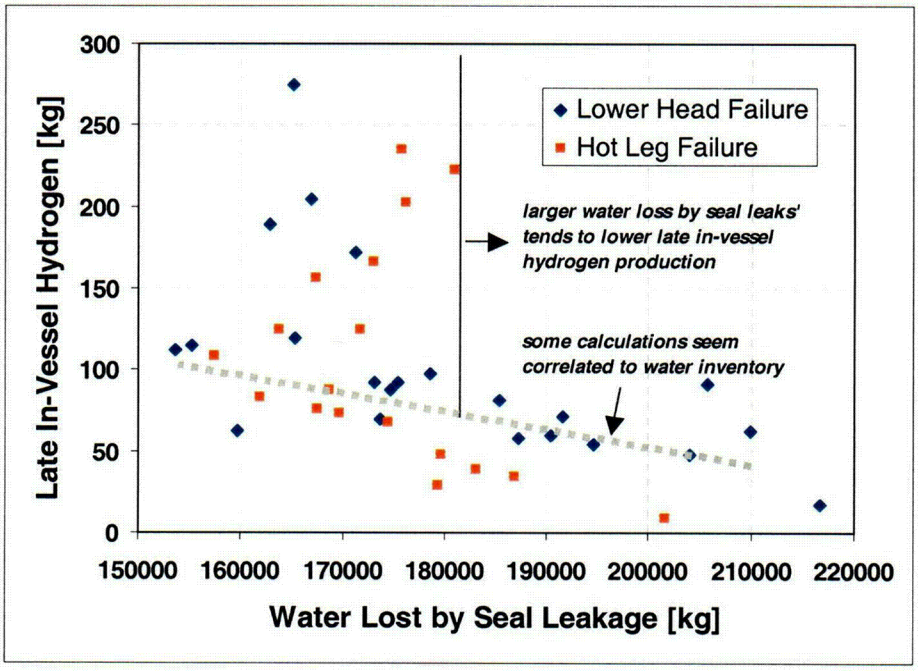

Figure 6-46 Correlation between late in-vessel hydrogen and RCS water loss via pump seals.

C42

7 Analysis of Parameter Sensitivity

7.1 Stepwise Linear Regression Analyses

A standard regression technique, stepwise linear regression, was used to determine which of the input variables are most strongly correlated with hydrogen production in the present study. This technique has been frequently used in the past to evaluate the most important of the uncertain input variables when performing MACCS2 calculations [10].

Two measures of hydrogen production were investigated: the final in-vessel and final ex-vessel productions. The results from the stepwise linear regression analyses are shown in Table 7-1 and Table 7-2 for these two cases, respectively. The columns in this table represent the following information: the first column provides the name of the variable in the linear expression, the second column represents the linear correlation coefficient, the third column indicates the standard error associated with the linear correlation coefficient, the fourth column represents the standard statistical function called the t-value, and the fifth column indicates the statistical significance of the correlation. A value in the final column between 0 and 0.05 indicates a strong statistical correlation; a value between 0.05 and 0.1 indicates a moderate correlation; and a value from 0.1 to 1.0 indicates a moderate to nonexistent correlation. Notice that both Tables are ordered from small to large values in the final column, with the exception of the intercept, which is always at the top. Thus, the correlations are in rank order of most significant at the top to least significant at the bottom. Notice that none of the input parameters are strongly correlated with hydrogen production; only a few are moderately correlated; most are weakly correlated.

In both tables, only the correlated variables for which the value of the coefficient is at least one standard error from zero are retained in the regression results. A correlation coefficient of zero indicates that the output value, hydrogen production, is independent of the input value. The purpose of the t-test values shown in the last two columns of the table is to show statistical likelihood that the correlation coefficient is significantly different from zero.

Table 7-1. Stepwise Linear Regression Results for In-Vessel Hydrogen Production

	Coeff.	Std. Error	t-Value	Pr(>|t|)
Intercept	239	427	0.559	0.580
Falling-Debris Heat-Transfer Coeff. (W m^{-2} K^{-1})	-0.731	0.4202	-1.740	0.091
Zr Melt-Release Temperature (K)	0.241	0.177	1.363	0.182
Lower Plenum Region Particle Diameter (m)	-3545	2610	-1.359	0.183
Zr Freezing Coefficient (W m^{-2} K^{-1})	0.0027	0.0024	1.149	0.258

Table 7-2. Stepwise Linear Regression Results for Ex-Vessel Hydrogen Production

Variable	Coeff.	Std. Error	t value	Pr(>|t|)
Intercept	1228	314	3.907	0.000
Zr Melt-Release Temperature (K)	-0.158	0.098	-1.616	0.115
Radiation Factor	238	153	1.551	0.130
Zr Freezing Coefficient ($W\ m^{-2}\ K^{-1}$)	0.0017	0.0013	1.327	0.193
Core- Region Particle Diameter (m)	-921	704	-1.308	0.200
UO_2 Collapse Temperature (K)	-0.0759	0.0759	-1.001	0.324

The most strongly correlated variables for in-vessel hydrogen production are the ones that we might have anticipated. In rank order, they are falling-debris heat-transfer coefficient, zirconium melt-release temperature, lower-plenum particle diameter, and zirconium freezing coefficient. Possible mechanisms for coupling between these variables and in-vessel hydrogen production are proposed in the following subsection, 7.2.

The most strongly correlated variables for ex-vessel hydrogen production are somewhat more surprising. In rank order, they are zirconium melt-release temperature, radiation factor, zirconium freezing coefficient, core-region particle diameter, and UO_2 collapse temperature. One surprising result is that the one parameter that directly controls ex-vessel phenomena, the multipliers for heat transfer between corium and an overlying water pool, did not make the list. One might expect that there is an inverse correlation between in-vessel and ex-vessel hydrogen production. This proves to have some validity, as discussed further in subsection 7.3.

Figure 7-1 shows the linear correlation between the MELCOR-calculated, final, in-vessel, hydrogen production and the correlation indicated in Table 7-1. This figure shows that there is significant residual variability in the data that is not captured by the correlation generated by the stepwise linear regression algorithm. This indicates that nonlinear interactions, not captured in the regression analysis, significantly affect the MELCOR-predicted, in-vessel, hydrogen production.

Figure 7-2 is analogous to Figure 7-1 except that it shows the comparison for ex-vessel hydrogen production. The correlation is somewhat better in this case, but again, significant residual uncertainty remains, indicating that this correlation only tells part of the story.

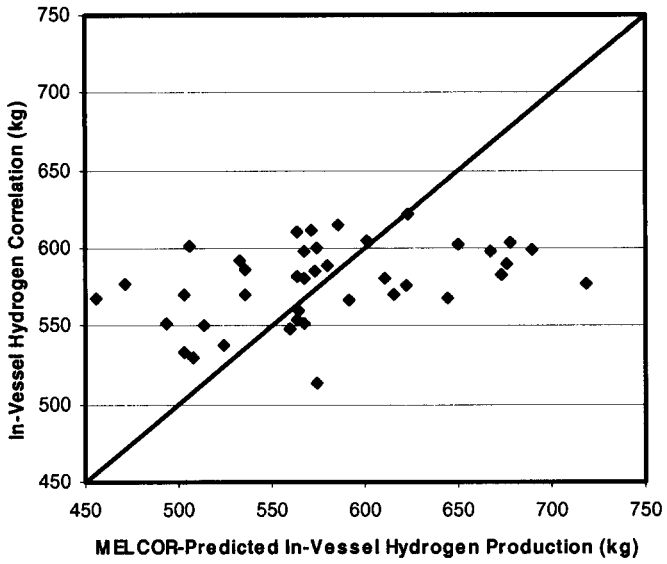

Figure 7-1 Comparison between MELCOR-predicted and correlated final, in-vessel, hydrogen production. The scatter points represent each of the MELCOR realizations. The solid line indicates perfect agreement between the predicted and correlated values.

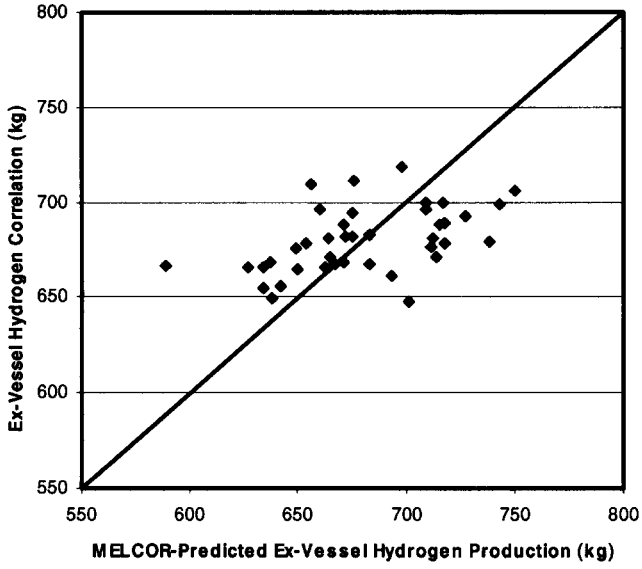

Figure 7-2 Comparison between MELCOR-predicted and correlated ex-vessel hydrogen production. The scatter points represent each of the MELCOR realizations. The solid line indicates perfect agreement between the predicted and correlated values.

7.2 Linear Regression Analyses of In-Vessel Hydrogen Production

In this section, parameters are discussed in order of their influence on in-vessel hydrogen production, as indicated in Table 7-1. The figures in this section display data from the 40 realizations as scatter points; they also display a linear least-squares fit to the data as a solid line. Unlike the stepwise linear regression analysis described in the previous subsection, the implicit assumption here is that only one variable is changing at a time. Obviously, this is not true, so significant scatter should be anticipated. The main purpose of this subsection is to provide a visualization and qualitative picture of the information from the linear stepwise regression analyses. In the figures below, the slope of the linear fit qualitatively displays the sensitivity of in-vessel hydrogen production to the input parameter. The scatter of the data around the line qualitatively shows the residual variability due to the other input parameters and due to nonlinear effects.

Figure 7-3 shows the sensitivity of *total* in-vessel hydrogen production to the falling heat-transfer coefficient between debris and water in the lower plenum. This input parameter is the most strongly correlated with in-vessel hydrogen production. The correlation coefficient is negative, indicating that hydrogen production is greater when this coefficient is smaller. Figure 7-4 suggests that a slightly stronger exists between this parameter and the early in-vessel hydrogen generation. There are several possible explanations, but one presently favored is the effect of this parameter on repressurization-induced failure of the hot-leg nozzle by creep-rupture. Greater heat transfer to the water in the lower head following core plate failure induces larger pressure spikes that can lead to hot-leg nozzle failure. This is born out by the data, which show that the average values of this coefficient are 215 and 251 W m^{-2} K^{-1}, respectively, when the hot-leg nozzle does not and does fail. (The range of falling heat-transfer coefficients explored was about 125 to 400 W m^{-2} K^{-1}.) On the average, the RCS experiences over 1/3 hr longer at high pressure when the hot-leg nozzle does not fail.

Figure 7-5 and Figure 7-6 show the sensitivity of *total and early* in-vessel hydrogen production (respectively) to the zirconium melt-release temperature. The correlation in this case is positive, indicating that hydrogen production is greater when zirconium relocates at higher temperatures. This agrees with our intuition, which is that the cladding should undergo more oxidation when held at higher temperatures for longer periods.

Figure 7-7 and Figure 7-8 show how hydrogen production varies with debris particle size in the lower plenum. In this case the slope is negative, indicating that more hydrogen is produced when the debris particle size is small. This also agrees with our intuition, which tells us that the greater the interfacial area between the particles and steam, the more oxidation should take place. Debris particle size in the lower plenum is also coupled with heat transfer between the falling debris and water. Thus, the trend shown in Figure 7-7 is related to the trend shown in Figure 7-3.

Figure 7-10 and Figure 7-11 shows the sensitivity of in-vessel hydrogen production to the zirconium freezing coefficient. The slope of the linear fit in this case is positive, indicating that more total hydrogen is generated when candling heat transfer is greater. This again is telling us that zirconium oxidation and hydrogen production are greater when more zirconium is retained in the relatively hot regions of the core.

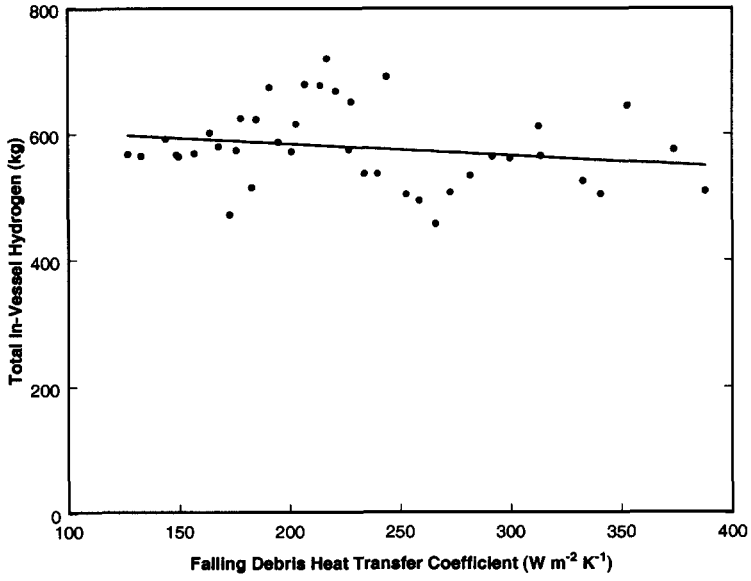

Figure 7-3. Sensitivity of *total* in-vessel hydrogen production to falling-debris heat-transfer coefficient in the lower plenum.

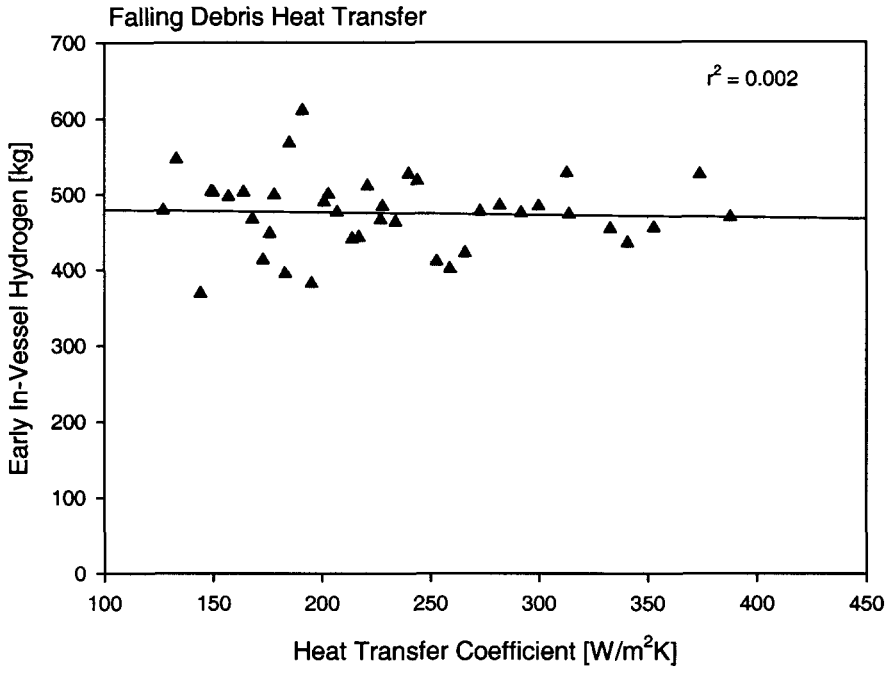

Figure 7-4 Sensitivity of *early-time* in-vessel hydrogen production to falling-debris heat-transfer coefficient in the lower plenum.

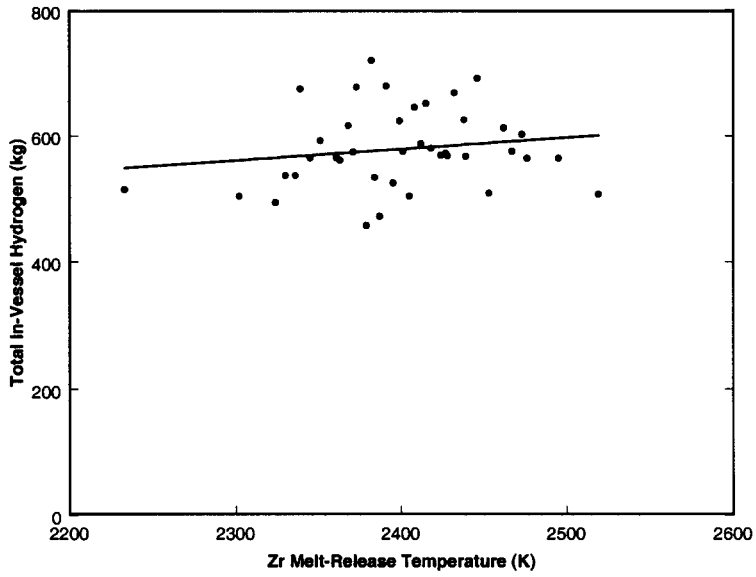

Figure 7-5. Sensitivity of *total* in-vessel hydrogen production to zirconium melt-release temperature.

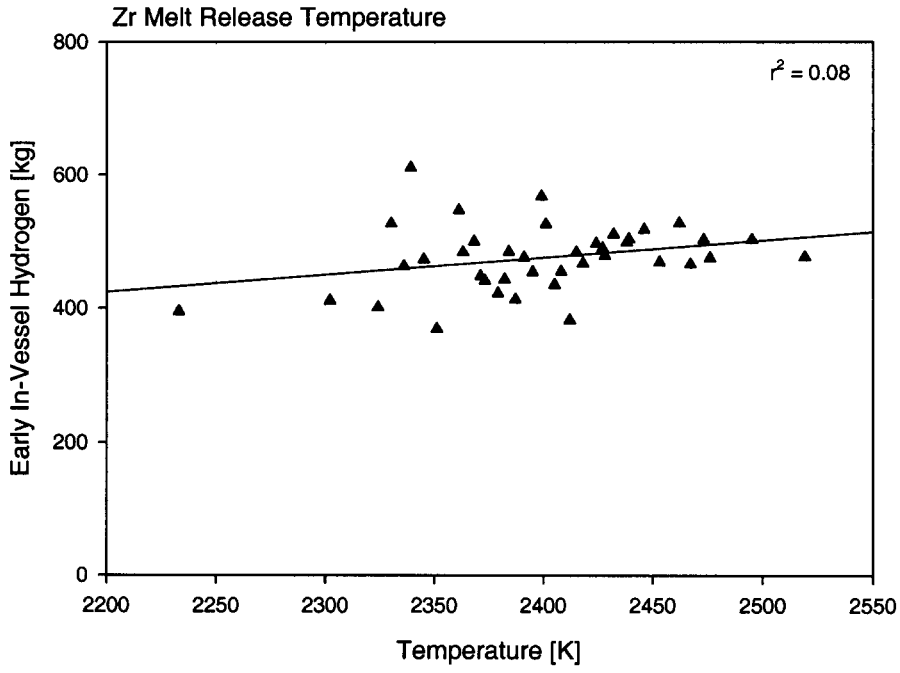

Figure 7-6 Sensitivity of *early-time* in-vessel hydrogen production to zirconium melt-release temperature.

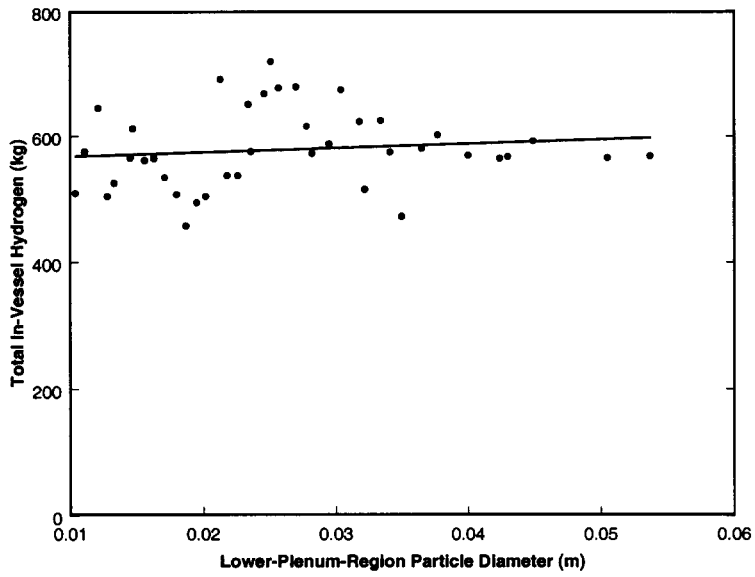

Figure 7-7. Sensitivity of *total* in-vessel hydrogen production to debris particle size in the lower plenum.

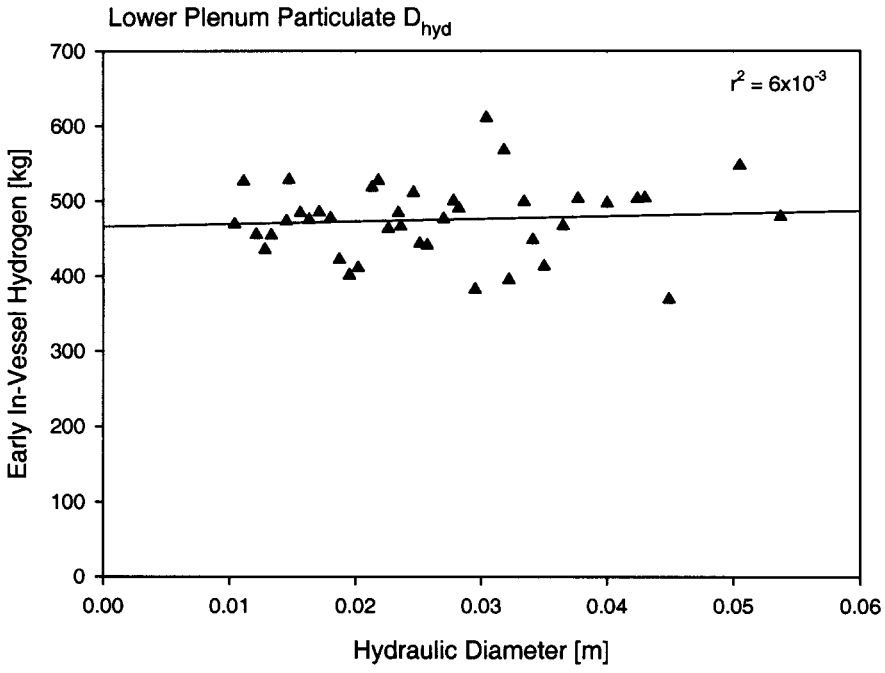

Figure 7-8 Sensitivity of *early-time* in-vessel hydrogen production to debris particle size in the lower plenum.

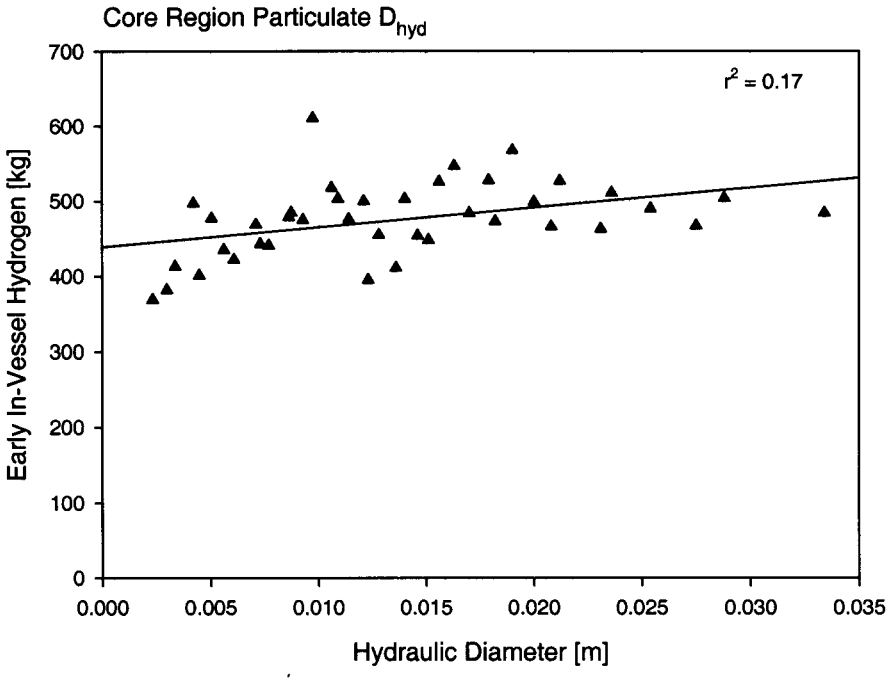

Figure 7-9 Sensitivity of *late-time* in-vessel hydrogen production to debris particle size in the lower plenum.

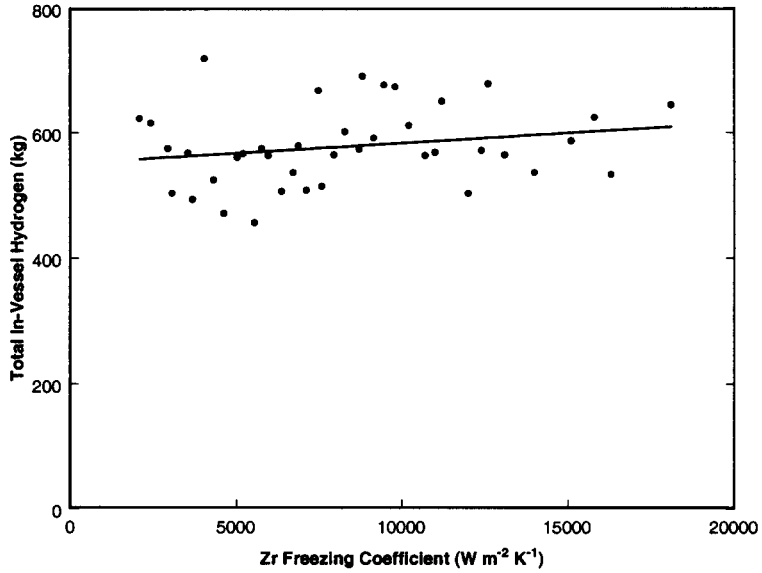

Figure 7-10. Sensitivity of *total* in-vessel hydrogen production to zirconium freezing coefficient.

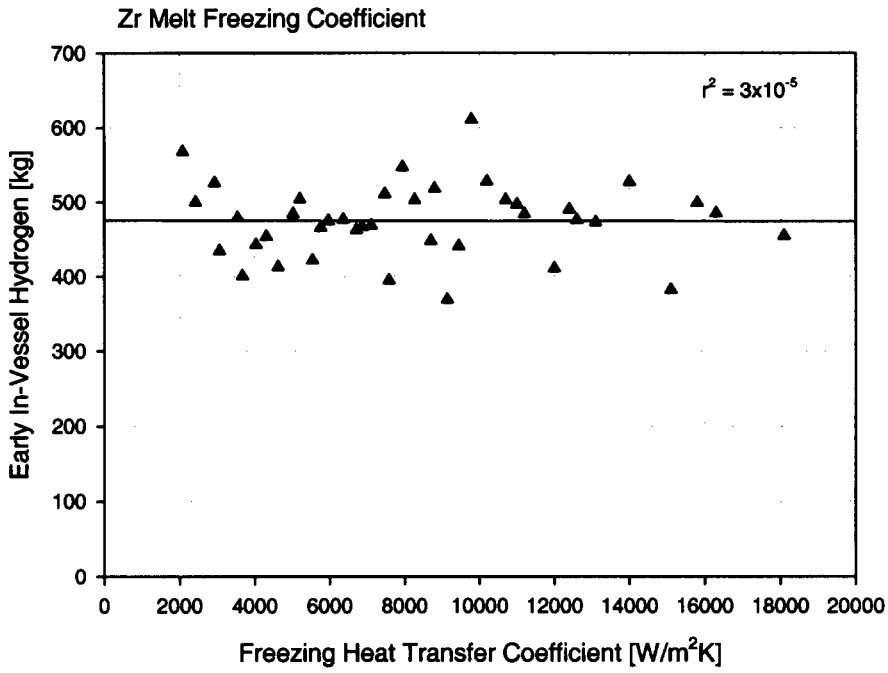

Figure 7-11 Sensitivity of *early-time* in-vessel hydrogen production to zirconium freezing coefficient.

7.3 Linear Regression Analyses of Ex-Vessel Hydrogen Production

This section is analogous to the preceding one, except that the results are for ex-vessel hydrogen production. Parameters are discussed in order of their influence, as indicated in Table 7-2. Like the previous section, the figures display data from the 40 realizations as scatter points; they also display a linear least-squares fit to the data as a solid line. The slope of the linear fit qualitatively displays the sensitivity of hydrogen production to the input parameter. The scatter of the data around the line qualitatively shows the residual variability due to the other input parameters and due to nonlinear effects.

Before examining the correlations between input variables and ex-vessel hydrogen production, it is worth noting that our expectation is that there should be an inverse correlation between in-vessel and ex-vessel hydrogen production. The correlation is displayed in Figure 7-12 and bears out our intuition. This indicates that we might generally expect to find the opposite trend for the influence of a parameter on ex-vessel hydrogen production as it had on in-vessel hydrogen production. However, there is considerable scatter in the plot, indicating that this inverse relationship might not be universal. This plot also indicates that not all of the materials that can be oxidized, mainly zirconium and stainless steel, are oxidized. In fact, the range of MELCOR-predicted, total, hydrogen production, in-vessel plus ex-vessel, is 1140 to 1370 kg.

Figure 7-13 shows the sensitivity of ex-vessel hydrogen production to zirconium melt-release temperature. The stepwise algorithm indicates that this parameter is the most highly correlated to ex-vessel hydrogen production and that the statistical significance is moderate. The likely explanation

for this correlation is that when more zirconium is oxidized in-vessel, less remains to oxidize ex-vessel.

Figure 7-14 shows the linear correlation between inter-ring, radiation factor in the core and ex-vessel hydrogen production. It is somewhat interesting that, while this parameter is very weakly correlated with in-vessel hydrogen production, it is nonetheless moderately correlated with ex-vessel production. The correlation is positive, indicating that increasing the radiation factor increases the ex-vessel hydrogen production. A possible explanation is that enhanced radiation results in a more uniform vessel temperature and thus leads to more ejection of fuel materials from the outer rings into the cavity. To confirm this, it might be worthwhile to correlate the mass of corium ejection to this and possibly other input variables.

Figure 7-15 shows the sensitivity of ex-vessel hydrogen production to the zirconium freezing coefficient. This parameter has a positive correlation with both in-vessel and ex-vessel hydrogen production. The correlation to ex-vessel hydrogen production is not obvious, but may be related to the quantity of corium ejected into the cavity. This connection bears further investigation.

Figure 7-16 shows the sensitivity of ex-vessel hydrogen production to core-region particle diameter. The trend is negative, indicating that reducing the diameter increases ex-vessel hydrogen production. Again, this correlation is not obvious and probably bears further investigation.

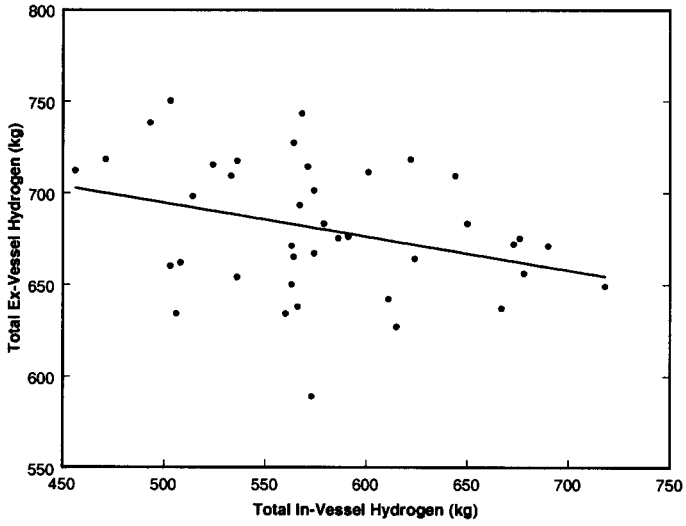

Figure 7-12. Correlation between in-vessel and ex-vessel hydrogen production.

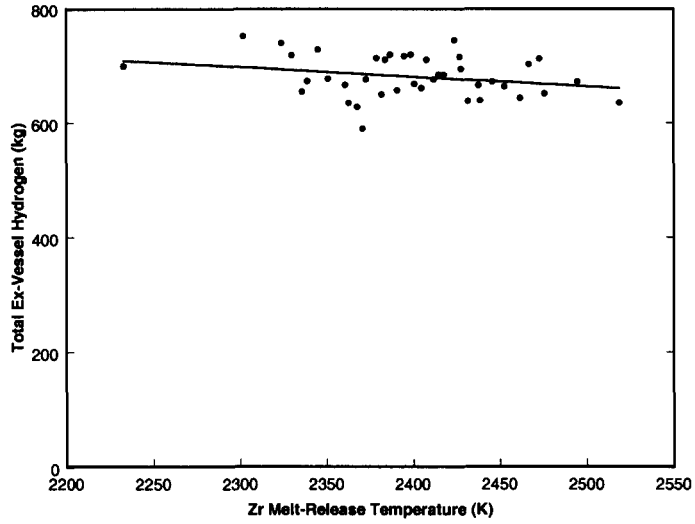

Figure 7-13. Sensitivity of ex-vessel hydrogen production to zirconium melt-release temperature.

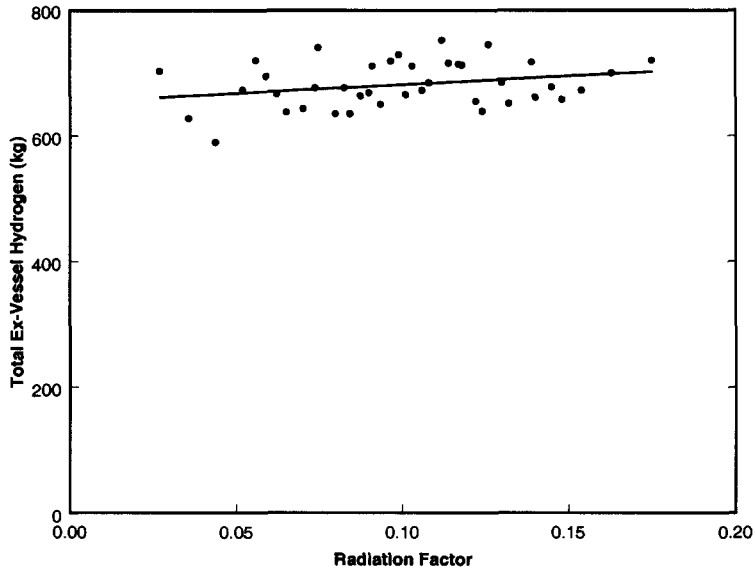

Figure 7-14. Sensitivity of ex-vessel hydrogen production to radiation factor between adjacent fuel rings.

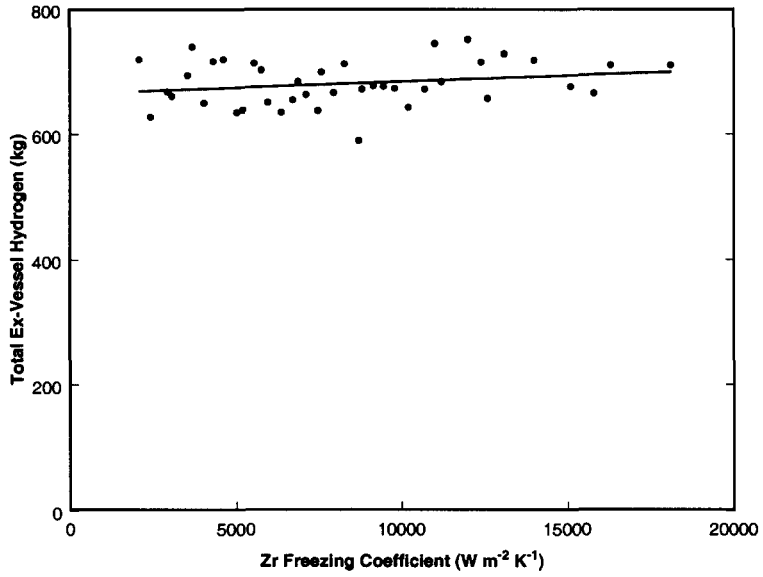

Figure 7-15. Sensitivity of ex-vessel hydrogen production to zirconium freezing coefficient.

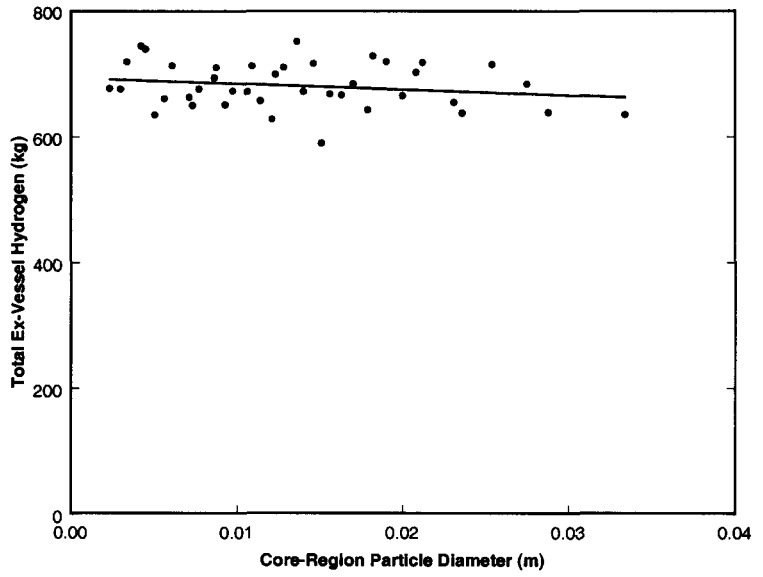

Figure 7-16. Sensitivity of ex-vessel hydrogen production to core-region particle diameter.

Figure 7-17 shows the sensitivity of ex-vessel hydrogen production to UO_2 collapse temperature. The slope of the linear fit is slightly negative, indicating that less ex-vessel hydrogen is produced when the collapse temperature is greater. This agrees with our intuition that UO_2 collapse temperature should correlate positively with in-vessel hydrogen production and with the inverse relationship between in-vessel and ex-vessel hydrogen production illustrated in Figure 7-12. Note, however, that the statistical significance of this correlation is marginal because the correlation coefficient is almost exactly one standard error from zero.

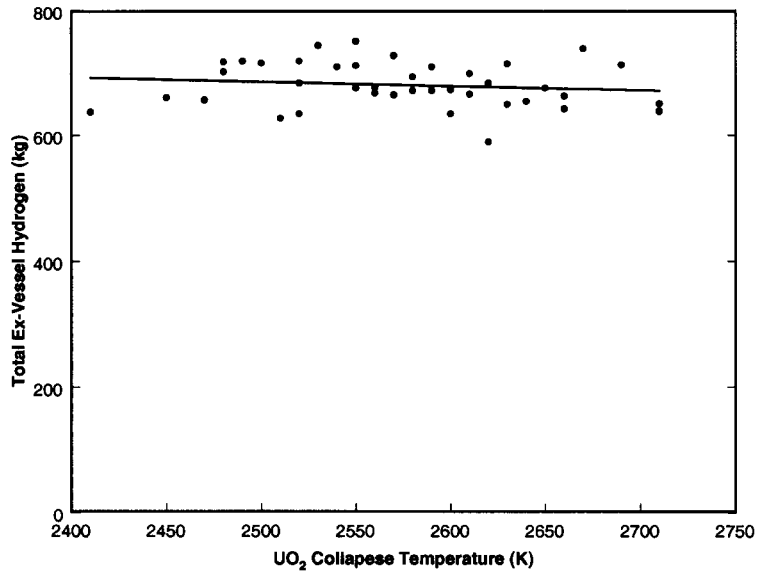

Figure 7-17. Sensitivity of ex-vessel hydrogen production to UO_2 collapse temperature.

8 Summary and Discussion

This study presents a method of characterizing uncertainties associated with the predictions of severe accident phenomena using the MELCOR code, in this case, the production of hydrogen for Station Blackout conditions in the Sequoyah plant. The basic approach of this methodology is to identify the MELCOR input parameters, sensitivity coefficients, and modeling options that describe or influence the uncertainty of interest, prescribe likelihood descriptions of the potential range of these parameters, and evaluate code predictions using a number of different random combinations of these parameter inputs sampled from the likelihood distributions. In order to limit the number of "realizations" (code calculations) needed to characterize the full range of uncertainty, the Latin Hypercube Sampling method (LHS) is used to sample the input parameter distributions. The methodology is denoted in this report as the *MELCOR Probabilistic Uncertainty Analysis Methodology (MPUAM)*, and while this study has emphasized hydrogen production, uncertainty in the prediction of other issues, such as fission product source terms, may similarly be examined.

Forty realizations (MELCOR calculations) were performed with LHS-generated samples from 10 uncertain MELCOR physics parameters to characterize the range of potential in-vessel and ex-vessel hydrogen generation due to the uncertainties in physics knowledge. Detailed rationale for likelihood distributions and range of uncertain parameters are provided. The uncertainty range, or spread, in predicted in-vessel hydrogen generation, gradually increased with time with a total *early in-vessel* range of 145kg around a mean value of 450 kg at ~5h *(+/- 16%)*, increasing to a *late in-vessel* range of 262 kg around a mean of 578 kg at ~10 h *(+/- 23%)*. Some realizations (~45%) produced creep rupture failure of the hot leg nozzle, assisted by natural circulation of hot gases from the reactor core to the steam generators, and the remainder produced lower head creep rupture failures following about an hour after significant relocation of core materials to the lower plenum. Initial failures of the RCS by either hot leg failure or lower head rupture, generally occurred between 6 to 7.5 hrs into the accident progression. Cases that produced hot leg rupture, ultimately also produced a later failure of the lower head by thermally induced loss of strength after core material relocation to the lower plenum. In all cases, unabated core concrete interactions ensued with core material transfer to the reactor cavity, owing to the lack of any significant quantities of water in the cavity. (Note that melting of the ice beds alone does not produce enough water to flood into the reactor cavity.) There was no consistent relationship between mode of vessel/RCS failure and the quantity of hydrogen produced.

Some cases which produced low amounts of hydrogen by 5 hrs went on to produce high amounts of hydrogen by 10 hrs, and vise versa, regardless of the mode of vessel failure. A characteristic signature for all analyses was the renewed production of hydrogen during the *late in-vessel* period following vessel/RCS rupture after leveling off at the end of the *early in-vessel* hydrogen production period. The early in-vessel hydrogen tends to level off as vessel water inventory is depleted although sporadic and partial accumulator injections lead to short renewals of the early hydrogen generation. Late hydrogen production results from the larger and complete injection of remaining accumulator water. The amount of hydrogen produced in the late in-vessel period is determined by the accessibility of water to "oxidizable" metals (Zr and stainless steel) and the amount of materials

remaining in-vessel (remaining in-vessel metallic materials are diminished both by oxidation and by loss to the cavity following failure of the lower head). For cases where the lower head failed first, late in-vessel hydrogen was dominated by oxidation of Zr metal remaining in the lower head as the accumulator water made its way to the cavity via the breach in the lower head. On the other hand, deep reflooding of lower head debris that occurred for cases where the hot leg nozzle failed first, appeared to produce late in-vessel hydrogen by oxidation of stainless steel remaining in the vessel and presumably above the reflood water level. It is significant, however, to point out that deep reflooding of the lower head debris did not result in quenching of the very hot debris in this location, and often debris temperatures above the liquidus were observed in the hottest lower plenum locations after accumulator injection.

Statistical evaluation of hydrogen generation showed fairly large and somewhat random variations amongst the 40 realizations. Various regression analyses, including Stepwise, a systematic regression method that attempts to identify and fit the most significant input parameters to a multivariate linear model, did not result in models with high degree of statistical correlation. This is not to say that no trends were observed. The most significant varied parameters, in rank order of importance, in determining the total in-vessel hydrogen were found to be: falling Debris heat transfer coefficient, Zr-melt release temperature and the Zr freezing coefficient. Indeed, the zircaloy melt release temperature parameter, which was considered to be the most significant parameter with respect to hydrogen generation prior to conducting this study, was shown to exhibit the expected general trend, especially for the early in-vessel hydrogen. However, the degree of variation observed in the realizations associated with varying the uncertain parameter was greater that the full range of hydrogen predicted by the regression fit to that parameter. In other words, the general trend is recognizable amongst the large overall scatter in the results, but the correlation is low.

In part, we feel that the degree of scatter in the predicted hydrogen results, when plotted against *any* of the varied uncertain parameters, is an inherent characteristic of the complex and coupled integral prediction rendered by MELCOR, involving many synergistic and non-linear interactions between physical models. Indeed, some degree of residual randomness, we feel, is likely to remain after individual input parameter uncertainty ranges have been reduced below some minimum level. The present degree of uncertainty (or certainty) attributed to the parameters explored in this study may be near this minimum threshold. We also feel that this is a reflection on the degree of *certainty* in these modeled processes that has been gained over these past 20 years of research in the field of severe accidents and core melt progression, and that similar degrees of residual uncertainty remain associated with all of the parameters investigated. In other words, if the uncertainty range in hydrogen generation were to be further reduced, it would require relatively equal reduction of uncertainty for all of the varied parameters, since none emerged from the statistical evaluation as being particularly dominant.

9 References

1. Gauntt, R.O. and L.L. Humphries, *Hydrogen Source Terms for Station Blackout Accidents in Sequoyah and Grand Gulf Estimated Using MELCOR 1.8.5*, letter report to NRC/DSARE, July 30, 2001.

2. Gauntt, R.O., R.K. Cole, et al., *MELCOR Computer Code Manuals, Version 1.8.5*, NUREG/CR-6119, Rev. 2, October 2000.

3. Wyss, G. and Jorgensen, 1998

4. Gauntt, R.O., S.G. Ashbaugh, A.R. Hill and K.C. Wagner, *Development of MELCOR 1.8.5 Models of Westinghouse Large Dry, Ice Condenser, and Subatmospheric Containment Pressurized Water Reactor Nuclear Power Plants*,

5. Sequoyah Nuclear Plant Final Safety Analysis Report – Volume 3, Tennessee Valley Authority, February 1, 1974.

6. SIEMENS MELCOR Uncertainty Study, CSARP Presentation.

7. Magallon, D. FARO, *LWR Programme Quench Test-2 Data Report*, Technical Note No.I.93.154.

8. Farmer, M.T. Modeling of Ex-Vessel Corium Coolaibility with the CORQUENCH Code, ICONE-9696.

9. Boardman, T. et al., *Leak Rate Analysis of the Westinghouse Reactor Coolant Pump*, NUREG/CR-4294, July 1985.

10. Chanin, D. I., and M. L. Young, *Code Manual for MACCS2, User's Guide*, NUREG/CR-6613, Vol. 1, SAND97-0594, May 1998.